

Measurements and Interpretations of Light Scattering  
From Intact Biological Cells

by

Jeremy D. Wilson

Submitted in Partial Fulfillment

of the

Requirements for the Degree

Doctor of Philosophy

Supervised by

Professor Thomas H. Foster

Department of Physics and Astronomy  
The College  
Arts & Sciences

University of Rochester  
Rochester, New York

2007

## **Curriculum Vitae**

The author was born in Fort Campbell, Kentucky on January 30, 1979. He attended Lewis and Clark College from 1997 to 2001, and graduated with a Bachelor of Arts in physics and mathematics. He came to the University of Rochester in the fall of 2002 and began graduate studies in the Department of Physics. He received a GAANN Fellowship for the years 2002 – 2005, and received the Messersmith Fellowship in 2006. He pursued his research in the area of experimental biological physics under the direction of Professor Thomas H. Foster, and received the Master of Arts degree from the University of Rochester in 2004.

## **Refereed publications**

W.J. Cottrell, J.D. Wilson, and T.H. Foster, "An inverted microscope enabling multi-modality imaging, angle-resolved scattering and scattering spectroscopy," *Opt. Lett.* **32**, 2348-2350 (2007).

J.D. Wilson, B.R. Giesselman, S. Mitra, and T.H. Foster, "Lysosome-damage-induced scattering changes coincide with release of cytochrome c," *Opt. Lett.* **32** (2007).

J.D. Wilson and T.H. Foster, "Characterization of lysosomal contribution to whole-cell light scattering as quantified by photodynamic organelle ablation," *J. Biomed. Opt.* **12**, 030503 (2007).

K. K-H. Wang, J.D. Wilson, M.E. Kenney, S. Mitra, and T.H. Foster, "Irradiation-induced enhancement of Pc 4 fluorescence and changes in light scattering are potential dosimeters for Pc 4-PDT," *Photochem. Photobiol.* DOI: 10.1111/j.1751-1097.2007.00128.x (2007).

J.D. Wilson, W.J. Cottrell, and T.H. Foster, "Index-of-refraction-dependent sub-cellular light scattering observed with organelle-specific dyes," *J. Biomed. Opt.* **12**, 014010 (2007).

J.D. Wilson and T.H. Foster, "Mie theory interpretations of light scattering from intact cells," *Opt. Lett.* **30**, 2442-2444 (2005).

J.D. Wilson, C.E. Bigelow, D.J. Calkins, and T.H. Foster, "Light scattering from intact cells reports oxidative-stress-induced changes in mitochondrial morphology," *Biophys. J.* **88**, 2929-2938 (2005).

S.L. Tufté, J.D. Wilson, G.J. Madson, L.M. Haffner, and R.J. Reynolds, "WHAM observations of H $\alpha$  from high-velocity clouds: are they galactic or extragalactic?" *Astrophys. J. Lett.* **572**, L153-L156 (2002).

## **Conference proceedings papers**

J.D. Wilson and T.H. Foster, "Fluence- and time- dependent lysosomal and mitochondrial damage induced by LS11-PDT characterized with light scattering," *SPIE Proceedings* **6446**, 64460F (2007).

J.D. Wilson and T.H. Foster, "PDT-induced changes in light scattering from cells using lysosomal- vs. mitochondrial-localizing photosensitizers," *SPIE Proceedings* **6139**, 613903 (2006).

J.D. Wilson and T.H. Foster, "Light scattering reports early mitochondrial responses to photodynamic therapy," *SPIE Proceedings* **5689**, 9-16 (2005).

J.D. Wilson, C.E. Bigelow, D.J. Calkins, and T.H. Foster, "Early mitochondrial responses to photodynamic therapy are reported by angularly resolved light scattering," In Biomedical Topical Meetings on CD-ROM (The Optical Society of America, Washington, DC), **FH13**, 37-39 (2004).

## **Talks**

J.D. Wilson, "Measurements and interpretations of light scattering from intact cells," PDT seminar, Division of Radiation Physics, Department of Radiation Oncology, University of Pennsylvania, Philadelphia, PA, May 7, 2007.

J.D. Wilson and T.H. Foster, "Fluence- and time-dependent lysosomal and mitochondrial damage induced by NPe6 PDT characterized with light scattering," SPIE Photonics West: Biomedical Applications of Light Scattering, San Jose, CA, January 21, 2007.

J.D. Wilson and T.H. Foster, "Interpreting light scattering signatures from cells subjected to oxidative stress," *Invited talk* at OSA Frontiers in Optics: Leveraging spectroscopic biosignatures, Rochester, NY, October 10, 2006.

## **Poster presentations**

J.D. Wilson and T.H. Foster, "PDT-induced changes in angularly resolved light scattering from Intact cells as a reporter of mitochondrial and lysosomal morphology," 11<sup>th</sup> Congress of the European Society for Photobiology, Aix Les Bains, France, September 7, 2005.

J.D. Wilson and T.H. Foster, "Angularly resolved light scattering in photodynamic therapy probes organelle morphology and composition changes," Engineering Conferences International: Advances in Optics for Biotechnology, Medicine, and Surgery, Copper Mountain, CO, July 26, 2005.

J.D. Wilson, C.E. Bigelow, D.J. Calkins, and T.H. Foster, "Early mitochondrial responses to photodynamic therapy are reported by angularly resolved light scattering," Optical Society of America Biomedical Optics Topical Meeting, Miami Beach, FL, April 16, 2004.

## Acknowledgements

I would like to gratefully acknowledge some of the people who have helped me over the years and made the completion of this document possible.

I would first like to thank my thesis advisor, Professor Thomas H. Foster. I am very appreciative of the time and effort that Professor Foster has invested in me, and for the unique opportunities afforded to me as a member of his research group. Professor Foster has shown an unwavering concern for the success of his students, and has demonstrated a rare balance between always being accessible and allowing me almost complete freedom and responsibility to pursue independent research. I am very grateful that my studies at Rochester were carried out in Professor Foster's research group.

I also had the privilege of working with several excellent graduate students in Professor Foster's research group: Chad Bigelow, Soumya Mitra, William Cottrell, Benjamin Pearson, Ken Kang-Hsin Wang, and Tammy Lee. Chad was instrumental in helping me get started in the lab, and was the source of many discussions about light scattering. Soumya has been a steady source of knowledge about biological and biophysical aspects of photodynamic therapy. As Soumya has made the transition from graduate student to faculty member in the Department of Imaging Sciences, he has become an invaluable resource as the person who has worked on virtually every experiment in the laboratory. William

has been exceptionally helpful throughout the years, and his vast knowledge of optics and particular aptitude for design and construction of equipment has made him one of the more sought out members of the Foster Laboratory. William carried out much of the rigorous optical design and characterization for the multifunctional scattering microscopy instrument described in Chapter 8. Benjamin joined our laboratory for only one year, but while he was here he did much of the tissue culture that was instrumental to many of my experiments. Ken has been a great help throughout the years, and he carried out the clonogenic cell survival assay presented in Chapter 7. Tammy is a relatively new addition to the laboratory, and her work in tissue culture has been most helpful over the last year.

I would also like to thank two technical members of the Foster Laboratory: David Conover and Benjamin Giesselman. David is an Associate in the Department of Imaging Sciences, whose help has been invaluable in the construction of the goniometer experiment from both the hardware and software side. He has also been quite helpful in the resurrection of the diffuse reflectance experiments, for which I am most grateful. Benjamin is a technician in the laboratory and the only person in the group with an undergraduate degree in biology, and his work in tissue culture as well as in the immunofluorescence staining presented in Chapter 7 has been most helpful.

There are several collaborators outside of the Foster Laboratory that deserve recognition. I would like to thank Professor David J. Calkins (currently at Vanderbilt) and Karen de Mesy Bentley for their help with the electron

microscopy studies presented in Chapter 4. I would also like to thank Michael Valentino and Professor John Frelinger for their help in designing the cytochrome c imaging assay. Scott Gibson, formerly with the Laboratory of Professor Russell Hilf, deserves special recognition for his willingness to drop everything and help Foster Lab members with biology-related problems. Scott was especially helpful with the protocol to isolate and validate viable mitochondria from fresh rabbit liver presented in Chapter 4.

I would like to gratefully acknowledge financial support from the National Institutes of Health grants CA122093 and CA68409 awarded by the National Cancer Institute. I also gratefully acknowledge financial support from the Agnes M. and George Messersmith Fellowship awarded by the University of Rochester for the 2006 – 2007 academic year.

Finally, I would like to thank my family for their love and support throughout the years. The support of my parents, James Wilson and Cynthia Weaver, and of my stepparents Lawrence Weaver and Deana Wilson, throughout my years of study has been truly amazing. I would especially like to thank my wife, Anne, for her love, support, and understanding these last couple of years, without which none of this would have been possible.

## **Abstract**

Visible light interacts with biological cells primarily through elastic scattering. The details of how cells scatter light depend on their morphology and their substructures. In this thesis we first present a series of experiments and models to discern the specific contributions of certain sub-cellular constituents to whole-cell scattering. Exploiting the findings of those studies, we report on experiments within model systems of cell death that demonstrate the potential of light scattering measurements as a tool in modern biology. Instrumentation capable of exploiting the findings of this thesis from a biology-relevant microscopy platform is designed and developed.

A Mie theory based interpretation of light scattering signals originating from a collection of particles with a broad size distribution is developed. Upon applying this model to scattering data from intact cells, we find that it robustly extracts the size scale of dominant light scattering particles, suggests that scattering measurements are sensitive primarily to mitochondrial and lysosomal morphology, and unites conflicting results in the literature. Using this model as a basis, we present a collection of studies in which we use various strategies of photodynamic therapy (PDT) as a biophysical tool to perturb mitochondria and lysosomes, and observe the effects of these perturbations on whole-cell scattering. Through these experiments, we are able to discern the individual contributions of

mitochondria and lysosomes to whole-cell light scattering, and demonstrate that mitochondria are responsible for roughly 80% of the scattering signal.

Results of experiments aimed at demonstrating the potential role that light scattering measurements have to play in future studies of cell death biology are presented. We first show that mitochondrial-PDT-induced morphology changes measured with light scattering map into the cell killing efficacy of the therapy. We next demonstrate that mitochondrial-morphology-induced scattering changes in cells whose lysosomes are insulted by PDT serves as a predictor of cytochrome c release, which is a biochemical signal for the induction of programmed cell death. Motivated by these experiments, we then report on the design, construction, and preliminary data from a multifunctional scattering microscopy system capable of exploiting the findings of this thesis in a biology-relevant platform.

## **Table of Contents**

Curriculum Vitae .....	<i>ii</i>
Acknowledgements .....	<i>v</i>
Abstract .....	<i>viii</i>
Table of Contents .....	<i>x</i>
List of Tables .....	<i>xvi</i>
List of Figures .....	<i>xvii</i>
<b>Chapter 1. Introduction .....</b>	<b>1</b>
1.1. Cell and organelle size and function .....	1
1.2. Photodynamic therapy .....	3
1.3. Organelle morphology, cell death pathways, and disease markers .....	5
1.4. Brief review of the literature on light scattering from biological cells .....	8
1.5. Overview of the thesis .....	10
References .....	14
<b>Chapter 2. Review of light scattering from particles with sizes comparable to the wavelength of incident light .....</b>	<b>18</b>
2.1. Introduction .....	18
2.2. Formulation of the basic scattering problem .....	19
2.3. Scattering, absorption, and extinction cross sections .....	24
2.4. Analytical solutions to the scattering problem .....	29

2.4.1. Separation of variables .....	29
2.4.2. Mie Theory .....	33
2.4.3. Scattering from a coated sphere .....	35
2.4.4. T matrix and extended boundary condition .....	38
2.5. Matrix elements and cross sections .....	44
2.6. Effects of particle size, shape, refractive index, and ensemble averaging on $\sigma_{\text{sca}}$ and $d\sigma_{\text{sca}}/d\Omega$ .....	46
2.7. Discussion .....	52
References .....	54
<b>Chapter 3. Mie theory interpretations of light scattering from intact cells .....</b>	<b>55</b>
3.1. Introduction .....	55
3.2. Construction of a goniometer .....	56
3.3. Cell culture and sample preparation .....	58
3.4. Scattering from polystyrene microspheres .....	58
3.5. Scattering phase function from an ensemble of particles .....	62
3.6. Interpretations of scattering from intact cells through $\sigma_p$ .....	64
3.7. Discussion .....	74
References .....	76
<b>Chapter 4. Light scattering from intact cells reports oxidative-stress-induced changes in mitochondrial morphology .....</b>	<b>77</b>
4.1. Introduction .....	77
4.2. Materials and methods .....	79

4.2.1. Cell culture and photodynamic treatment .....	79
4.2.2. Isolation of mitochondria .....	81
4.2.3. Angularly resolved light scattering .....	82
4.2.4. Electron microscopy methods .....	82
4.2.5. Coated sphere modeling and fitting .....	83
4.3. Results .....	84
4.3.1. Scattering measurements from suspensions of intact cells .....	84
4.3.2. Scattering results from isolated mitochondria .....	86
4.3.3. Electron microscopy results .....	86
4.3.4. Scattering results for photodynamically-treated cells .....	91
4.4. Discussion .....	95
References .....	103

**Chapter 5. Index-of-refraction-dependent light scattering observed  
with organelle-localizing dyes .....106**

5.1. Introduction .....	106
5.2. Materials and methods .....	109
5.2.1. Organelle localizing dyes .....	109
5.2.2. Cell culture and staining .....	111
5.3.3 Fluorescence spectroscopy .....	112
5.2.4. Angularly-resolved light scattering measurements .....	112
5.2.5. Darkfield scattering spectroscopy measurements .....	114
5.2.6. Mie theory fitting to angularly resolved light scattering data .....	118

5.3. Results .....	121
5.3.1. Angularly resolved light scattering in the presence of NPe6 .....	121
5.3.2. Darkfield spectroscopy .....	123
5.3.3. Modeling complex refractive index .....	125
5.3.4. Angularly resolved scattering in the presence of HPPH .....	130
5.3.5. Fits to angularly resolved measurements .....	132
5.3.6. Scattering results from cells stained with Mito- and LysoTracker dyes .....	136
5.4. Discussion .....	138
References .....	144
<b>Chapter 6. Characterization of the lysosomal contribution to whole- cell scattering as quantified by photodynamic organelle ablation .....</b>	<b>147</b>
6.1. Introduction .....	147
6.2. Materials and methods .....	148
6.3. Results and discussion .....	149
References .....	160
<b>Chapter 7. Biological implications of mitochondrial-morphology- induced light scattering changes .....</b>	<b>161</b>
7.1. Introduction .....	161
7.2. Coated sphere swelling parameter and cell survival in Pc 4-PDT .....	162
7.2.1. Introduction .....	162
7.2.2. Materials and methods .....	163
7.2.2.1. Cell culture and Pc 4-PDT protocols .....	163
7.2.2.2. Light scattering measurements and models .....	164

7.2.2.3. Clonogenic cell survival assay .....	164
7.2.3. Results .....	165
7.2.3.1. Scattering results .....	165
7.2.3.2. Clonogenic cell survival results .....	167
7.2.4. Discussion .....	169
7.3. Lysosome-damage-induced mitochondrial scattering changes coincide with release of cytochrome c .....	171
7.3.1. Introduction .....	171
7.3.2. Materials and methods .....	172
7.3.2.1. Cell culture and NPe6-PDT protocol .....	172
7.3.2.2. Light scattering measurements and modeling .....	172
7.3.2.3. Cytochrome c release assay .....	173
7.3.3. Results .....	174
7.3.3.1. Scattering results .....	174
7.3.3.2. Cytochrome c assay results .....	177
7.3.4. Discussion .....	179
7.4. Summary .....	179
References .....	181
<b>Chapter 8. An inverted microscope enabling multi-modality imaging, angle-resolved scattering, and spectroscopy .....</b>	<b>183</b>
8.1. Introduction .....	183
8.2. Fourier plane in an imaging system .....	184
8.3. Instrument design and construction .....	186

8.4. Instrument calibrations and corrections .....	190
8.5. Verification of instrumentation with a model system .....	192
8.6. Data from intact EMT6 cells .....	196
8.7. Discussion .....	198
References .....	200
<b>Appendix. Details of the goniometer experiment .....</b>	<b>201</b>
A.1. Introduction .....	201
A.2. Critical experimental components .....	201
A.3. System alignment protocol .....	204
A.4. Hardware and software settings .....	206
A.5. Data acquisition .....	207
A.6. Limitations on measurements .....	208

## List of Tables

3.1. Parameters returned from Mie theory fits to scattering data from intact cells .....	68
5.1. Summary of parameters returned from absorbing-sphere fits to control and NPe6-stained cells .....	137
6.1. Summary of parameters returned from fits to control and NPe6-PDT-treated cells .....	154

## List of Figures

1.1. Size scales of cells and sub-cellular structures .....	2
1.2. Typical cell death pathways .....	7
2.1. Schematic of the basic scattering problem .....	20
2.2. Geometry used to describe the incident and scattered fields .....	22
2.3. An ideal experimental system with which to measure extinction .....	25
2.4. Geometry for the scattering problem of a homogenous sphere .....	34
2.5. Geometry for the scattering problem of a coated sphere .....	36
2.6. Geometry for extended boundary condition T matrix calculations .....	41
2.7. Mie theory calculations demonstrating the effects of particle size and refractive index on angular scattering .....	45
2.8. Mie theory calculations demonstrating the effects of ensemble averaging of particles of different sizes on angular scattering .....	47
2.9. T matrix calculations demonstrating the effects of particle shape versus particle size on angular scattering .....	49
2.10. T matrix calculation demonstrating the effects of particle shape on the total scattering cross section .....	51
3.1. Block diagram of the goniometer experiment .....	57
3.2. Angularly resolved light scattering data from microspheres .....	60
3.3. Relationship between $\rho(r)$ and $\sigma\rho(r)$ .....	63
3.4. Scattering data and Mie theory fits with different assumed functional forms of $\rho(r)$ .....	66

3.5. Sampling of Gaussian distributions with negative means .....	69
3.6. $\sigma\rho(r)$ for four different functional forms of $\rho(r)$ .....	71
3.7. Comparison of our results with those of another leading laboratory .....	73
4.1. Scattering data from control and ALA-PDT-treated cells .....	85
4.2. Scattering data from isolated mitochondria .....	87
4.3. Size distributions measured from cells and from mitochondria .....	88
4.4. Histograms of ALA-PDT-treated and control mitochondrial size .....	90
4.5. Electron microscopy images of and dielectric models for control and ALA-PDT-treated mitochondria .....	92
4.6. Forward calculations of a homogenous-sphere swelling model plotted with ALA-PDT-treated cell data .....	94
4.7. Forward calculations of a water-based coated sphere swelling model plotted with ALA-PDT-treated cell data .....	96
4.8. Scattering data from ALA-PDT-treated cells and the cytosol-based coated-sphere fit .....	98
5.1. Fluorescence excitation and emission spectra for EMT6 cells loaded with NPe6 or HPPH .....	110
5.2. Schematic of the goniometer for multi-color angularly-resolved light scattering measurements .....	113
5.3. Schematic of the darkfield spectroscopy setup .....	116
5.4. Representative angularly-resolved light scattering for cells loaded with NPe6 and control cells at 488, 633, and 658 nm .....	122
5.5. Representative darkfield spectra for NPe6-loaded and control cells .....	124
5.6. Mie theory calculations of the mean scattering cross section versus the imaginary part of the refractive index .....	126

5.7. Mie theory calculations of the angular dependence of light scattering for particles with $n_r = 1.6$ and varying $n_i$ .....	128
5.8. Mie theory calculations of the angular dependence of light scattering for particles with $n_r = 1.4$ and varying $n_i$ .....	129
5.9. Representative angularly-resolved light scattering data for cells loaded with HPPH and control cells at 658 nm .....	131
5.10. Angularly-resolved light scattering data and absorbing-sphere fit .....	134
6.1. Fluorescence images of LysoTracker re-distribution in response to NPe6-PDT .....	150
6.2. Angularly-resolved light scattering data from intact control EMT6 cells and cells given $20 \text{ J cm}^{-2}$ NPe6-PDT .....	152
6.3. Plots of $\sigma_p$ returned from fits to control- and NPe6-treated-cells, respectively .....	156
6.4. Particle size distributions extracted from fits to scattering data .....	158
7.1. Angularly-resolved light scattering data and coated sphere fits to data from Pc 4-PDT-treated EMT6 cells in suspension .....	166
7.2. Time course of swelling parameter for various fluences of 250 nM Pc 4-PDT .....	168
7.3. Clonogenic survival of EMT6 cells treated with 250 nM Pc 4-PDT at various fluences .....	170
7.4. Time course of angularly-resolved light scattering post $1 \text{ J cm}^{-2}$ NPe6-PDT .....	175
7.5. Results from cytochrome c imaging assay .....	178
8.1. Schematic of a single-lens imaging system .....	185
8.2. Schematic diagram of our system in imaging mode, Fourier plane imaging and angle resolved scattering mode, and scattering spectroscopic acquisition mode .....	187

8.3. Representative data from 4 $\mu\text{m}$ polystyrene microspheres from our system in imaging mode .....	191
8.4. Representative data from 2 and 4 $\mu\text{m}$ polystyrene microspheres with our system in Fourier imaging and angle resolved scattering mode .....	193
8.5. Representative data from 4 $\mu\text{m}$ polystyrene microspheres from our system in scattering spectroscopy mode .....	195
8.6. Representative data from EMT6 cell monolayers from our system in fluorescence imaging and angle-resolved scattering modes .....	197
A.1. Digital photograph of the Foster Laboratory goniometer experiment ....	202
A.2. Seven-step schematic for alignment of the goniometer experiment .....	205
A.3. Schematic explanation of the $\text{Sin}(\theta)$ correction to goniometer data .....	209
A.4. Schematic to demonstrate how back reflections can affect backscattering signal from angularly-resolved measurement.....	211

## **Chapter 1. Introduction**

This thesis consists of a collection of related studies aimed at discerning the biological and biophysical connection between light scattering signals from biological cells and these cells' morphological and biochemical status. To set the stage for later chapters, we first review some basic cell biology and sub-cellular morphology. As the majority of these studies are conducted in the context of photodynamic therapy, which is a cancer intervention whose goal is cell killing, we introduce the aspects of photodynamic therapy relevant to this thesis and discuss the biochemical and morphological aspects of cell death pathways. The status of light scattering in the literature is reviewed, and we conclude by providing an overview of the remaining chapters of this thesis.

### **1.1 Cell and organelle size and function**

In this section, we review the morphology and functions of some of the cellular sub-structures within mammalian cells at the level of the introductory text by Starr [1]. Biological cells are made up of several sub-structures known as organelles that are immersed in a fluid known as cytosol and packaged in the plasma membrane. These structures all have specific roles to play in the function of the cell, as well as characteristic size scales (please see figure 1.1). A whole mammalian cell is roughly 10-15  $\mu\text{m}$  in diameter. The largest organelle is the cell

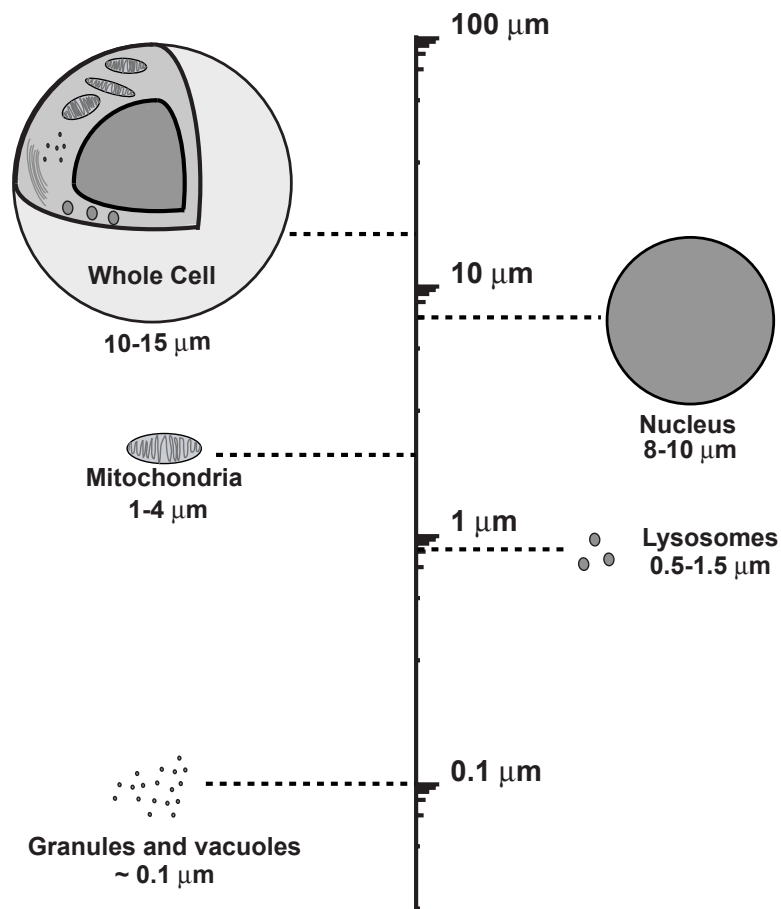


**Figure 1.1** Size scale of cells and sub-cellular structures. A whole cell is roughly 10-15  $\mu\text{m}$  in diameter. There is exactly one cell nucleus per cell, and these organelles are typically 8-10  $\mu\text{m}$  in diameter. The next largest organelles are the mitochondria, which are between 1-4  $\mu\text{m}$  in length, and roughly 0.5-1  $\mu\text{m}$  in width. The cell lysosomes are 0.5-1.5  $\mu\text{m}$  in diameter, and there are other smaller granules and vacuoles that are 100 nm or less.

---

nucleus, which is 8-10  $\mu\text{m}$  in diameter and contains the cell's genetic material. The second largest organelles within cells are the mitochondria, which are elongated ellipsoidal structures that are roughly 1-4  $\mu\text{m}$  along their major axis and 0.5 – 1  $\mu\text{m}$  along their minor axis. These organelles serve multiple functions within cells. Although their primary purpose is synthesis of ATP, which is the main chemical energy source for the cell, they are also involved in heme synthesis and play a vital role in most cell death pathways. In contrast to the cell nucleus, there are between  $10^0$  -  $10^5$  mitochondria per cell, depending on the cell type. These organelles are morphologically dynamic, and in their size and biochemistry mitochondria resemble bacteria. They have their own DNA, which they exchange with one another by mitochondrial fission and fusion, and the proper regulation of this process is vital to health.

There are many vesicles within cells, the most important of which are lysosomes, which are 0.5 - 1.5  $\mu\text{m}$  in diameter, and whose primary purpose is the digestion of cellular waste. These are highly acidic organelles and contain stores of enzymes and iron. There are several other organelle sites within cells such as the endoplasmic reticulum, the Golgi apparatus, and the cytoskeleton whose roles are beyond the scope of this thesis.

## 1.2 Photodynamic therapy

Photodynamic therapy (PDT) is a cancer intervention that uses a photosensitizing agent and visible light to damage tumors. In PDT, a drug, or

---

---

photosensitizer, is introduced into cells via incubation for in vitro experiments or by systemic or topical administration in a human or animal. These drugs, in the absence of light, typically have little to no toxicity and preferentially accumulate in tumor cells. Upon irradiation with light of an appropriate wavelength, the optically excited photosensitizer, in the presence of ground state oxygen, produces highly reactive singlet oxygen which is responsible for cell damage.

Many of these photosensitizers localize in, and upon irradiation deposit oxidative stress to, specific organelle sites within cells [2]. Drugs such as aminolevulinic acid (ALA)-induced protoporphyrin IX (PpIX), silicon phthalocyanine 4 (Pc 4), 2-[1-hexyloxyethyl]-2-divinyl pyropheophorbide-a (HPPH), benzoporphyrin derivative (BPD), and hematoporphyrin derivative (Photofrin®) localize primarily in the mitochondria. There are also drugs that localize to lysosomes, such as N-aspartyl chlorin e6 (NPe6), Lutetium texaphyrin (LuTex), and lysyl chlorine-p6 (LPC). Photosensitizers can also localize to the endoplasmic reticulum (such as meso-tetra(3-hydroxyphenyl)chlorin (mTHPC)) or to the plasma membrane (such as monocationic porphyrin (MCP)). The particular organelle site to which a drug localizes can determine the pathway by which a cell dies in response to the therapy, and sub-cellular localization has also been shown to correlate with cell-killing efficacy [2].

---

### **1.3 Organelle morphology, cell death pathways, and disease markers**

Subcellular morphology can be highly relevant to the fate of a damaged cell. Cells die primarily through two pathways, apoptosis and necrosis. Apoptosis, or programmed cell death, is an intrinsic cell suicide mechanism that involves distinct biochemical and morphological markers [3]. This pathway is triggered by most cell types when the cell is damaged irreversibly, and it undergoes a process in which the cell is dismantled and packaged for disposal by the immune system. The late-stage processes, which occur tens of hours post-insult, include DNA fragmentation, nuclear condensation, and the ‘blebbing’ off of apoptotic bodies. Apoptosis is of great interest in modern medicine and biology, as its dysregulation is linked to a variety of diseases such as cancer, AIDS, and neurological disorders [3]. Also, the ability of therapies to induce apoptotic versus necrotic cell death could have the potential to enhance their outcome [4]. Necrosis, for the most part, is defined as cell death that occurs when the cell is damaged sufficiently that the complex apoptotic signaling cannot proceed.

Most cell death pathways involve the mitochondria [5]. A schematic of some of these pathways is shown in figure 1.2. If the cell is treated with mitochondrial PDT, then oxidative stress is deposited directly to the mitochondria [6]. For lysosomal PDT, oxidative stress causes enzymes to be released from the lysosomes into the cytosol, and through a series of yet unproven events, the pro-

---

apoptotic Bcl-2 protein BID is cleaved to truncated-BID (t-BID) and attacks the mitochondrial membrane [7]. The mitochondria can also be insulted by other proapoptotic members of the Bcl-2 family such as BAX, by intracellular calcium, reactive oxygen species (ROS), activated caspases, and other stressors [5]. If a mitochondrion is sufficiently damaged, it will release cytochrome c from its membrane space into the cytosol, which is often accompanied by mitochondrial swelling. Once cytochrome c is released into the cytosol, it combines with APAF-1, ATP, procaspase-3, and procaspase-9 to form an apoptosome, which activates caspase-3 and caspase-9. Once these caspases are activated, they form a feedback loop by attacking other mitochondria within the cell, and are responsible for signaling the biochemical process culminating in apoptosis [5]. Due to this feedback loop, Goldstein et al. have shown that once cytochrome c is released from a single mitochondrion within a cell, the rest of that cell's mitochondria will release their cytochrome c within approximately 5 minutes [8].

Once cytochrome c is released from a mitochondrion, the cell will die. Even if the cell is damaged sufficiently that the process of apoptosis is unable to proceed to completion, all of the mitochondria within the cell will release their cytochrome c, which is a crucial part of the mitochondrial electron transport chain. When the electron transport chain breaks down, there is a buildup of ROS, followed by the inability of mitochondria to produce ATP leading to loss of cell function [5].

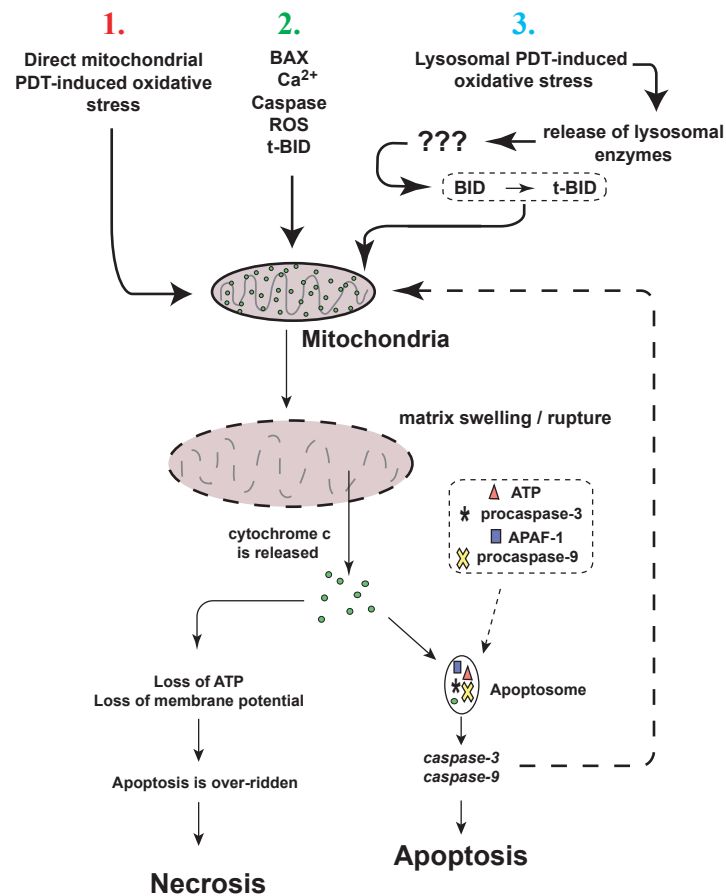


**Figure 1.2.** Typical cell death pathways for cells insulted by mitochondrial PDT (1), a variety of other common insults (2), and for lysosomal PDT (3). Once the insult reaches a mitochondrion, cytochrome c is released and is often accompanied by mitochondrial swelling. The cytochrome c combines with ATP, APAF-1, procaspase-3, and procaspase-9 to form an apoptosome, which activates caspase-3 and caspase-9. The activated caspases then cause cytochrome c release from other cellular mitochondria, as well as initiate biochemical signaling leading to apoptotic cell death. If this mechanism is overwhelmed, the mitochondria lose the ability to generate ATP and the cell dies through necrotic cell death.

---

Organelle morphology changes other than stress-induced mitochondrial swelling are associated with and can serve as markers for a variety of diseases. The morphology of the nucleus is important in the diagnosis of pre-cancerous conditions. In many pre-cancerous epithelial tissues, the nuclei become both enlarged and crowded, and when stained for pathology they take up larger quantities of certain dyes [9]. Mitochondrial morphology changes accompanying dysfunctional mitochondria are associated with a number of human diseases including blindness [10,11], deafness [12], diabetes [13], neurodegeneration [14], and are associated with the aging process [15].

## **1.4 Brief review of the literature on light scattering from biological cells**

Extraction of morphological information from intact cells using light scattering measurements has existed for years. In flow cytometry, light scattered into forward angles ( $0.5\text{-}2^\circ$ ) was first used to measure cell size by Mullaney et al. [16]. Salzman et al. [17] extended this to measurements of forward-scattering ( $1 \pm 0.1^\circ$ ) and side-scattering ( $90 \pm 12^\circ$ ) and could use these to distinguish different cell types.

Optical transmission measurements of isolated mitochondria have long been used as a tool in biology and biochemistry to quantify mitochondrial morphology changes. These measurements simply used the optical density of mitochondrial suspensions at wavelengths where absorption was minimal. These types of studies enlightened the role of ADP in the regulation of metabolic and

---

---

structural states of mitochondria [18] and the role of ATP in reversing various types of mitochondrial swelling [19].

Rigorous measurements of light scattering from sub-cellular structures within intact cells originated less than ten years ago with the idea of light scattering spectroscopy that was introduced by Perelman et al. [20]. In that report, the authors observed a periodic fine structure on top of the wavelength-resolved diffuse reflectance signal from epithelial tissue. Employing a Rayleigh-Gans approximation, the authors were able to extract nuclear size distributions. The instrumentation for these wavelength-resolved backscattering measurements was further extended by Backman et al. [21] to include polarization selection to discriminate between singly- and multiply-scattered light, and a Mie theory model was adopted to describe their data. This technique successfully eliminated multiply-scattered light, but the measurement was restricted to cells on the surface of tissues. This limitation was overcome by Wax et al. [22] who combined angle-resolved backscattering measurements with low coherence interferometry to create a depth-sensitive measurement of nuclear size within tissues.

There have also been several reports of light scattering measurements from intact cells in vitro to assess sub-cellular morphology. In the backscattering geometry, Schuele et al. [23] were able to quantify sub-cellular constituents from within intact cells that agreed qualitatively with electron microscopy (EM), and further claimed to observe a mitochondrial index of refraction change in response to thermal stress. In the forward scattering geometry, Mourant et al. [24]

---

---

measured angularly-resolved forward-scattered light from intact cells and from multi-cellular spherical aggregates of cells (spheroids) and concluded that in the angular range of  $15\text{-}110^\circ$ , sub-cellular structures dominated light scattering. In another paper, Mourant et al. [25] modeled angularly-resolved light scattering from intact cells within a Mie theory model and concluded that scattering from intact cells is dominated by particles that are on the order of 100 nm.

Incorporating forward scattering measurements into an optical scattering ratiometric imaging (OSIR) microscope, Boustany et al. [26] reported an intracellular-calcium-induced scattering change from intact cells that the authors attributed to mitochondrial rounding. In a later report, Boustany et al. [27] used their OSIR microscope to measure both intact cells and cells transfected to over-express the anti-apoptotic Bcl-2 protein Bcl-XL, and claimed that the over-expression induced a morphology change in parallel with resistance to apoptosis.

Despite the number of researchers publishing their work in the field of biomedical light scattering, the contributions of individual organelle populations to the observed light scattering signals are poorly understood. In order for light scattering measurements to be relevant to modern biology or medicine, this connection must be established.

## **1.5 Overview of the thesis**

In Chapter 2, we provide a review of light scattering theory for particles whose size scales are similar to the wavelength of incident light. We introduce

---

---

the basic scattering problem and discuss quantities of interest to the later chapters in generic terms. We then review solutions to the scattering problem for a homogenous sphere, an n-level coated sphere, and a homogenous particle of arbitrary shape. In the final section of Chapter 2, we provide some illustrative forward calculations that demonstrate the effects of particle size, shape, and index of refraction, as well as the effects of ensemble averaging of populations of light scattering particles.

In Chapter 3, we introduce our goniometer experiment for measuring angularly resolved light scattering and present models for inverting our data. We first look at scattering data from monodisperse polystyrene microspheres and present a model from which we can recover the size of these beads. We next develop a Mie theory interpretation of light scattering from a broad size distribution of particles and illustrate the power of this interpretation through applying it to measurements from intact cells. Portions of Chapter 3 have been published previously in [28] and [29], and co-authorship with Thomas H. Foster, Chad E. Bigelow, and David J. Calkins is gratefully acknowledged.

In Chapter 4, we present the results from an experiment in which we perturbed mitochondria within intact cells and observed corresponding light scattering signatures. We show that the details of the morphological changes to the mitochondria, as observed by electron microscopy, are faithfully reported in our light scattering data. We further develop a coated-sphere-based model for mitochondrial swelling in response to mitochondrial-targeted PDT. Portions of

---

---

Chapter 4 have been published previously [29], and co-authorship with Thomas H. Foster, Chad E. Bigelow, and David J. Calkins is gratefully acknowledged.

In Chapter 5, we report on the results of a set of experiments in which we stain specific organelle sites within cells with high-extinction dyes. We show that within a Mie theory model, the changes in scattering properties of a particle in response to the addition of an absorber depend heavily on its inherent refractive index. Through an absorbing-sphere Mie theory model, we show that the indices of refraction of lysosomes and mitochondria are significantly different, and that lysosomes have a much higher refractive index than has been reported for organelles in the literature. We further are able to extract estimates of lysosomal and mitochondrial size and their overall contribution to light scattering. Portions of Chapter 5 have been published previously [30], and co-authorship with William J. Cottrell and Thomas H. Foster is gratefully acknowledged.

In Chapter 6, we confirm the estimates of organelle sizes and contributions to light scattering by ablating the lysosomes in intact cells using a lysosomal PDT strategy. Observing light scattering pre- and post-ablation, we are able to fit a model to our data and place hard numbers on the estimates shown in Chapter 5. Portions of Chapter 6 were published previously [31], and co-authorship with Thomas H. Foster is gratefully acknowledged.

In Chapter 7, we report on a set of experiments that demonstrate the significance of our light scattering measurements to studies of cell death biology. In the first section, we show that changes in the swelling parameter from our

---

---

coated-sphere model for mitochondrial PDT corresponds to cell survival as quantified by colony forming assay. Portions of this section have been published [32], and co-authorship with Ken K-H. Wang, Soumya Mitra, Malcolm E. Kenney, and Thomas H. Foster is gratefully acknowledged. In the second section of this Chapter, we report that *mitochondrial* scattering changes following *lysosomal*-PDT coincide with the release of cytochrome c from the mitochondria. Portions of this section have been submitted for publication, and co-authorship with Benjamin R. Geisselman, Soumya Mitra, and Thomas H. Foster is gratefully acknowledged.

In Chapter 8, we present the design, construction, and initial testing of our multifunctional light scattering and fluorescence microscopy and spectroscopy system. We have designed and constructed instrumentation that is able to incorporate every experiment and model presented in the preceding Chapters at the focus of a standard inverted microscope, which makes great strides toward making light scattering measurements relevant to modern biology. Portions of this chapter have been submitted for publication, and co-authorship with William J. Cottrell and Thomas H. Foster is gratefully acknowledged.

---

---

## References

1. C. Starr, *Biology concepts and applications*, (Wadsworth Publishing Company, Belmont, CA, 1997).
2. D. Kessel, "Correlation between subcellular localization and photodynamic efficacy," *J. Porphyrins Phthalocyanines* **8**, 1009-1014 (2004).
3. A. Ashkenazi and V. M. Dixit, "Death receptors: signaling and modulation," *Science* **281**, 1305-1308 (1998).
4. N. L. Oleinick, R. L. Morris, and I. Belichenko, "The role of apoptosis in response to photodynamic therapy: what, where, why, and how," *Photochem. Photobiol. Sci.* **1**, 1-21 (2002).
5. D. R. Green and J. C. Reed, "Mitochondria and apoptosis," *Science* **281**, 1309-1312 (1998).
6. M. Lam, N. L. Oleinick, and A. L. Nieminen, "Photodynamic therapy-induced apoptosis in epidermoid carcinoma cells. Reactive oxygen species and mitochondrial inner membrane permeabilization," *J. Biol. Chem.* **276**, 47379-47386 (2001).
7. J. J. Reiners, Jr., J. A. Caruso, P. Mathieu, B. Chelladurai, X. M. Yin, and D. Kessel, "Release of cytochrome c and activation of pro-caspase-9 following lysosomal photodamage involves Bid cleavage," *Cell Death Differ.* **9**, 934-944 (2002).
8. J. C. Goldstein, C. Munoz-Pinedo, J. E. Ricci, S. R. Adams, A. Kelekar, M. Schuler, R. Y. Tsien, and D. R. Green, "Cytochrome c is released in a single step during apoptosis," *Cell Death Differ.* **12**, 453-462 (2005).
9. R. H. Riddell, H. Goldman, D. F. Ransohoff, H. D. Appelman, C. M. Fenoglio, R. C. Haggitt, C. Ahren, P. Correa, S. R. Hamilton, B. C. Morson, and ., "Dysplasia in inflammatory bowel disease: standardized classification with provisional clinical applications," *Hum. Pathol.* **14**, 931-968 (1983).
10. C. Delettre, G. Lenaers, J. M. Griffoin, N. Gigarel, C. Lorenzo, P. Belenguer, L. Pelloquin, J. Grosgeorge, C. Turc-Carel, E. Perret, C. Astarie-Dequeker, L. Lasquelles, B. Arnaud, B. Ducommun, J. Kaplan, and C. P. Hamel, "Nuclear gene OPA1, encoding a mitochondrial

- dynamamin-related protein, is mutated in dominant optic atrophy," *Nat. Genet.* **26**, 207-210 (2000).
11. C. Delettre, G. Lenaers, L. Pelloquin, P. Belenguer, and C. P. Hamel, "OPA1 (Kjer type) dominant optic atrophy: a novel mitochondrial disease," *Mol. Genet. Metab* **75**, 97-107 (2002).
  12. T. Yamasoba, Y. Goto, Y. Oka, I. Nishino, K. Tsukuda, and I. Nonaka, "Atypical muscle pathology and a survey of cis-mutations in deaf patients harboring a 1555 A-to-G point mutation in the mitochondrial ribosomal RNA gene," *Neuromuscul. Disord.* **12**, 506-512 (2002).
  13. T. Yu, J. L. Robotham, and Y. Yoon, "Increased production of reactive oxygen species in hyperglycemic conditions requires dynamic change of mitochondrial morphology," *Proc. Natl. Acad. Sci. U. S. A.* **103**, 2653-2658 (2006).
  14. P. A. Trimmer, R. H. Swerdlow, J. K. Parks, P. Keeney, J. P. Bennett, Jr., S. W. Miller, R. E. Davis, and W. D. Parker, Jr., "Abnormal mitochondrial morphology in sporadic Parkinson's and Alzheimer's disease hybrid cell lines," *Exp. Neurol.* **162**, 37-50 (2000).
  15. M. Jendrach, S. Pohl, M. Voth, A. Kowald, P. Hammerstein, and J. Bereiter-Hahn, "Morpho-dynamic changes of mitochondria during ageing of human endothelial cells," *Mech. Ageing Dev.* **126**, 813-821 (2005).
  16. P. F. Mullaney, M. A. Van Dilla, J. R. Coulter, and P. N. Dean, "Cell sizing: a light scattering photometer for rapid volume determination," *Rev. Sci. Instrum.* **40**, 1029-1032 (1969).
  17. G. C. Salzman, J. M. Crowell, J. C. Martin, T. T. Trujillo, A. Romero, P. F. Mullaney, and P. M. LaBauve, "Cell classification by laser light scattering: identification and separation of unstained leukocytes," *Acta Cytol.* **19**, 374-377 (1975).
  18. L. Packer, "Metabolic and structural states of mitochondria. I. Regulation by adenosine diphosphate," *J. Biol. Chem.* **235**, 242-249 (1960).
  19. A. L. Lehninger, "Reversal of various types of mitochondrial swelling by adenosine triphosphate," *J. Biol. Chem.* **234**, 2465-2471 (1959).
  20. L. T. Perelman, V. Backman, M. Wallace, G. Zonios, R. Manoharan, A. Nusrat, S. Shields, M. Seiler, C. Lima, T. Hamano, I. Itzkan, J. Van Dam, J. M. Crawford, and M. S. Feld, "Observation of periodic fine structure in

- 
- reflectance from biological tissue: A new technique for measuring nuclear size distribution," *Phys. Rev. Lett.* **80**, 627-630 (1998).
21. V. Backman, R. Gurjar, K. Badizadegan, L. Itzkan, R. R. Dasari, L. T. Perelman, and M. S. Feld, "Polarized light scattering spectroscopy for quantitative measurement of epithelial cellular structures in situ," *IEEE J. Sel. Top. in Quant. Electron.* **5**, 1019-1026 (1999).
  22. A. Wax, C. Yang, V. Backman, K. Badizadegan, C. W. Boone, R. R. Dasari, and M. S. Feld, "Cellular organization and substructure measured using angle-resolved low-coherence interferometry," *Biophys. J.* **82**, 2256-2264 (2002).
  23. G. Schuele, E. Vitkin, P. Huie, C. O'Connell-Rodwell, D. Palanker, and L. T. Perelman, "Optical spectroscopy noninvasively monitors response of organelles to cellular stress," *J. Biomed. Opt.* **10**, 051404 (2005).
  24. J. R. Mourant, T. M. Johnson, V. Doddi, and J. P. Freyer, "Angular dependent light scattering from multicellular spheroids," *J. Biomed. Opt.* **7**, 93-99 (2002).
  25. J. R. Mourant, T. M. Johnson, S. Carpenter, A. Guerra, T. Aida, and J. P. Freyer, "Polarized angular dependent spectroscopy of epithelial cells and epithelial cell nuclei to determine the size scale of scattering structures," *J. Biomed. Opt.* **7**, 378-387 (2002).
  26. N. N. Boustany, R. Drezek, and N. V. Thakor, "Calcium-induced alterations in mitochondrial morphology quantified in situ with optical scatter imaging," *Biophys. J.* **83**, 1691-1700 (2002).
  27. N. N. Boustany, Y. C. Tsai, B. Pfister, W. M. Joiner, G. A. Oyler, and N. V. Thakor, "BCL-xL-dependent light scattering by apoptotic cells," *Biophys. J.* **87**, 4163-4171 (2004).
  28. J. D. Wilson and T. H. Foster, "Mie theory interpretations of light scattering from intact cells," *Opt. Lett.* **30**, 2442-2444 (2005).
  29. J. D. Wilson, C. E. Bigelow, D. J. Calkins, and T. H. Foster, "Light scattering from intact cells reports oxidative-stress-induced mitochondrial swelling," *Biophys. J.* **88**, 2929-2938 (2005).
  30. J. D. Wilson, W. J. Cottrell, and T. H. Foster, "Index-of-refraction-dependent subcellular light scattering observed with organelle-specific dyes," *J. Biomed. Opt.* **12**, 014010 (2007).

- 
31. J. D. Wilson and T. H. Foster, "characterization of lysosomal contribution to whole-cell light scattering as quantified by photodynamic organelle ablation," *J. Biomed. Opt.* **12**, 030503, (2007).
  32. Wang K.K-H., J. D. Wilson, Kenney M.E., S. Mitra, and T. H. Foster, "Irradiation-induced enhancement of Pc 4 fluorescence and changes in light scattering are potential dosimeters for Pc 4-PDT," *Photochem. Photobiol.* DOI: 10.1111/j.1751-1097.2007.00128.x (2007).

## **Chapter 2. Review of light scattering from particles with sizes comparable to the wavelength of incident light**

### **2.1 Introduction**

We review light scattering from particles whose sizes are comparable to the wavelength of incident light. The scattering problem from particles in this size range ( $\sim 0.1$ - $10 \mu\text{m}$ ) cannot be treated within dipole or geometrical optics approximations and must be treated as a boundary value problem. We first introduce the generic scattering problem, and define quantities of interest in terms of scattered light from an arbitrary particle. We then outline methods to solve the boundary value problem from  $n$ -level spheres and from homogenous particles of arbitrary shape. The dependence of light scattering properties on particle size, composition, and shape are demonstrated through a series of illustrative forward calculations, and the implications for the studies presented in the rest of this document are discussed. This review borrows heavily from Bohren and Huffman [1], Mishchenko, Travis, and Lacis [2], and from Kahnert [3].

---

## 2.2 Formulation of the basic scattering problem

As the starting point in the generic light scattering problem, we assume that light is incident on a homogenous (i.e.  $\mu$ ,  $\varepsilon$  are constant) dielectric particle that is surrounded by a homogenous medium. A schematic is shown in figure 2.1. If the incident light is an infinite plane wave, we can write the incident electric and magnetic fields,  $\mathbf{E}_i$  and  $\mathbf{H}_i$ , as

$$\mathbf{E}_i(\mathbf{r}, t) = \mathbf{E}_0 \exp(i(\mathbf{k} \cdot \mathbf{r} - \omega t)), \quad (2.1)$$

$$\mathbf{H}_i(\mathbf{r}, t) = \mathbf{H}_0 \exp(i(\mathbf{k} \cdot \mathbf{r} - \omega t)). \quad (2.2)$$

Here the electric fields inside the particle are denoted  $\mathbf{E}_1$ ,  $\mathbf{H}_1$ , and the fields outside the particle are the sums of the incident and scattered fields as

$$\mathbf{E}_2 = \mathbf{E}_i + \mathbf{E}_s, \quad (2.3)$$

$$\mathbf{H}_2 = \mathbf{H}_i + \mathbf{H}_s. \quad (2.4)$$

We assume that there are no sources in space, meaning that  $\rho = 0$  and  $\mathbf{J} = 0$  for all  $\mathbf{r}$  and  $t$ , and we further assume that the scattering particle is a linear material (i.e.  $\mathbf{D} = \varepsilon \mathbf{E}$  and  $\mathbf{B} = \mu \mathbf{H}$ ). Then the Maxwell's equations for the system simplify to

$$\nabla \times \mathbf{H} = \varepsilon \frac{\partial \mathbf{E}}{\partial t}, \quad (2.5)$$

$$\nabla \times \mathbf{E} = -\mu \frac{\partial \mathbf{H}}{\partial t}, \quad (2.6)$$

$$\nabla \cdot \mathbf{E} = 0, \quad (2.7)$$

$$\nabla \cdot \mathbf{H} = 0. \quad (2.8)$$

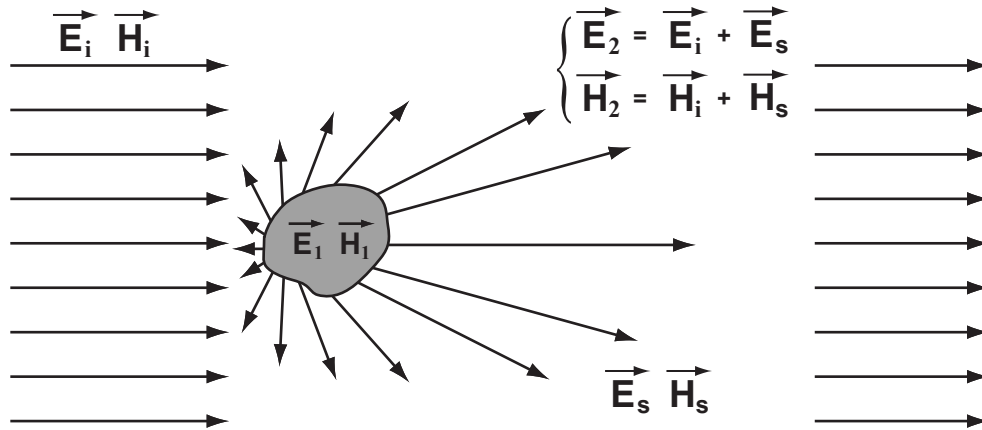


**Figure 2.1.** Schematic of the basic scattering problem. An infinite plane wave is incident on a scattering particle. We define the region of space inside the particle to be region 1, and outside the particle to be region 2. In region 2, the electric and magnetic fields are the sum of the incident and scattered fields.

By taking the curl of equation (2.6) and taking advantage of equations (2.1) and (2.5), we arrive at

$$\nabla \times \nabla \times \mathbf{E} = \omega^2 \epsilon \mu \mathbf{E}(\mathbf{r}). \quad (2.9)$$

Taking advantage of the identity  $\nabla \times \nabla \times \mathbf{X} = \nabla(\nabla \cdot \mathbf{X}) - \nabla^2 \mathbf{X}$ , and noting that  $\mathbf{E}$  is divergence free, we arrive at the familiar vector Helmholtz equation for the electric field,

$$[\nabla^2 + k(\mathbf{r})^2] \mathbf{E}(\mathbf{r}) = 0, \quad (2.10)$$

where  $k^2 = \omega^2 \mu \epsilon$ , or alternatively  $k^2 = (n\omega/c)^2$  where  $n$  is the refractive index and  $c$  is the speed of light. By similar reasoning, we arrive at the analogous equation describing the magnetic field

$$[\nabla^2 + k(\mathbf{r})^2] \mathbf{H}(\mathbf{r}) = 0. \quad (2.11)$$

These are elliptic differential equations that have to be solved subject to the boundary conditions that at the particle-medium interface the tangential components of the fields are continuous, which is written as

$$[\mathbf{E}_2(\mathbf{X}) - \mathbf{E}_1(\mathbf{X})] \times \hat{\mathbf{n}} = 0, \quad (2.12)$$

$$[\mathbf{H}_2(\mathbf{X}) - \mathbf{H}_1(\mathbf{X})] \times \hat{\mathbf{n}} = 0, \quad (2.13)$$

where  $\mathbf{X}$  is on the surface of the particle, and  $\hat{\mathbf{n}}$  is a unit vector normal to that surface.

We define a coordinate system centered on the scattering particle with the incident beam along the  $z$  axis, as shown in figure 2.2, and consider light scattered into the direction of  $\hat{\mathbf{r}}$ . We define the scattering plane as that containing the unit

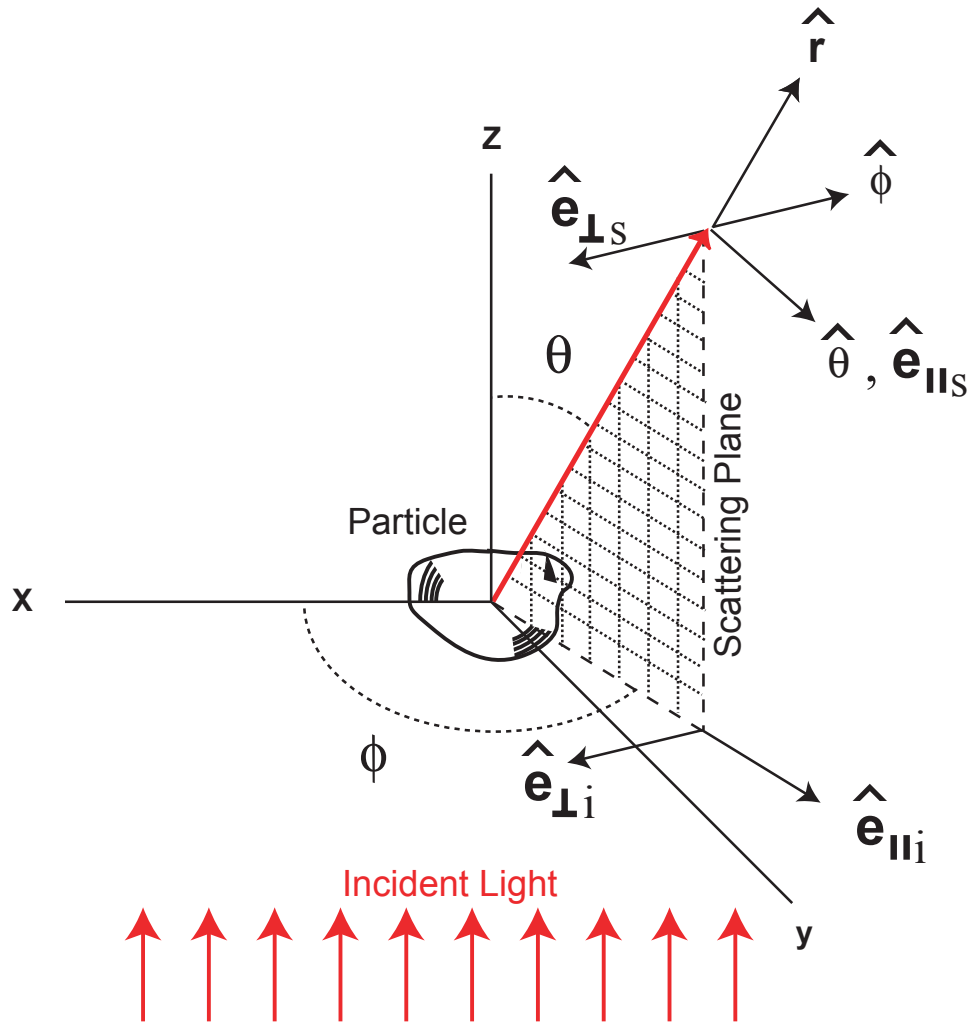


**Figure 2.2.** Geometry used to describe the incident and scattered fields. We let the z axis be the direction of propagation of the incident light, and define the scattering plane as that containing the z axis and the radius vector. We write the scattered fields in terms of a different basis than that used to describe the incident fields. Each of these basis sets has a unit vector that is parallel to and a unit vector that is perpendicular to the scattering plane.

vectors describing the direction of propagation of the scattered field,  $\hat{\mathbf{r}}$ , and that of the incident field,  $\hat{\mathbf{z}}$ . It is convention to write the incident electric field, which is parallel to the x-y plane, in terms of the unit vectors  $\hat{\mathbf{e}}_{\parallel i}$  and  $\hat{\mathbf{e}}_{\perp i}$ , which reside in the x-y plane and are parallel and perpendicular to the scattering plane, respectively. If we write the components of the incident electric field along the x and y axis as  $E_{xi}$  and  $E_{yi}$ , respectively, then the components of the electric field in the directions of  $\hat{\mathbf{e}}_{\parallel i}$  and  $\hat{\mathbf{e}}_{\perp i}$  are written

$$E_{\parallel i} = \cos \phi E_{xi} + \sin \phi E_{yi}, \quad (2.14)$$

$$E_{\perp i} = \sin \phi E_{xi} - \cos \phi E_{yi}. \quad (2.15)$$

Far from the scattering object, the scattered electric field is in the direction of some vector,  $\mathbf{A}$ , that is perpendicular to the  $\hat{\mathbf{r}}$  direction. In its asymptotic form we can write

$$\mathbf{E}_s \sim \frac{e^{ikr}}{-ikr} \mathbf{A}. \quad (2.16)$$

Again, it is useful to decompose the scattered electric field into an orthonormal basis that contains the scattering direction,  $\hat{\mathbf{r}}$ , and unit vectors  $\hat{\mathbf{e}}_{\parallel s}$  and  $\hat{\mathbf{e}}_{\perp s}$  which are parallel and perpendicular to the scattering plane, respectively. To maintain the same handedness as the basis vectors describing the incident field, we let  $\hat{\mathbf{e}}_{\parallel s} = \hat{\boldsymbol{\theta}}$ , and  $\hat{\mathbf{e}}_{\perp s} = -\hat{\boldsymbol{\phi}}$ . Then the scattered field is written

$$\mathbf{E}_s = E_{\parallel s} \hat{\mathbf{e}}_{\parallel s} + E_{\perp s} \hat{\mathbf{e}}_{\perp s}. \quad (2.17)$$

---

Due to the linearity of Maxwell's equations (2.5-2.8) and the boundary conditions (2.12, 2.13), we can write the scattered electric field as a linear transformation of the incident electric field as

$$\begin{bmatrix} E_{\parallel s} \\ E_{\perp s} \end{bmatrix} = \frac{e^{ikr}}{-ikr} \begin{bmatrix} S_2 & S_3 \\ S_4 & S_1 \end{bmatrix} \begin{bmatrix} E_{\parallel i} \\ E_{\perp i} \end{bmatrix}, \quad (2.18)$$

where the matrix elements,  $S_j$ , of the matrix  $\vec{\tilde{S}}$  depend on the polar angle,  $\theta$ , and the azimuthal angle,  $\phi$ , and contain all of the information about the particle's size and shape as well indices of refraction of the particle and surrounding medium. At the heart of solving the scattering problem is the calculation of these four (angular-dependant) matrix elements. In the scattering matrix from randomly oriented particles,  $S_3 = S_4$ , and in the particular case of scattering from a sphere,  $S_3 = S_4 = 0$ .

### 2.3 Scattering, absorption, and extinction cross sections

Suppose that we have an idealized experimental setup shown in figure 2.3. Here we have a perfectly collimated light source whose power is measured by a detector through a lens and aperture in such a way that any off-axis light is rejected. In the absence of any scattering particles in our light path, we measure an intensity of  $I_o$  at the detector. If we introduce a particle into the beam path, the detector will measure a smaller intensity,  $I$ . The difference between  $I_o$  and  $I$  is due to both the *scattering* of light out of the beam path as well as by *absorption* of

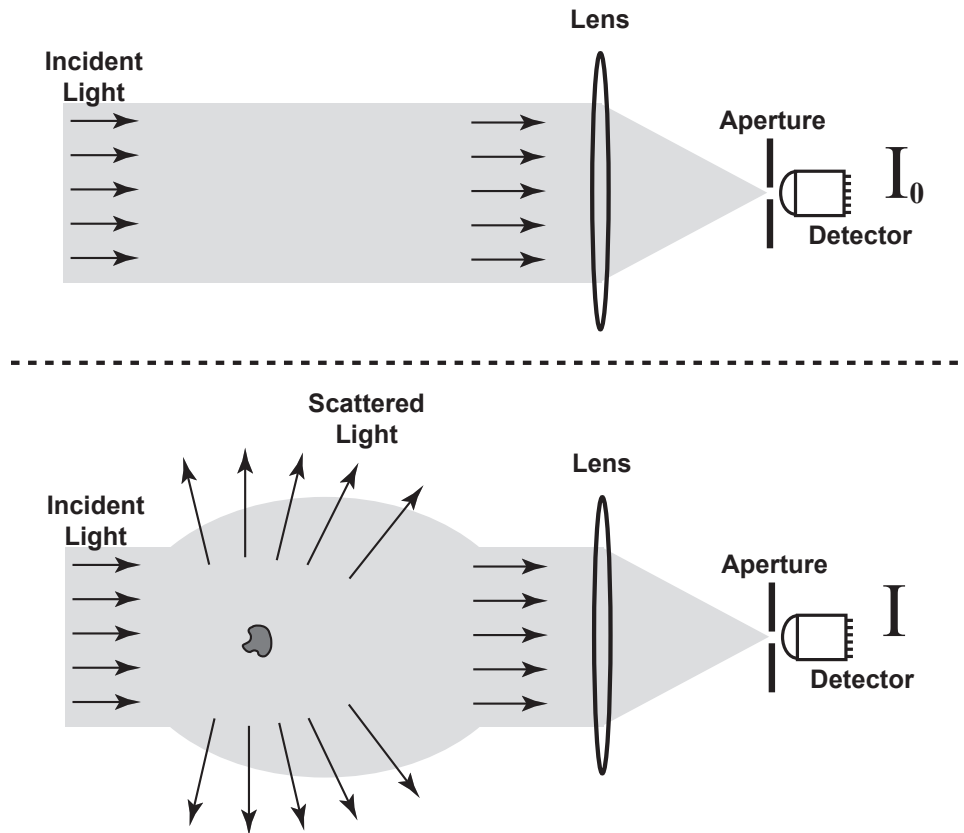


**Figure 2.3.** An ideal experimental system in which we have a perfectly collimated light source and a detection system that collects all of the incident light, and rejects any light that has any angular divergence. In the absence of any particles in the light path, the detector measures  $I_0$ . With a particle in the light path, the detector measures  $I < I_0$ , with the difference due to both light absorbed by the particle, and light scattered out of the detection aperture.

light by the particles and is collectively called *extinction*. Once we have calculated the scattered fields, we can account for these three quantities explicitly.

Let us examine the case in which we have one scattering particle centered at the origin and illuminated by an infinite plane wave propagating in the direction of  $\hat{\mathbf{z}}$  such as that shown in figure 2.2. We further assume that we have already calculated the scattering matrix,  $\vec{\mathbf{S}}$ , from equation (2.18). From the incident and scattered fields, we can calculate the time averaged rate of energy flux for regions of space outside of the particle, or the Poynting vector, which we will call  $\mathbf{P}$  to avoid confusion with the scattering matrix, as

$$\mathbf{P} = \frac{1}{2} \text{Re} \left\{ (\mathbf{E}_i + \mathbf{E}_s) \times (\mathbf{H}_i + \mathbf{H}_s)^* \right\}. \quad (2.19)$$

The external Poynting vector is the sum of the Poynting vectors for the incident and scattered fields, as well as a third term consisting of mixed fields that we will call the extinction term as

$$\mathbf{P}_s = \frac{1}{2} \text{Re} \left\{ \mathbf{E}_s \times \mathbf{H}_s^* \right\}, \quad (2.20)$$

$$\mathbf{P}_i = \frac{1}{2} \text{Re} \left\{ \mathbf{E}_i \times \mathbf{H}_i^* \right\}, \quad (2.21)$$

$$\mathbf{P}_{ext} = \frac{1}{2} \text{Re} \left\{ \mathbf{E}_s \times \mathbf{H}_i^* + \mathbf{E}_i \times \mathbf{H}_s^* \right\}. \quad (2.22)$$

Let us assume that the scattering particle is surrounded in a non-absorbing medium. Consider a sphere centered at the origin whose radius is much greater than the dimensions of the particle. Then we can calculate the net rate of energy

flux across the sphere by integrating the Poynting vector over the surface of the sphere as

$$W_a = -\int_{\substack{sphere \\ surface}} \mathbf{P} \cdot \hat{\mathbf{r}} dA, \quad (2.23)$$

where we have placed a negative sign in front of the integral to define a positive quantity. If  $W_a$  is negative, then we created energy within our sphere which is unphysical (i.e. the particle is spontaneously radiating!). We added the subscript, a, because this net *loss* of energy cannot come from scattering, and must be due to absorption from the particle. But from equations (2.19-2.22), we can see that

$W_a = W_i - W_s + W_{ext}$  where

$$W_i = -\int_{\substack{sphere \\ surface}} \mathbf{P}_i \cdot \hat{\mathbf{r}} dA, \quad (2.24)$$

$$W_s = \int_{\substack{sphere \\ surface}} \mathbf{P}_s \cdot \hat{\mathbf{r}} dA, \quad (2.25)$$

$$W_{ext} = -\int_{\substack{sphere \\ surface}} \mathbf{P}_{ext} \cdot \hat{\mathbf{r}} dA. \quad (2.26)$$

We have chosen the sign convention for  $W_s$  as this quantity reflects the scattered energy radiating out of the sphere. As the incident Poynting vector is independent of the scattering particle, by conservation of energy  $W_i = 0$ . Then we can see that the extinction rate,  $W_{ext}$ , is simply the sum of the absorption and scattering energy rates, or

$$W_{ext} = W_a + W_s. \quad (2.27)$$

In the far-field, our scattered electric field is as written in equation (2.16) with

$$\mathbf{A} = \vec{\mathbf{S}} \cdot \mathbf{E}_i. \quad (2.28)$$

If we plug the electric and magnetic fields into equation (2.26) and evaluate the integral, we get the result known as the optical theorem,

$$W_{ext} = \frac{4\pi}{k^2} \operatorname{Re} \left\{ \left( \mathbf{E}_i^* \cdot \mathbf{A} \right) \Big|_{\theta=0} \right\}, \quad (2.29)$$

which has units of irradiance multiplied by area. It is common to speak of the extinction cross section, or the rate of energy loss per unit irradiance, which is written

$$\sigma_{ext} = \frac{4\pi}{k^2 |\mathbf{E}_i|^2} \operatorname{Re} \left\{ \left( \mathbf{E}_i^* \cdot \mathbf{A} \right) \Big|_{\theta=0} \right\}. \quad (2.30)$$

Similarly, we can write the scattering cross section, or the amount of light scattered per unit irradiance, as

$$\sigma_{sca} = \int_{4\pi} \frac{|\mathbf{A}|^2}{k^2 |\mathbf{E}_i|^2} d\Omega. \quad (2.31)$$

It follows from equation (2.27) that we can write the absorption cross section as

$$\sigma_a = \sigma_{ext} - \sigma_s. \quad (2.32)$$

A quantity that will be of great interest in later chapters is the integrand of equation (2.31), the differential scattering cross section,

$$\frac{d\sigma_{sca}}{d\Omega} = \frac{|\mathbf{A}|^2}{k^2 |\mathbf{E}_i|^2}, \quad (2.33)$$

---

which is the angular distribution of scattered light. As angle-resolved measurements of absolute scattering intensity are often difficult, these measurements are often modeled as a phase function,

$$P(\theta, \phi) = \frac{1}{\sigma_{sca}} \frac{d\sigma_{sca}}{d\Omega}, \quad (2.34)$$

which is the angular distribution of scattered light that is normalized such that

$$\int_{4\pi} P(\theta, \phi) d\Omega = 1. \quad (2.35)$$

## 2.4 Analytical solutions to the scattering problem

### 2.4.1 Separation of variables

One of the most common approaches to solving the scattering problem is to use the separation of variables method (SVM). From equation (2.10), any suitable electric field must satisfy the vector Helmholtz equation. The strategy behind the SVM approach is to find solutions to the *scalar* Helmholtz equation by separation of variables, and from these solutions to construct vector wave functions that are solutions to the *vector* Helmholtz equation. From there, the incident, scattered, and internal fields can then be expanded in these vector functions, and the expansion coefficients are determined by the boundary conditions in equation (2.12).

In spherical coordinates, the scalar Helmholtz equation is written

$$\left[ \frac{1}{r} \frac{\partial^2}{\partial r^2} r + \frac{1}{r^2 \sin \theta} \frac{\partial}{\partial \theta} \sin \theta \frac{\partial}{\partial \theta} + \frac{1}{r^2 \sin^2 \theta} \frac{\partial^2}{\partial \phi^2} + k^2 \right] \psi = 0. \quad (2.36)$$

Solutions to this equation are found by assuming  $\psi$  is a product of radial, polar, and azimuthal functions as

$$\psi(r, \theta, \phi) = R(r)\Theta(\theta)\Phi(\phi). \quad (2.37)$$

Under this assumption, we obtain three ordinary differential equations

$$\left[ \frac{d^2}{dr^2} + k^2 - \frac{n(n+1)}{r^2} \right] rR = 0, \quad (2.38)$$

$$\left[ \frac{1}{\sin \theta} \frac{d}{d\theta} \sin \theta \frac{d}{d\theta} + n(n+1) - \frac{m^2}{\sin^2 \theta} \right] \Theta = 0, \quad (2.39)$$

$$\left[ \frac{d^2}{d\phi^2} + m^2 \right] \Phi = 0, \quad (2.40)$$

where  $m^2$  and  $n(n+1)$  are separation constants. The solutions to equations (2.38-2.40) are well known. The solutions to the radial equation,  $R(r) = z_n^{(j)}(r)$ , are the spherical Bessel functions ( $j=1$ ), the spherical Neumann functions ( $j=2$ ), and spherical Hankel functions of the first and second kind ( $j=3, 4$ , respectively) where  $n$  is a non-negative integer. Solutions to the polar equation,  $\Theta(\theta) = P_n^m(\theta)$ , are the associated Legendre functions where  $m = -n, -n+1, \dots, n-1, n$ . The even and odd solutions to the azimuthal equation are  $\Phi_e(\phi) = \cos(m\phi)$  and  $\Phi_o(\phi) = \sin(m\phi)$ , respectively. Then solutions to equation (2.36) take on the form

$$\psi_{e,m,n}^{(j)}(r, \theta, \phi) = z_n^{(j)} P_m^n(\theta) \cos(m\phi). \quad (2.41)$$

$$\psi_{o,m,n}^{(j)}(r, \theta, \phi) = z_n^{(j)} P_m^n(\theta) \sin(m\phi) \quad (2.42)$$

Now that we know that  $\psi$  is a solution to the scalar Helmholtz function, we can construct the functions

$$\mathbf{M}_{\{e,o\},m,n}^{(j)} = \nabla \times (\mathbf{r}\psi_{\{e,o\},m,n}^{(j)}), \quad (2.43)$$

$$\mathbf{N}_{\{e,o\},m,n}^{(j)} = \frac{1}{k} \nabla \times \mathbf{M}_{\{e,o\},m,n}^{(j)}, \quad (2.44)$$

that are solutions to the vector Helmholtz equation. These orthonormal functions are known as the vector spherical harmonics.

We now have a set of functions from which we can expand the incident electric field. For simplicity, let us assume that the plane wave is propagating in the  $\hat{\mathbf{z}}$  direction, and the electric field is x-polarized. In spherical coordinates, our electric field is written

$$\mathbf{E}_i = E_0 e^{ikr \cos \theta} (\sin \theta \cos \phi \hat{\mathbf{r}} + \cos \theta \cos \phi \hat{\boldsymbol{\theta}} - \sin \phi \hat{\boldsymbol{\phi}}). \quad (2.45)$$

As this plane wave must be well-behaved at the origin, we expand the incident electric field in vector harmonics with spherical Bessel functions describing the radial component. We then write

$$\mathbf{E}_i = \sum_{n=0}^{\infty} \sum_{m=-n}^n (B_{emn} \mathbf{M}_{emn}^{(1)} + B_{omn} \mathbf{M}_{omn}^{(1)} + A_{omn} \mathbf{N}_{omn}^{(1)} + A_{emn} \mathbf{N}_{emn}^{(1)}), \quad (2.46)$$

where the expansion coefficients are determined the usual way as

$$A_{omn} = \frac{\int_{4\pi} \mathbf{E}_i \cdot \mathbf{N}_{omn} d\Omega}{\int_{4\pi} \mathbf{N}_{omn} \cdot \mathbf{N}_{omn} d\Omega}, \quad (2.47)$$

with analogous expressions for  $B_{omn}$ ,  $A_{emn}$ , and  $B_{emn}$ . Evaluating these integrals, we find that  $A_{omn}$  and  $B_{emn}$  vanish for all  $m$  and  $n$ , and further that the remaining

coefficients vanish except when  $m = 1$ . The final expanded form of the incident electric field is

$$\mathbf{E}_i = E_0 \sum_{n=1}^{\infty} i^n \frac{2n+1}{n(n+1)} (\mathbf{M}_{oln}^{(1)} - i\mathbf{N}_{eln}^{(1)}), \quad (2.48)$$

and by taking the curl of equation (2.48), we get the corresponding magnetic field

$$\mathbf{H}_i = \frac{-k}{\omega\mu} E_0 \sum_{n=1}^{\infty} i^n \frac{2n+1}{n(n+1)} (\mathbf{M}_{eln}^{(1)} + i\mathbf{N}_{oln}^{(1)}). \quad (2.49)$$

The forms of equations (2.48) and (2.49) dictate the forms of the expansions of the internal fields,  $\mathbf{E}_1$ ,  $\mathbf{H}_1$ , and the scattered fields  $\mathbf{E}_s$ ,  $\mathbf{H}_s$ . As the internal fields have to be finite at the origin, then we again use the Bessel functions for the radial dependence. As the scattered field must asymptotically approach equation (2.16), we must use the spherical Hankel functions to describe the radial dependence. Both the spherical Hankel functions of the first and second kind have the correct asymptotic form, but functions of the first kind describe an outgoing spherical wave and those of the second kind describe an incoming wave. Thus on physical grounds we expand our scattered fields using the spherical Hankel functions of the first kind, and our internal and scattered fields take the form

$$\mathbf{E}_1 = \sum_{n=1}^{\infty} E_n (c_n \mathbf{M}_{oln}^{(1)} - i d_n \mathbf{N}_{eln}^{(1)}) \quad (2.50)$$

$$\mathbf{H}_1 = \frac{-k}{\omega\mu} \sum_{n=1}^{\infty} E_n (d_n \mathbf{M}_{eln}^{(1)} + i c_n \mathbf{N}_{oln}^{(1)}), \quad (2.51)$$

$$\mathbf{E}_s = \sum_{n=1}^{\infty} E_n \left( ia_n \mathbf{M}_{o1n}^{(3)} - b_n \mathbf{N}_{e1n}^{(3)} \right), \quad (2.52)$$

$$\mathbf{H}_s = \frac{-k}{\omega\mu} \sum_{n=1}^{\infty} E_n \left( ib_n \mathbf{M}_{e1n}^{(3)} + a_n \mathbf{N}_{o1n}^{(3)} \right). \quad (2.53)$$

Equations (2.50-2.53) are the starting point for calculating the scattered field using both the separation of variables method, as well as for other methods such as the T matrix formalism.

### 2.4.2 Mie theory

We now address the scattering problem of a homogenous dielectric sphere that is surrounded by a homogenous medium. The credit for the solution of this problem has been given to Gustav Mie for his 1908 paper, “Beiträge zur Optik trüber Medien, speziell kolloidaler Metallösungen,” (Leipzig, Ann. Phys. **330**, 377–445), and thus the solution is known as Mie theory. We consider the geometry shown in figure 2.4, with a spherical scattering center with radius  $a$ . We define region 1 to be inside the particle, and region 2 to be the surrounding medium.

We can now apply the boundary conditions from equations (2.12-2.13) to the equations for the incident, scattered, and internal fields expanded in vector harmonics (equations (2.50-2.53)) exploiting the spherical symmetry of the particle. We eventually arrive at a system of four equations in the four unknowns,

$$z_n^{(1)}(mx)c_n + z_n^{(3)}(x)b_n - z_n^{(1)}(x) = 0 \quad (2.54)$$

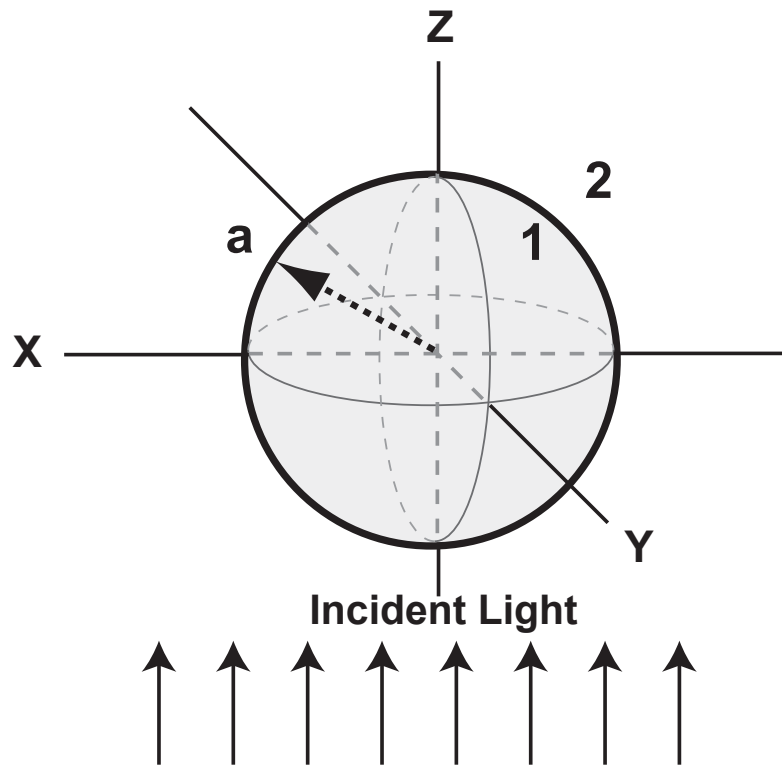


**Figure 2.4.** Geometry for the problem of light scattering by a homogenous spherical particle. A homogenous dielectric sphere of radius  $a$  is centered at the origin and surrounded by a homogenous dielectric medium. The scattering particle is illuminated by an infinite plane wave propagating along the  $z$  axis. We define region 1 to be inside the particle, and region 2 to be the surrounding medium.

$$\mu_2[mxz_n^{(1)}(mx)]'c_n + \mu_1[xz_n^{(3)}(x)]'b_n - \mu_1[[xz_n^{(1)}(x)]]' = 0 \quad (2.55)$$

$$\mu_2mz_n^{(1)}(mx)d_n + \mu_1z_n^{(3)}(x)a_n - \mu_1z_n^{(1)}(x) = 0 \quad (2.56)$$

$$[mxz_n^{(1)}(mx)]'d_n + m[xz_n^{(3)}(x)]'a_n - m[xz_n^{(1)}(x)]' = 0 \quad (2.57)$$

where the prime denotes differentiation with respect to the radial function's argument,  $x = k_2a$  is known as the size parameter, and  $m = k_1/k_2$  which simplifies to the relative refractive index of the particle to the surrounding medium,  $n_1/n_2$ . If we assume that  $\mu_1 = \mu_2$ , and define the functions

$$\psi_n(\nu) = \nu z_n^{(1)}(\nu), \quad (2.58)$$

$$\xi_n(\nu) = \nu z_n^{(3)}(\nu), \quad (2.59)$$

then solving equations (2.54-2.57) for the expansion coefficients we can write

$$a_n = \frac{m\psi_n(mx)\psi_n'(x) - \psi_n(x)\psi_n'(mx)}{m\psi_n(mx)\xi_n'(x) - \xi_n(x)\psi_n'(mx)}, \quad (2.60)$$

$$b_n = \frac{\psi_n(mx)\psi_n'(x) - m\psi_n(x)\psi_n'(mx)}{\psi_n(mx)\xi_n'(x) - m\xi_n(x)\psi_n'(mx)}, \quad (2.61)$$

and we now have a closed form for the scattered fields.

### 2.4.3 Scattering from a coated sphere

The application of the separation of variables for a homogenous sphere can be directly extended to an n-level sphere. Here we briefly outline the calculation of the scattered fields for a 2-level or coated sphere. We consider the geometry shown in figure 2.5 with a spherical scattering center with an outer radius  $b$ . The particle has a core, with radius  $a < b$ , that is made up of different

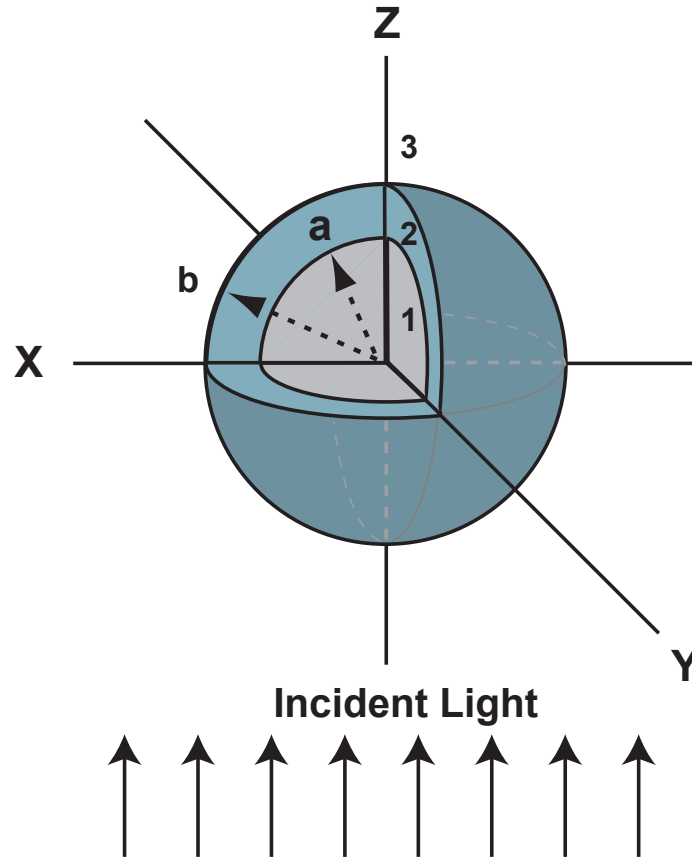


**Figure 2.5.** Geometry for the problem of light scattering by a coated spherical particle. A spherical particle is centered at the origin, and surrounded by an infinite homogenous dielectric medium. The particle has two levels: an inner core of radius  $a$ , and an outer shell of radius  $b$ . Both the core and coating are made up of homogenous (yet mutually exclusive) dielectric material. The particle is illuminated by an infinite plane wave traveling along the  $z$  axis. We define region 1 to be inside the particle core, region 2 to be the coating, and region 3 to be the surrounding medium.

material than the coating. We now must consider 3 regions: region 1 is the particle core, region 2 is the coating, and region 3 is the surrounding medium. Our expansions for the incident and scattered fields, as well as for the fields in region 1, are exactly as written in equations (2.48-2.53). We now have to expand the fields in region 2, which adds some complexity to the problem. In this region, both spherical Bessel functions and the spherical Neumann functions are finite, and thus the electric field must be expanded in both as

$$\mathbf{E}_2 = \sum_{n=1}^{\infty} E_n \left( f_n \mathbf{M}_{oln}^{(1)} - i g_n \mathbf{N}_{eln}^{(1)} + v_n \mathbf{M}_{oln}^{(2)} - i w_n \mathbf{N}_{oln}^{(2)} \right). \quad (2.62)$$

Now we apply the boundary conditions at the two interfaces, namely

$$(\mathbf{E}_2 - \mathbf{E}_1) \times \hat{\mathbf{r}} = \mathbf{0} \Big|_{r=a}, \quad (2.63)$$

$$(\mathbf{E}_s + \mathbf{E}_i - \mathbf{E}_2) \times \hat{\mathbf{r}} = \mathbf{0} \Big|_{r=b}, \quad (2.64)$$

with corresponding conditions on the magnetic fields. These conditions yield 8 equations in 8 unknowns, which can be solved for the expansion coefficients. Here we define two size parameters,  $x = k_3 a$  and  $y = k_3 b$ , and we define  $m_1 = k_2/k_1$  and  $m_2 = k_3/k_2$  as the relative refractive indices at the core-coating and coating-medium interfaces, respectively. If we define the function  $\chi_n(\nu) = \nu z_n^{(2)}(\nu)$  and assume that  $\mu_1 = \mu_2 = \mu_3$ , we can solve for the scattered field expansion coefficients as

$$a_n = \frac{\psi_n(y)[\psi'_n(m_2 y) - A_n \chi'_n(m_2 y)] - m_2 \psi'_n(y)[\psi_n(m_2 y) - A_n \chi_n(m_2 y)]}{\xi_n(y)[\psi'_n(m_2 y) - A_n \chi'_n(m_2 y)] - m_2 \xi'_n(y)[\psi_n(m_2 y) - A_n \chi_n(m_2 y)]}, \quad (2.65)$$

$$b_n = \frac{m_2 \psi_n(y) [\psi'_n(m_2 y) - B_n \chi'_n(m_2 y)] - \psi'_n(y) [\psi_n(m_2 y) - B_n \chi_n(m_2 y)]}{m_2 \xi_n(y) [\psi'_n(m_2 y) - B_n \chi'_n(m_2 y)] - \xi'_n(y) [\psi_n(m_2 y) - B_n \chi_n(m_2 y)]}, \quad (2.66)$$

where

$$A_n = \frac{m_2 \psi_n(m_2 x) \psi'_n(m_1 x) - m_1 \psi'_n(m_2 x) \psi_n(m_1 x)}{m_2 \chi_n(m_2 x) \psi'_n(m_1 x) - m_1 \chi'_n(m_2 x) \psi_n(m_1 x)}, \quad (2.67)$$

$$B_n = \frac{m_2 \psi_n(m_1 x) \psi'_n(m_2 x) - m_1 \psi_n(m_2 x) \psi'_n(m_1 x)}{m_2 \chi'_n(m_2 x) \psi_n(m_1 x) - m_1 \psi'_n(m_1 x) \chi'_n(m_2 x)}. \quad (2.68)$$

This same procedure could be followed to calculate the scattered field for an n-level sphere, and the complexity would increase as 4 additional expansion coefficients per layer.

#### **2.4.4 T matrix and extended boundary condition**

The separation of variables method can be applied to particles with symmetry corresponding to a specific coordinate system. It is particularly well-suited to spherical particles, and analogous problems have been solved for infinite cylinders in polar coordinates [1] and for ellipsoids in elliptical coordinates [4]. To solve for the scattered electric field from arbitrarily shaped particles, a common approach is the T matrix method. Presented here is a very rough sketch as to how this method is implemented.

The heart of the T matrix method relies on the fact that we can expand *any* incident,  $\mathbf{E}_i$ , scattered,  $\mathbf{E}_s$ , and internal,  $\mathbf{E}_1$ , electric fields in vector spherical harmonics as

$$\mathbf{E}_i = \sum_{n=1}^{\infty} \sum_{m=-n}^n \left( p_{nm} \mathbf{M}_{nm}^{(1)} + q_{nm} \mathbf{N}_{nm}^{(1)} \right), \quad (2.69)$$

$$\mathbf{E}_s = \sum_{n=1}^{\infty} \sum_{m=-n}^n \left( a_{nm} \mathbf{M}_{nm}^{(3)} + b_{nm} \mathbf{N}_{nm}^{(3)} \right), \quad (2.70)$$

$$\mathbf{E}_1 = \sum_{n=1}^{\infty} \sum_{m=-n}^n \left( c_{nm} \mathbf{M}_{nm}^{(3)} + d_{nm} \mathbf{N}_{nm}^{(3)} \right). \quad (2.71)$$

Because of the linearity of Maxwell's equations and the boundary conditions, there exists a transition matrix (or T matrix),  $\vec{\mathbf{T}}$ , between the expansion coefficients for the incident and scattered field as

$$a_{mn} = \sum_{n'=1}^{\infty} \sum_{m'=-n'}^{n'} \left( T_{mnm'n'}^{11} p_{m'n'} + T_{mnm'n'}^{12} q_{m'n'} \right), \quad (2.72)$$

$$b_{mn} = \sum_{n'=1}^{\infty} \sum_{m'=-n'}^{n'} \left( T_{mnm'n'}^{21} p_{m'n'} + T_{mnm'n'}^{22} q_{m'n'} \right). \quad (2.73)$$

If one could calculate these  $T^{ij}$ , then the problem would be solved. A major advantage of the T matrix formalism is that once a T matrix is computed with respect to one particle orientation, the T matrix can be rotated to reflect scattering from a particle in any orientation, meaning that it only need be calculated once. In fact, it can be orientation-averaged *analytically* once a T matrix has been calculated for a particle in a fixed position.

The elements of the T matrix are computed using the Extended Boundary Condition Method (EBCM). This strategy is based on re-casting the scattering problem into a surface integral equation, as was first introduced by Waterman [5].

The vector Green's identity states that for any vectors  $\mathbf{a}$  and  $\mathbf{b}$  and a surface  $S$  bounding a volume  $V$ ,

$$\int_V dV [\mathbf{a} \cdot (\nabla \times \nabla \times \mathbf{b}) - \mathbf{b} \cdot (\nabla \times \nabla \times \mathbf{a})] = \int_S dS \cdot \hat{\mathbf{n}} [\mathbf{b} \times (\nabla \times \mathbf{a}) - \mathbf{a} \times (\nabla \times \mathbf{b})], \quad (2.74)$$

where  $\hat{\mathbf{n}}$  is normal to the surface. We then substitute  $\mathbf{a} = \mathbf{E}$  and  $\mathbf{b} = \vec{\mathbf{G}} \cdot \mathbf{c}$ , where  $\vec{\mathbf{G}}$  is the Green's function that satisfies  $\nabla \times \nabla \times \vec{\mathbf{G}} - k^2 \vec{\mathbf{G}} = \vec{\mathbf{I}} \delta(\mathbf{r} - \mathbf{r}')$  and  $\mathbf{c}$  is an arbitrary constant vector. If the volume that we are integrating over,  $V$ , is the *medium surrounding the particle*, then the bounding surface,  $S$ , has two components: the surface of the particle,  $S_i$ , and the surface of a sphere centered at the origin and with a radius of  $r = \infty$ ,  $S_\infty$  (please see figure 2.6). By design, the volume integral simplifies to

$$\int_{\substack{\text{outside} \\ \text{medium}}} dV \mathbf{E} \cdot (\nabla \times \nabla \times \vec{\mathbf{G}} - k^2 \vec{\mathbf{G}}) \cdot \mathbf{c} = \begin{cases} \mathbf{E}(\mathbf{r}) \cdot \mathbf{c} & \text{for } \mathbf{r} \in V \\ 0 & \text{for } \mathbf{r} \notin V \end{cases}. \quad (2.75)$$

Outside of the particle we know from equation (2.3) that  $\mathbf{E} = \mathbf{E}_i + \mathbf{E}_s$ . If we look at the surface integral over  $S_\infty$ , this expression simplifies to

$$\int_{S_\infty} dS [-i\omega\mu(\hat{\mathbf{r}} \cdot \mathbf{H})] \times \vec{\mathbf{G}} \cdot \mathbf{c} - (\hat{\mathbf{r}} \cdot \mathbf{E}) \times (\nabla \times \vec{\mathbf{G}} \cdot \mathbf{c}), \quad (2.76)$$

and in the far field  $\mathbf{E}_s \cdot \hat{\mathbf{r}} = \mathbf{H}_s \cdot \hat{\mathbf{r}} = 0$ . Thus the integral over  $S_\infty$  is independent of the scattering particle and must give us the incident electric field dotted into our constant vector,  $\mathbf{E}_i \cdot \mathbf{c}$ , while the integral over the surface of the particle must give us the analogous scalar product for our scattered field,  $\mathbf{E}_s \cdot \mathbf{c}$ . So combining equations (2.75-2.76), and canceling  $\mathbf{c}$  from both sides of the equation, we get

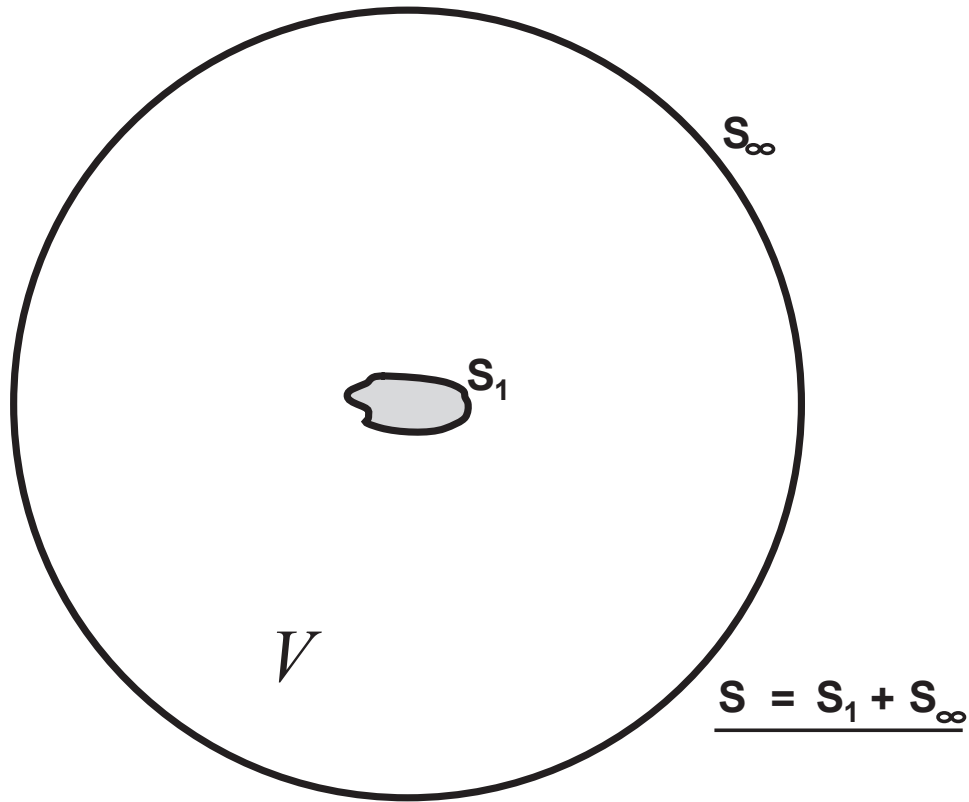


**Figure 2.6.** Geometry used for extended boundary condition T matrix calculations. If our integral from equation (2.74) is over the volume outside of the particle, the bounding surface for the volume,  $V$ , contains two components: the surface of the sphere at infinity,  $S_\infty$ , and the surface of the particle,  $S_1$ .

$$\int_{S_p} dS \left[ i\omega\mu(\hat{\mathbf{n}} \times \mathbf{H}) \cdot \tilde{\mathbf{G}} + (\hat{\mathbf{n}} \times \mathbf{E}) \cdot (\nabla \times \tilde{\mathbf{G}}) \right] = \begin{cases} \mathbf{E}_s(\mathbf{r}) & r \in V \\ -\mathbf{E}_i(\mathbf{r}) & r \notin V \end{cases}, \quad (2.77)$$

which is known as the extended boundary condition, as this is an analytic continuation of the incident and scattered fields into the particle in such a way that they exactly cancel each other out. From here, we have to use both forms of equation (2.77) to solve for the scattered field. First, we use the known form of the incident field, equation (2.69), and insert it into the lower branch of equation (2.77) to find the surface fields in terms of the incident fields. Then we can take this expression and substitute it back into the upper branch of equation (2.77) to obtain the scattered field.

The Green's function,  $\tilde{\mathbf{G}}(\mathbf{r}, \mathbf{r}')$ , can be expanded in vector spherical harmonics as

$$\tilde{\mathbf{G}}(\mathbf{r}, \mathbf{r}') = ik \sum_{n=0}^{\infty} \sum_{m=-n}^n (-1)^m \begin{cases} \mathbf{M}_{n,-m}^{(3)}(\mathbf{r}') \mathbf{M}_{n,m}^{(1)}(\mathbf{r}) + \mathbf{N}_{n,-m}^{(3)}(\mathbf{r}') \mathbf{N}_{n,m}^{(1)}(\mathbf{r}) & r < r' \\ \mathbf{M}_{n,-m}^{(1)}(\mathbf{r}') \mathbf{M}_{n,m}^{(3)}(\mathbf{r}) + \mathbf{N}_{n,-m}^{(1)}(\mathbf{r}') \mathbf{N}_{n,m}^{(3)}(\mathbf{r}) & r > r' \end{cases}. \quad (2.78)$$

From here, substituting equations (2.69-2.71) and (2.77-2.78) subject to the boundary conditions in equations (2.12-2.13) we can obtain a linear equation that links the expansion coefficients of the scattered field to those of the internal field, which is written in compact form

$$\begin{bmatrix} p_{mn} \\ q_{mn} \end{bmatrix} = {}_1\tilde{\mathbf{Q}} \begin{bmatrix} c_{mn} \\ d_{mn} \end{bmatrix}, \quad (2.79)$$

where the elements of  ${}_1\tilde{\mathbf{Q}}$  involve surface integrals over the particle as

$${}_1Q_{mmm'n'}^{11} = (-1)^m (-i) \int_{S_p} dS \hat{\mathbf{n}} \left[ k_1 k_2 \mathbf{N}_{m'n'}^{(1)}(k_1 r) \times \mathbf{M}_{-mn}^{(3)}(k_2 r) - k_2^2 \mathbf{M}_{m'n'}^{(1)}(k_1 r) \times \mathbf{N}_{-mn}^{(3)}(k_2 r) \right], \quad (2.80)$$

$${}_1Q_{mmm'n'}^{12} = (-1)^m (-i) \int_{S_p} dS \hat{\mathbf{n}} \left[ k_1 k_2 \mathbf{M}_{m'n'}^{(1)}(k_1 r) \times \mathbf{M}_{-mn}^{(3)}(k_2 r) - k_2^2 \mathbf{N}_{m'n'}^{(1)}(k_1 r) \times \mathbf{N}_{-mn}^{(3)}(k_2 r) \right], \quad (2.81)$$

$${}_1Q_{mmm'n'}^{21} = (-1)^m (-i) \int_{S_p} dS \hat{\mathbf{n}} \left[ k_1 k_2 \mathbf{N}_{m'n'}^{(1)}(k_1 r) \times \mathbf{N}_{-mn}^{(3)}(k_2 r) - k_2^2 \mathbf{M}_{m'n'}^{(1)}(k_1 r) \times \mathbf{M}_{-mn}^{(3)}(k_2 r) \right], \quad (2.82)$$

$${}_1Q_{mmm'n'}^{22} = (-1)^m (-i) \int_{S_p} dS \hat{\mathbf{n}} \left[ k_1 k_2 \mathbf{M}_{m'n'}^{(1)}(k_1 r) \times \mathbf{N}_{-mn}^{(3)}(k_2 r) - k_2^2 \mathbf{N}_{m'n'}^{(1)}(k_1 r) \times \mathbf{M}_{-mn}^{(3)}(k_2 r) \right]. \quad (2.83)$$

Similarly, we can write a linear relationship between the expansion coefficients for the internal and scattered field as

$$\begin{bmatrix} a_{mn} \\ b_{mn} \end{bmatrix} = {}_2\tilde{\mathbf{Q}} \begin{bmatrix} c_{mn} \\ d_{mn} \end{bmatrix}, \quad (2.84)$$

where the elements are also integrations over the surface of the particle as

$${}_2Q_{mmm'n'}^{11} = (-1)^{m+1} (-i) \int_{S_p} dS \hat{\mathbf{n}} \left[ k_1 k_2 \mathbf{N}_{m'n'}^{(1)}(k_1 r) \times \mathbf{M}_{-mn}^{(1)}(k_2 r) - k_2^2 \mathbf{M}_{m'n'}^{(1)}(k_1 r) \times \mathbf{N}_{-mn}^{(1)}(k_2 r) \right], \quad (2.85)$$

$${}_2Q_{mmm'n'}^{12} = (-1)^{m+1} (-i) \int_{S_p} dS \hat{\mathbf{n}} \left[ k_1 k_2 \mathbf{M}_{m'n'}^{(1)}(k_1 r) \times \mathbf{M}_{-mn}^{(1)}(k_2 r) - k_2^2 \mathbf{N}_{m'n'}^{(1)}(k_1 r) \times \mathbf{N}_{-mn}^{(1)}(k_2 r) \right], \quad (2.86)$$

$${}_2Q_{mmm'n'}^{21} = (-1)^{m+1} (-i) \int_{S_p} dS \hat{\mathbf{n}} \left[ k_1 k_2 \mathbf{N}_{m'n'}^{(1)}(k_1 r) \times \mathbf{N}_{-mn}^{(1)}(k_2 r) - k_2^2 \mathbf{M}_{m'n'}^{(1)}(k_1 r) \times \mathbf{M}_{-mn}^{(1)}(k_2 r) \right], \quad (2.87)$$

$${}_2Q_{mmm'n'}^{22} = (-1)^{m+1} (-i) \int_{S_p} dS \hat{\mathbf{n}} \left[ k_1 k_2 \mathbf{M}_{m'n'}^{(1)}(k_1 r) \times \mathbf{N}_{-mn}^{(1)}(k_2 r) - k_2^2 \mathbf{N}_{m'n'}^{(1)}(k_1 r) \times \mathbf{M}_{-mn}^{(1)}(k_2 r) \right]. \quad (2.88)$$

Given these two matrices, we can finally write our T matrix as

$$\tilde{\mathbf{T}} = {}_2\tilde{\mathbf{Q}} \cdot ({}_1\tilde{\mathbf{Q}})^{-1}. \quad (2.89)$$

If the incident field is a plane wave, then we can write the scattered field expansion coefficients in terms of the incident field expansion coefficients as

$$\begin{bmatrix} a_n \\ b_n \end{bmatrix} = \vec{\mathbf{T}} \begin{bmatrix} p_n = i^n \frac{2n+1}{n(n+1)} \\ q_n = -i^{n+1} \frac{2n+1}{n(n+1)} \end{bmatrix}. \quad (2.90)$$

The T matrix method has been recently revisited by Meshchenko [2, 6, 7], and that author has made a FORTRAN implementation freely available [7]. The forward calculations presented in subsequent sections are done using the double-precision FORTRAN code from that reference.

## 2.5 Matrix elements and cross sections

Now that we have the tools to calculate the expansion coefficients of the scattered fields, we can write our observable quantities in terms of these expansion coefficients. If we first define the angular functions,

$$\pi_n = \frac{P_n^1(\theta)}{\sin(\theta)}, \quad (2.91)$$

$$\tau_n = \frac{dP_n^1(\theta)}{d\theta}, \quad (2.92)$$

we can write the diagonal scattering matrix elements as

$$S_1 = \sum_n \frac{2n+1}{n(n+1)} (a_n \pi_n + b_n \tau_n), \quad (2.93)$$

$$S_2 = \sum_n \frac{2n+1}{n(n+1)} (a_n \tau_n + b_n \pi_n). \quad (2.94)$$

For particles with spherical symmetry, the off-diagonal scattering matrix elements vanish. For particles without spherical symmetry, it is easiest to write the off-

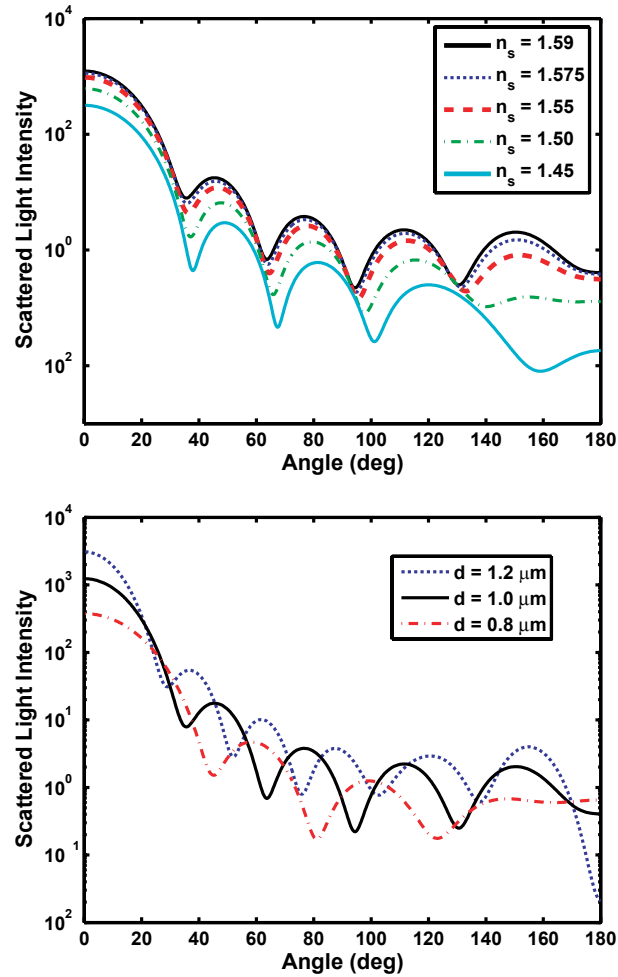


**Figure 2.7.** Plots of Mie theory calculations demonstrating the effects on particle size and refractive index on light scattering. In all calculations, we assume that we are illuminating with 633 nm light, and that the particles are in water ( $n = 1.33$ ). In the top panel we show angular scattering distributions from 1  $\mu\text{m}$  spheres with refractive indices ranging from 1.59 (polystyrene) to 1.45 (organelle). Refractive index has a weak effect on the shape of the curve, but has a strong effect on  $\sigma_{\text{sca}}$ . In the lower panel, we show angular scattering distributions from spheres with refractive indices of 1.59, and diameters ranging from 0.8-1.2  $\mu\text{m}$ . These curves show that particle size has a large effect on both the shape ( $d\sigma_{\text{sca}}/d\Omega$ ) of angular scattering and the total cross section,  $\sigma_{\text{sca}}$ .

diagonal elements in terms of the T-matrix elements. Assuming averaging over all orientations, we get

$$S_3 = S_4 = \sum_n \left[ \frac{2n(n+1)}{n(n+1)} T_n^{11} \tau_n(\theta) \pi_n(0) + T_n^{12} \tau_n(\theta) \tau_n(0) + T_n^{21} \pi_n(\theta) \pi_n(0) + T_n^{11} \pi_n(\theta) \tau_n(0) \right]. \quad (2.95)$$

We can also write the extinction and scattering cross sections in terms of the expansion coefficients as

$$\sigma_{ext} = \frac{2\pi}{k^2} \sum_{n=1}^{\infty} [(2n+1) \text{Re}(a_n + b_n)], \quad (2.96)$$

$$\sigma_{sca} = \frac{2\pi}{k^2} \sum_{n=1}^{\infty} [(2n+1) (|a_n|^2 + |b_n|^2)]. \quad (2.97)$$

## 2.6 Effects of particle size, shape, refractive index, and ensemble averaging on $\sigma_{sca}$ and $d\sigma_{sca}/d\Omega$

Using the above methods for calculating the differential and total cross sections, we can examine the effects of particle size, shape, and refractive index on these quantities. We first examine the effects of index of refraction on the scattering properties of a single sphere. In the top panel of figure 2.7, we use Mie theory to plot the angular scattering distributions for 1  $\mu\text{m}$  spheres in water ( $n = 1.33$ ) with refractive indices ranging from 1.59 to 1.45 that have been illuminated with 633 nm light. The shape of the curve is weakly dependant on the refractive index, while the overall scattered intensity,  $\sigma_{sca}$ , tracks well with refractive index. If instead of varying the refractive index, we vary the particle diameter, as shown

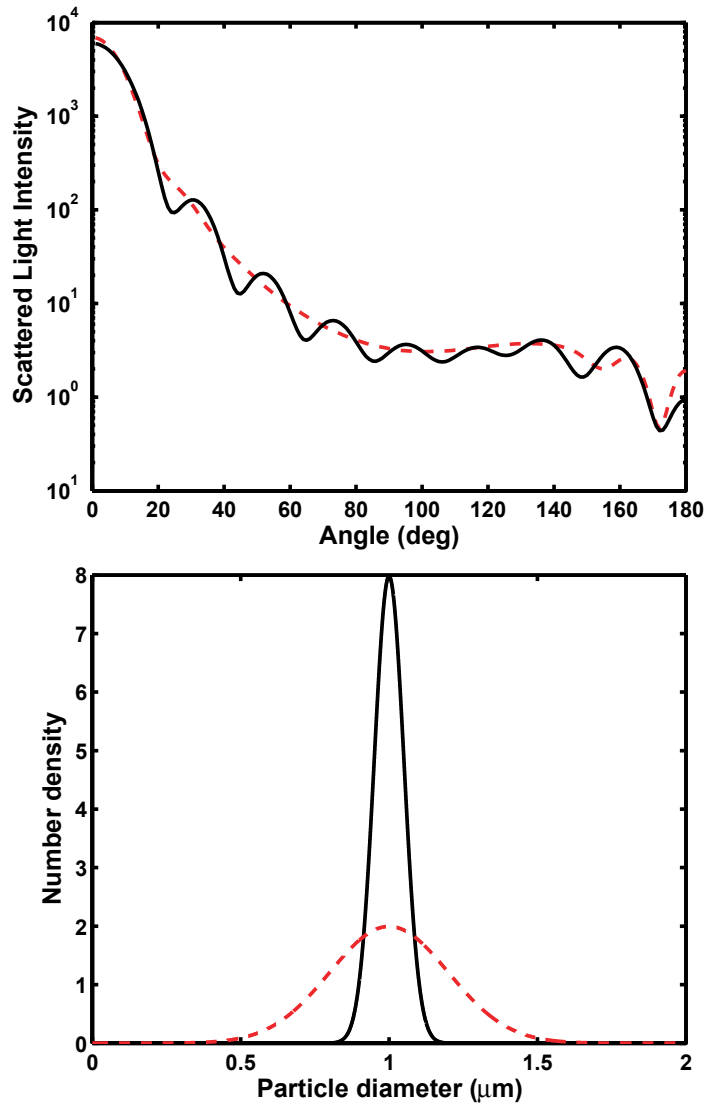


**Figure 2.8.** In the top panel we plot Mie theory calculations of angular scattering from narrow (solid black) and wide (dashed red) particle size distributions of light scattering centers both with a mean size of 1  $\mu\text{m}$ . The corresponding size distributions are plotted in the lower panel with identical line-style.

in the lower panel of figure 2.7, we see that the diameter has a strong effect on both the differential and total scattering cross sections.

Due to the strong dependence on particle size of the periodic or resonant structure in the differential cross section, this structure vanishes when scattering originates from populations of spheres whose sizes are distributed. In the top panel of figure 2.8, we see angular scattering distributions from two different populations of spheres, each with refractive indices of 1.59 and mean sizes of 1  $\mu\text{m}$ . The solid black curve represents angular scattering from a population of spheres with a standard deviation in particle diameter of 0.05  $\mu\text{m}$ , while the dashed red curve represents angular scattering from population of spheres with a standard deviation in particle diameter of 0.2  $\mu\text{m}$ . The corresponding particle size distributions are shown in the lower panel of figure 2.8.

We now demonstrate the effects of particle shape on scattering properties. It has been suggested that in the forward direction, orientation-averaged non-spherical particles scatter light roughly as surface-area-equivalent spheres [6]. To demonstrate this assertion, we calculated the scattered field for size distributions of spheres with mean diameters ranging from 0.4 – 2  $\mu\text{m}$  and with refractive indices of 1.59 in water illuminated with 633 nm light. We also calculated scattering from surface-area-equivalent populations of ellipsoids of revolution with shape parameters,

$$\varepsilon \equiv \frac{\text{Particle diameter parallel to axis of revolution}}{\text{Particle diameter perpendicular to axis of revolution}}, \quad (2.98)$$

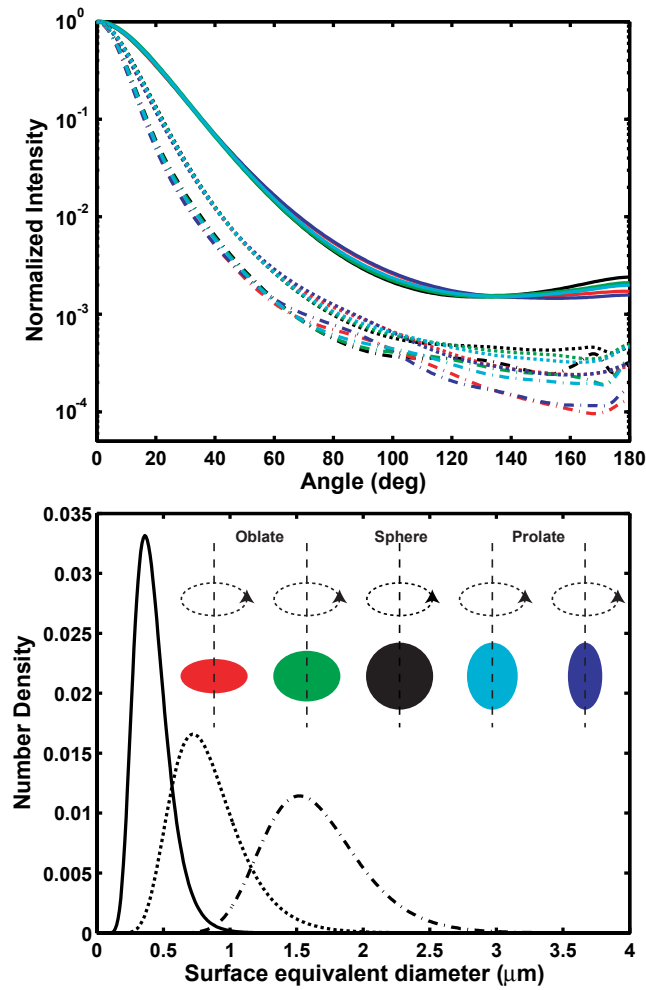


**Figure 2.9.** The top panel displays normalized angular scattering distributions calculated with the T matrix method for size distributions of spheres and surface-area-equivalent ellipsoids. The line color encodes particle shape, and the line style encodes surface-area-equivalent sphere particle size distributions that are both shown in the lower panel. These calculations demonstrate that in the forward direction, surface area, and not particle shape, affects angular scattering.

ranging from  $\varepsilon = 0.5 - 2$  and refractive indices of 1.59 using the T matrix formalism. In figure 2.9 we plot the angular scattering distributions for these spheres and ellipsoids that are normalized to 1 at  $\theta = 0$ . We encoded particle shape by color, with red and green curves representing  $\varepsilon = 0.5$  and  $\varepsilon = 0.75$  (oblate spheroids), respectively, and the light and dark blue representing  $\varepsilon = 1.5$  and  $\varepsilon = 2$  (prolate spheroids), respectively. The black curves are angular scattering distributions from spheres. We further encode surface-area-equivalent sphere particle size distributions in line style, with the corresponding size distributions shown in the lower panel. We see that in the *forward-scattering direction*, the shape of the differential cross sections depends strongly on the equal-surface-equivalent-sphere particle size distributions, while there is minimal if any dependence on particle shape.

We similarly looked at the effect of particle shape on the total scattering cross section,  $\sigma_{\text{sca}}$ . In figure 2.10, we show a bar plot of mean scattering cross section versus mean particle size for surface-area-equivalent size distributions of particles with refractive indices of 1.59 in water and illuminated with 633 nm light. The corresponding size distributions are plotted in the lower panel of this figure. We see that the total cross section tracks strongly with surface-equivalent sphere size and has a weak dependence on particle shape.

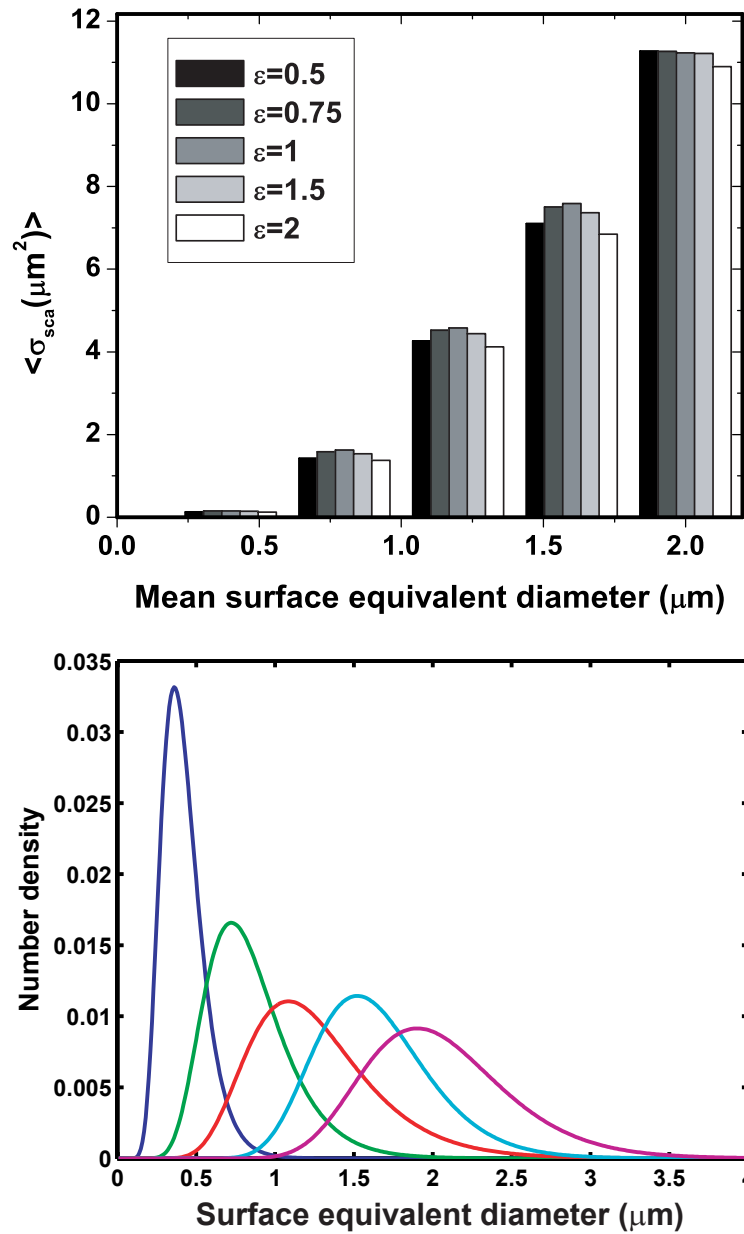


**Figure 2.10.** The top panel displays mean scattering cross sections for various size distributions of spheres and distributions of surface-area-equivalent ellipsoids. The surface-equivalent-distributions are displayed in the lower panel.

## 2.7 Discussion

We have reviewed light scattering from the formulation of the problem to the calculation of the scattered fields and cross sections for particles with spherical symmetry and for arbitrary homogenous particles. For spheres, we have shown that particle refractive index primarily affects the total scattering cross section, while particle size has a strong effect on both the shape of the differential and magnitude of the total scattering cross sections. Through forward calculations, we have demonstrated that in the forward direction, i.e.  $\theta < 90^\circ$ , surface area of the particle has the strongest effect on the shape of the differential cross section. Furthermore, particle shape has a minimal effect on the total cross section.

Modeling light scattering by an arbitrary particle with Mie theory is attractive for a variety of reasons. From a strictly computational point of view, Mie theory is both faster and more convergent than the T matrix method. The T matrix involves numeric integrations over the particle surface (equations (2.80-2.88)) and a matrix inversion (equation (2.89)). T matrix computations are generally not convergent for ellipsoids with aspect ratios greater than 2 [2]. Beyond the computational aspects, modeling light scattering from non-spherical particles is only as good as one's assumptions. If a researcher makes scattering measurements from a cloud of *unknown* aerosol particles, inversion of these measurements within a non-spherical model would be ambiguous.

For the remainder of this document, we will assume that scattering originates from particles with spherical symmetry. Based on our calculations using surface-area-equivalent ellipsoids, we confine our scattering measurements to sample forward-scattered light.

## References

1. C. F. Bohren and D. R. Huffman, *Absorption and scattering of light from small particles.*, (Wiley, New York, 1998).
2. M. I. Mishchenko, L. D. Travis, and A. A. Lacis, *Scattering, absorption, and emission of light by small particles*, (NASA Goddard Institute for Space Studies, New York, 2004).
3. F. M. Kahnert, "Numerical methods in electromagnetic scattering theory," *J. Quant. Spectrosc. Radiat. Transfer*, **79**, 775-824 (2003).
4. S. Asano and M. Sato, "Light-scattering by randomly oriented spheroidal particles," *Appl. Opt.* **19**, 962-974 (1980).
5. P. C. Waterman, "Matrix-methods in potential theory and electromagnetic scattering," *J. Appl. Phys.* **50**, 4550-4566 (1979).
6. M. I. Mishchenko, "Light scattering by size-shape distributions of randomly oriented axially symmetric particles of a size comparable to a wavelength," *Appl. Opt.* **32**, 4652-4666 (1993).
7. M. I. Mishchenko and L. D. Travis, "Capabilities and limitations of a current FORTRAN implementation of the T-matrix method for randomly oriented, rotationally symmetric scatterers," *J. Quant. Spectrosc. Radiat. Transfer*, **60**, 309-324 (1998).

## **Chapter 3. Mie theory interpretations of light scattering from intact cells**

### **3.1 Introduction**

There have been many recent studies showing the ability of light scattering measurements to monitor intracellular morphology. Previous authors have used wavelength resolved [1] and angularly resolved [2] backscattering measurements to obtain nuclear size distributions with applicability to cancer diagnosis. Other groups have looked at angularly resolved scattering from cells in suspension over a broad range of angles, for example 15-160 degrees [3] or 5-90 degrees [4] and concluded that organelles smaller than a nucleus are the dominant scatterers in these regimes. Angularly resolved light scattering for particle sizing has been widely used, although the difficulty of inverting angularly resolved light scattering measurements increases with the width of the particle size distribution [5,6]. Previous studies have shown that inverting angularly resolved light scattering from intact cells within a Mie theory model requires a broad distribution of scattering sizes, and that the mean scattering size is very small [3,4,7]. Here we present an analysis that includes the product of the particle

---

size distribution and the scattering cross section, which identifies a characteristic scattering size, and we examine the effect that this product has on the interpretation of the scattering data.

## 3.2 Construction of a goniometer

We constructed a goniometer to measure angularly resolved light scattering from particles or biological cells in suspension. A block diagram of the experimental setup is shown in figure 3.1. A scattering sample in aqueous suspension is placed in a cylindrical cuvette (Model 540.115, Helma, Plainview, NY), which is positioned above the center of a 30.5 cm diameter rotary stage (RT-12, Arrick Robotics, Tyler, TX). Red light (632.8 nm) from a 20 mW helium-neon laser is directed through the cuvette. In all of our measurements, the laser is linearly polarized perpendicular to the surface of the rotary stage. Light scattered from the sample is passed through a pinhole mounted midway to the edge of the rotary stage and collected by an optical fiber (200  $\mu\text{m}$  core diameter, 0.22 NA) that is mounted at the edge. Light exiting the fiber is measured by a photodiode (New Focus model 2001, San Jose, CA) and digitized at 16 bits. A PC-controlled stepper motor rotates the stage, and the angular position is read out from an optical encoder. The stage position and photodiode voltage are simultaneously recorded every  $2.5^\circ$ . The data acquisition is automated and controlled by a lab-built program written in LabView (National Instruments, Austin, TX). Each scan of the full angular range takes approximately 1 minute.

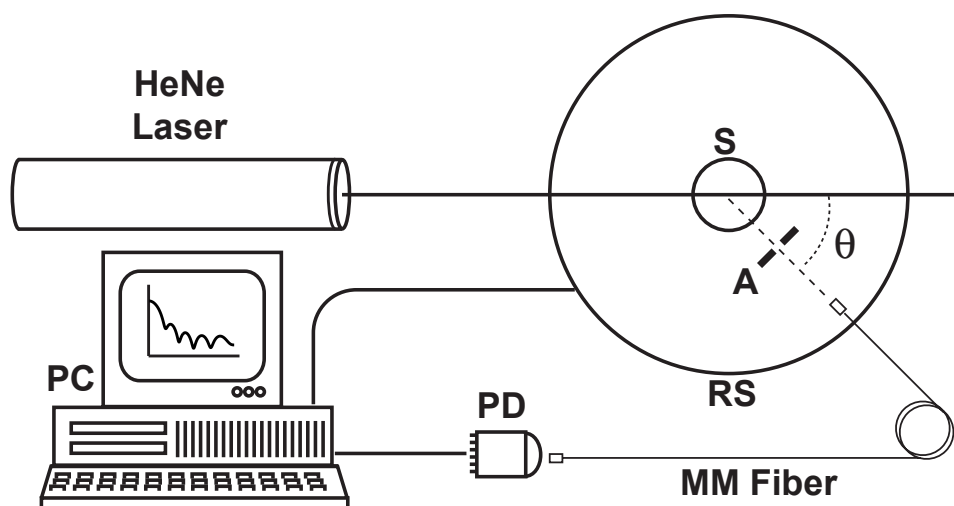


**Figure 3.1.** Block diagram of the goniometer setup for measuring angularly resolved light scattering. A laser beam is directed through a sample (S) suspended above the center of a computer (PC)-controlled rotary stage (RS). Scattered light is measured by a photodiode via a multimode fiber mounted on the stage.

For each measurement, a background is taken with the suspending solution in the absence of the scattering sample. The sample is then added and mixed well. Each data set represents the measurement of the sample with the background subtracted. There is also a multiplicative factor of  $\text{Sin}(\theta)$  to account for the number of particles being sampled at a given angle [5].

### **3.3 Cell culture and sample preparation**

EMT6 mouse mammary sarcoma cells were maintained in monolayer in Eagle's basal medium with 10% fetal bovine serum (complete media) at 37° C and 5% CO<sub>2</sub>. When the cells reached 60-70% confluence, the media was removed, and cells were washed twice with Hanks' Balanced Salt Solution (HBSS), lifted from the plate with 0.25% trypsin, and then suspended in at least 1 part complete media per part trypsin. They were then centrifuged and re-suspended in HBSS at a stock concentration of approximately  $5 \times 10^6$  cells/ml.

### **3.4 Scattering from polystyrene microspheres**

Aqueous suspensions of monodisperse polystyrene microspheres (Duke Scientific, Palo Alto, CA) were used to verify the goniometer experiment. These beads have a well defined spherical shape and index of refraction (1.59) and a narrow size distribution with a mean diameter of either 1 or 2  $\mu\text{m}$ , and a coefficient of variance (CV) of less than 8%. Scattering parameters from very

---

dilute suspensions of these microspheres can be calculated exactly with Mie theory. Thus, we wanted to create conditions in which we were measuring photons that had only undergone a single scattering event. To accomplish this in these experiments, the concentration of the 1  $\mu\text{m}$  diameter beads was adjusted to  $5 \times 10^6$  beads/ml, while that of the 2  $\mu\text{m}$  diameter beads was adjusted to  $10^6$  beads/ml, which yielded a scattering mean free path of 10 cm in both cases. The width of our cuvette is 2 cm, meaning that we were that we were sampling primarily singly-scattered light.

We fit a Mie theory model to our scattering data from these beads. The model assumed that scattering originated from an ensemble of spheres that obeyed a log-normal distribution in radius. Then we could write our particle size distribution as  $\rho(r) = c \ell(r)$ , where  $c$  is a constant and  $\ell(r)$  is a log-normal distribution as

$$\ell(r) = \frac{1}{rS\sqrt{2\pi}} \exp\left[-\frac{(\ln(r) - M)^2}{2S^2}\right], \quad (3.1)$$

where  $M$  and  $S$  are related to the mean,  $\mu$ , and standard deviation,  $SD$ , through the relationships

$$S^2 = \ln\left[1 + \left(\frac{SD}{\mu}\right)^2\right], \quad (3.2)$$

$$M = \ln(\mu) - \frac{S^2}{2}. \quad (3.3)$$

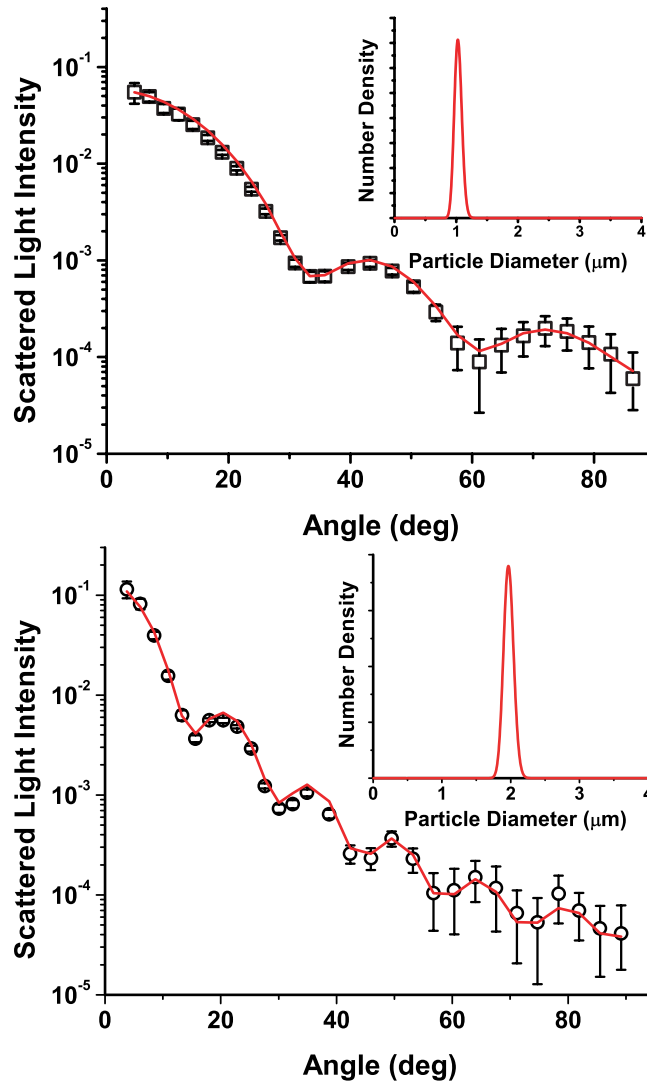


**Figure 3.2.** Angularly resolved light scattering data from 1 (top) and 2 (bottom)  $\mu\text{m}$  polystyrene microspheres. The solid lines are their corresponding Mie theory fits. The insets show the particle size distributions returned by the Mie theory fits described in the text.

Angular scattering distributions,  $S(\theta, r)$ , were calculated from Mie theory, and we created test functions,  $T(\theta)$ , such that

$$T(\theta) = \int S(\theta, r) \rho(r) dr. \quad (3.4)$$

We then adjusted  $\mu$ ,  $SD$ , and  $c$  using a downhill simplex algorithm [8] to minimize the function  $\chi^2$  as

$$\chi^2 = \sum_n \frac{(D_n - T_n)^2}{v_n}, \quad (3.5)$$

where  $D_n$  represents the  $n$ th data point,  $T_n$  is the corresponding value of the test function, and  $v_n$  is the corresponding variance.

Representative scattering data and Mie theory fits for 1 and 2  $\mu\text{m}$  polystyrene microspheres are shown in figure 3.2. Data sets for both the 1 and 2  $\mu\text{m}$  polystyrene microspheres are well represented by their Mie theory fits. For the 1  $\mu\text{m}$  spheres, the Mie theory fits predict that these spheres have a mean diameter of 1.01  $\mu\text{m}$  with a standard deviation of 0.05  $\mu\text{m}$ . In the case of the 2  $\mu\text{m}$  spheres, the model predicts that the beads have a mean diameter of 1.98  $\mu\text{m}$  with a standard deviation of 0.08  $\mu\text{m}$ . Both of these predictions are well within manufacturer specifications.

### 3.5 Scattering phase function from an ensemble of particles

The microsphere data and Mie theory fits shown above validate our goniometer experiment and demonstrate that through a Mie theory model we can very accurately size spherical scattering centers with narrow size distributions. Before moving on to scattering data from biological cells, we first need a framework from which to interpret light scattering measurements from an ensemble of scattering particles that does not necessarily have a narrow size distribution.

Angularly-resolved light scattering measurements from a single sphere samples the differential cross section,  $d\sigma/d\Omega$ , where  $\sigma$  is the total scattering cross section, and  $\Omega$  is a solid angle. Most goniometer experiments [3,4] do not measure an absolute intensity at the detector but rather a relative intensity as a function of scattering angle, so the data may be modeled as a normalized phase function  $P(\theta) = d\sigma/d\Omega \times \sigma^{-1}$ , where  $\theta$  is the polar scattering angle. If we consider scattering from a collection of  $N$  spheres, the appropriate weight for each individual phase function is the scattering cross section,  $\sigma$ , if we are considering all scattering angles. Then the phase function for the collection takes the form

$$P_{total}(\theta) = \frac{\sum_{j=1}^N \sigma_j P_j(\theta)}{\sum_{j=1}^N \sigma_j}. \quad (3.6)$$

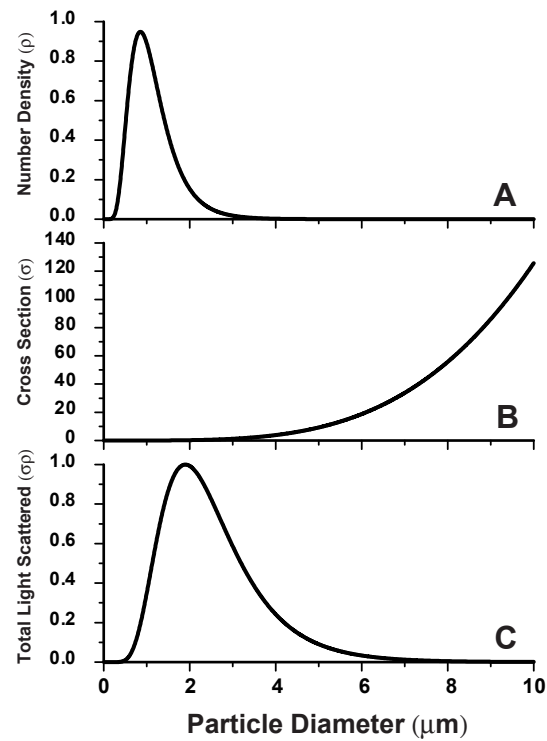


**Figure 3.3.** Relationship between the scattering cross-section-weighted size distribution,  $\sigma\rho(r)$  (C), and the particle size distribution,  $\rho(r)$  (A). The log normal particle size distribution shown here has a mean diameter and standard deviation of 1.09 and 0.6  $\mu\text{m}$ , respectively. The scattering cross section,  $\sigma(r)$  (B), as a function of particle diameter is plotted for spheres of refractive index 1.40 in a surrounding medium of index 1.38 and a vacuum wavelength of 633 nm.

If the number of particles of radius  $r$  per unit volume was described by a number density function,  $\rho(r)$ , then the phase function is written

$$P_{total}(\theta) = \frac{\int \sigma(r)\rho(r)P(r,\theta)dr}{\int \sigma(r)\rho(r)dr}. \quad (3.7)$$

The product  $\sigma\rho$  as a bulk optical property is simply the scattering coefficient,  $\mu_s$ , which is the inverse of the scattering mean free path. It is clear that this parameter is the appropriate weighting function for the scattering phase function and that it is to this parameter that goniometer experiments are in fact sensitive. For our purposes, we refer to this parameter as the total light scattered, as  $\mu_s$  is a macroscopic property and we are considering microscopic single-scattering events. Figure 3.3 shows the relationship between a specific particle size distribution,  $\rho(r)$ , and the total light scattered,  $\sigma\rho(r)$ , corresponding to that size distribution.

### 3.6 Interpretations of scattering from intact cells through $\sigma\rho$

To illustrate the physical nature of the quantity  $\sigma\rho$ , we examined its effect on the interpretation of fits to experimental scattering data. Angularly resolved scattering measurements were made from intact EMT6 cells prepared as described above. Background measurements were taken with HBSS, and cells from the stock suspension were added to a final concentration of  $10^5$  cells/ml. This

concentration corresponded to a 10 cm mean free path as measured in transmission by an absorption spectrophotometer. A Mie theory model incorporating a multimodal distribution of sphere sizes was fit to the data. Three forms of particle size distributions were used in the fits: log normal; exponential; and Gaussian. All fits were carried out by building test functions from Mie theory as written in equation (3.4). Here we assumed that the particle size distributions were made up of sums of log normal distributions,

$$\rho(r) = \sum_j c_j \ell_j(r), \quad (3.8)$$

of Gaussian distributions,

$$\rho(r) = \sum_j c_j \exp\left[\frac{-(r - \mu_j)^2}{2SD^2}\right] \frac{1}{SD_j \sqrt{2\pi}}, \quad (3.9)$$

or of exponential distributions

$$\rho(r) = \sum_j c_j \mu_j^{-1} \exp(-r / \mu_j), \quad (3.10)$$

and minimizing  $\chi^2$  (equation (3.5)) using a downhill simplex method. For each distribution type, we attempted to fit the data using single particle size distribution, a bimodal distribution, and a trimodal distribution. In all cases, a bimodal distribution best described the data. The bimodal distribution showed a great improvement in  $\chi^2$  over the single distribution. Furthermore, when we attempted to fit trimodal distributions to our data, our fitting algorithm returned a bimodal distribution, with the amplitude of the third distribution tending toward

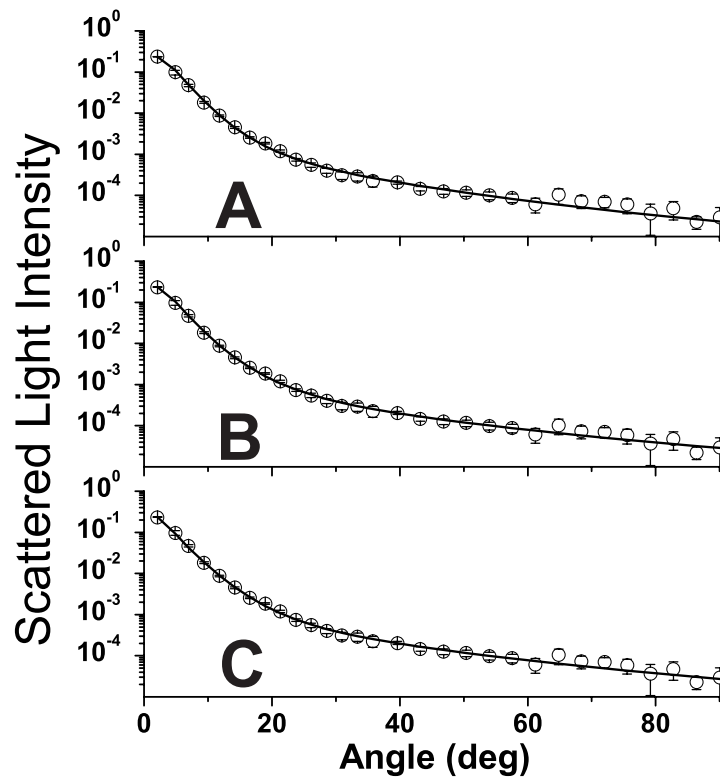


**Figure 3.4.** Angularly resolved light scattering data (o) from intact EMT6 cells with bi-modal fits (—) assuming Gaussian (A), exponential (B), and log normal (C) distributions. Data were obtained at 31 angular positions from 5 to 90°. The global minimum in  $\chi^2$  was obtained with the log normal fit. Mean scatterer diameters, standard deviations, and relative numbers of scatterer populations are summarized in Table 3.1 for the three assumed particle size distributions.

---

zero (i.e.  $c_3 = 0$ ). For the bimodal log normal and Gaussian distributions, the fitting parameters were the means and widths of the two distributions and the relative number of particles in each distribution, resulting in 6 fit parameters. In the case of the exponential distribution, the width of the distribution is fixed for a given mean, leaving only 4 independent fit parameters for a bimodal distribution. To confirm the validity of the bimodal size distribution, a series of fits was also performed assuming two and three log normal distributions not for  $\rho(r)$  but instead for the quantity  $\sigma\rho$ , thereby abandoning any assumption of a particle size distribution altogether.

The data are well represented by fits of all three distributions, as can be seen in figure 3.4. The log normal distribution provided the best fit, with the exponential distribution degrading  $\chi^2$  by 11%. Fits incorporating the Gaussian distribution were more interesting. The Gaussian distribution is symmetric, while the log normal and exponential distributions are skewed. When the means and widths of the Gaussian distributions were free parameters, the minimum in  $\chi^2$ , which was 38% higher than that of the log normal distribution, was achieved by Gaussians with negative means, with only the positive tail of the distribution being sampled by the fitting routine. The resulting size distribution qualitatively resembled an exponential distribution, with a mean slightly higher than that returned by the exponential fit (please see figure 3.5). When the means of the Gaussian distributions were constrained to be positive, the data could not be well

---



---

<b>Parameter</b>	<b>Log Normal</b>	<b>Exponential</b>	<b>Gaussian</b>
Mean <sub>1</sub>	1.09	0.59	0.7
SD <sub>1</sub>	0.6	0.59	0.65
Mean <sub>2</sub>	0.14	0.06	0.08
SD <sub>2</sub>	0.07	0.06	0.07
c <sub>2</sub> /c <sub>1</sub>	330	704	100000
$\chi^2/\nu$	0.975	1.1	1.25

---

**Table 3.1.** Parameters returned from Mie theory fits to angularly resolved scattering data using three functional forms of particle size distributions. The parameter  $c_2/c_1$  is the ratio of particle numbers in distributions two and one, respectively. The Gaussian parameters reflect the positive sampled tails of the distributions with negative means, as described in the text and shown pictorially in figure 3.5. Dimensions of means and standard deviations (SD) are microns ( $\mu\text{m}$ ).

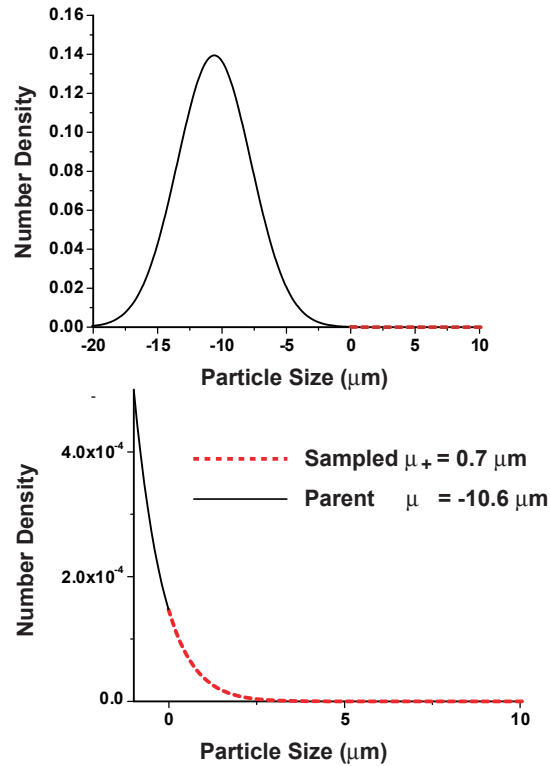


**Figure 3.5.** Example of one size distribution returned by fits to cell data assuming Gaussian particle size distributions. Our fitting algorithm only sampled physical (positive) sized particles. When the mean and standard deviations were allowed to float as free parameters, the best fit size distribution consisted of Gaussian curves with negative means. That meant that our phase functions were constructed using the positive tails (red dashed lines) of these parent curves (black solid lines), and the ‘effective’ particle size distribution qualitatively looked like an exponential distribution. The ‘effective’ means and standard deviations were calculated by numerical integrations over these positive tails.

---

fit, with a resulting reduced  $\chi^2$  ( $\chi^2/\nu$ , with  $\nu$  being degrees of freedom) of 5.79 (not shown). This suggests that a skewed distribution is required to represent the data, and the Gaussian distribution is not a good physical model for the particle size distribution of intracellular scatterers. We note also that the data were well fit by a bimodal distribution in  $\sigma\rho$ , but when a third population was introduced, it took the form of a Raleigh scatterer, and its relative amplitude tended to zero.

Parameters returned from the fits are summarized in Table 3.1. The means and widths of the particle sizes returned by the three distributions are not in agreement, although in each case they combine to produce very similar scattering phase functions. Despite the discrepancies in the means and standard deviations of the particle sizes extracted from the fits to the same scattering data using the three particle size distributions, figure 3.6 illustrates that the total light scattered as functions of particle diameter,  $\sigma\rho$ , are almost identical for these three different assumed functional forms. Not only is it striking that these plots look so similar given that all three arise from such different particle size estimates, but they all peak near 2  $\mu\text{m}$ , while none of the particle size distributions would lead one to believe that 2  $\mu\text{m}$  diameter particles were substantial light scatterers.

To consider the parameter  $\sigma\rho$  in the context of research that has been described previously on the subject of angularly resolved light scattering from cells, we have taken the Mie theory fits to angularly resolved scattering from AT3.1 cells reported by Mourant et al. [3] and plotted them in figure 3.7 as both

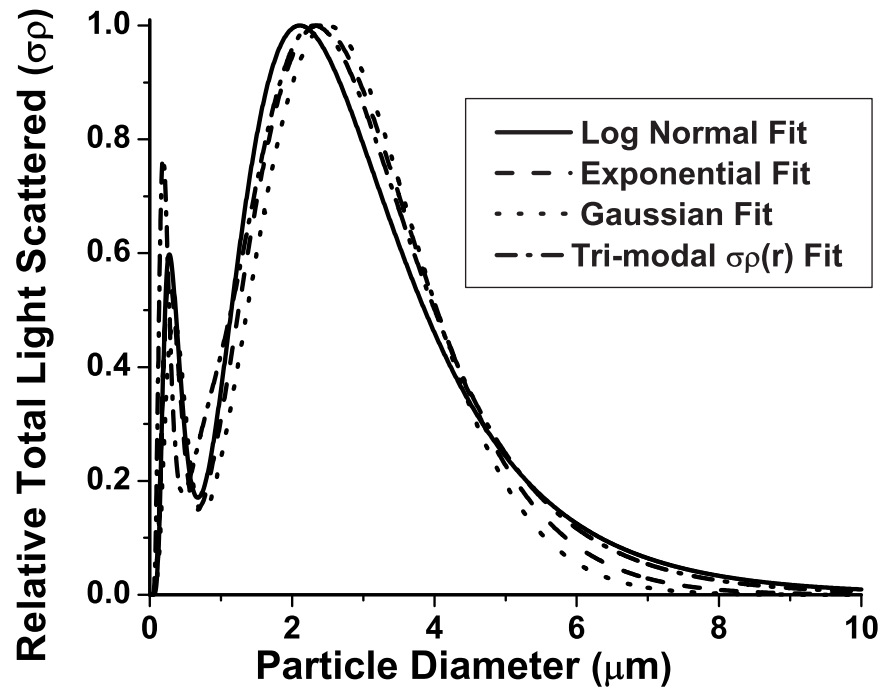


**Figure 3.6.** Relative total light scattered ( $\sigma\rho$ ) vs. particle diameter for the three distributions used to fit the data of figure 3.5 and a fourth curve resulting from a fit using a log normal functional form for  $\sigma\rho$  with a tri-modal distribution. The curves are normalized to 1 at their peak value.

---

particle size and total light scattered ( $\sigma\rho$ ) distributions. Note that the vertical axis of panel A in figure 3.7 is a log scale. This distribution would lead one to believe that the primary scatterers of light were on the order of 10 nm in diameter. Panel 4 B shows the effect of weighting the number density by the scattering cross section. In this plot, the dominant scatterers are shown to be approximately 2  $\mu\text{m}$  in diameter, in close agreement with our own studies.

The size parameters reported in Table 3.1 indicate that the ability to size intracellular organelles is highly dependent on the functional form that is assumed for the particle size distribution. Although the global minimum in  $\chi^2$  does suggest that the log normal distribution is the appropriate choice for extracting particle sizes in these experiments, the mean diameter extracted from fits to the same data varied by nearly a factor of two depending on the choice of the log normal vs. the exponential distribution while  $\chi^2$  changed by only 11%. Despite this sensitivity to the choice of the particle size distribution function, the shape of the product  $\sigma\rho$  vs. scatterer diameter plot is remarkably robust with respect to this choice. Thus it appears that Mie theory analysis of light scattering measurements reports the size distributions of the particles that scatter light into a given angular range even when its ability to actually size the scattering particles is dependent on an assumed functional form.

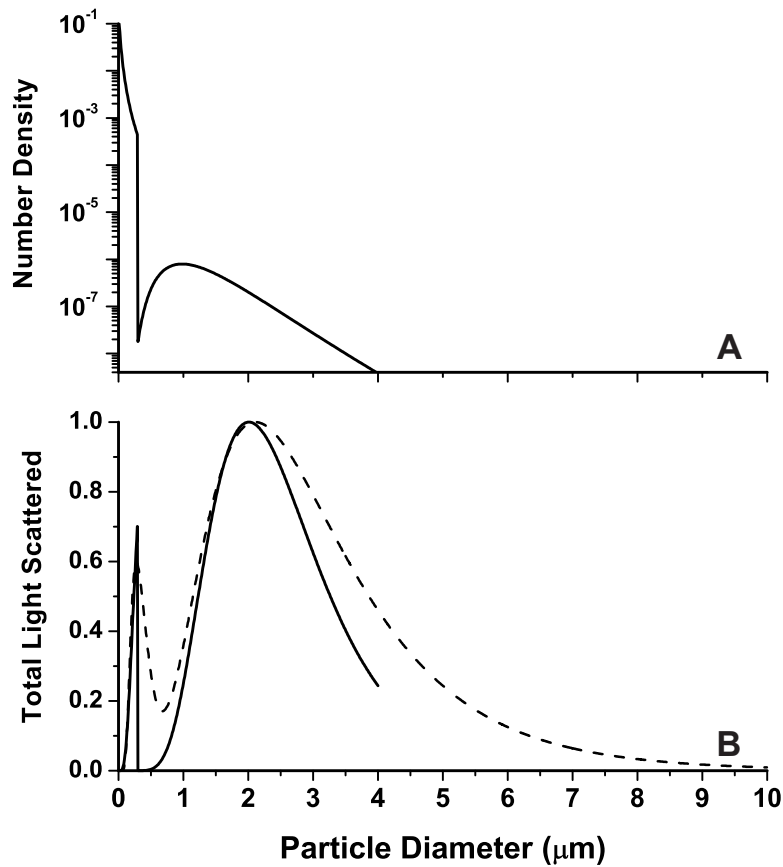


**Figure 3.7.** (A) Reproduction of figure 6 from Mourant et al. [3], which is a particle size distribution returned from a Mie theory fit to angularly resolved scattering data from AT3.1 cells. Note that this is plotted on a log scale, and the number of ‘large’ scatterers is much smaller than the number of ‘small’ scatterers. (B) The distribution shown in (A) weighted by the scattering cross section (—) plotted along with the total light scattered returned from the log normal fits to scattering from EMT6 cells (- -) depicted in figure 3.6.

### 3.7 Discussion

The main peak of the  $\sigma\rho$  curves in figures 3.6 and 3.7 provides evidence that angularly resolved light scattering is sensitive to organelles the size of lysosomes and mitochondria; the latter being 1-4  $\mu\text{m}$  in length [9]. Analysis of the  $\sigma\rho$  plots in figure 3.6 suggests that for EMT6 cells, 85% of the light was scattered from mitochondrial-sized organelles, and for AT3.1 cells that fraction is about 95%. The analysis of both cell lines indicates that there is a population of scattering centers that are in the 10 nm diameter scale, which are considerable in number but which do not have a very large effect on the shape of the scattering phase function.

In the next few chapters, we report our results from several research directions suggested by this study. In Chapters 4 and 6, we exploit known, mitochondria- and lysosome-targeted insults that alter  $\rho$  in an organelle-specific basis, in order to discern the separate contributions of different organelles such as mitochondria and lysosomes to the larger of the  $\sigma\rho$  distributions in figures 3.6 and 3.7. In Chapter 5, we report on the effects of adding strongly absorbing dyes to these organelle sites, and in effect altering  $\sigma$  in an organelle-specific manner, which will allow for extraction of refractive index from these organelle sites. The connection between the quantity  $\sigma\rho$ , which governs the shape of the single-scattering phase function, and the bulk tissue optical property  $\mu_s$  raises the

---

question as to whether these single scattering measurements could serve to inform macroscopic measurements of scattering from tissue.

---

## References

1. L. T. Perelman, V. Backman, M. Wallace, G. Zonios, R. Manoharan, A. Nusrat, S. Shields, M. Seiler, C. Lima, T. Hamano, I. Itzkan, J. Van Dam, J. M. Crawford, and M. S. Feld, "Observation of periodic fine structure in reflectance from biological tissue: A new technique for measuring nuclear size distribution," *Phys. Rev. Lett.* **80**, 627-630 (1998).
2. A. Wax, C. Yang, V. Backman, K. Badizadegan, C. W. Boone, R. R. Dasari, and M. S. Feld, "Cellular organization and substructure measured using angle-resolved low-coherence interferometry," *Biophys. J.* **82**, 2256-2264 (2002).
3. J. R. Mourant, T. M. Johnson, S. Carpenter, A. Guerra, T. Aida, and J. P. Freyer, "Polarized angular dependent spectroscopy of epithelial cells and epithelial cell nuclei to determine the size scale of scattering structures," *J. Biomed. Opt.* **7**, 378-387 (2002).
4. R. Drezek, A. Dunn, and R. Richards-Kortum, "Light scattering from cells: finite-difference time-domain simulations and goniometric measurements," *App. Opt.* **38**, 3651-3661 (1999).
5. C. F. Bohren and D. R. Huffman, *Absorption and scattering of light from small particles.*, (Wiley, New York, 1998).
6. G. C. Salzman, S. B. Singham, R. G. Johnston, and C. F. Bohren, "Light scattering and cytometry," *Flow Cytometry and Sorting*, M. R. Melamed, T. Lindmo, and M. L. Mendelshoh, eds., (Wiley-Liss, New York, 1990), 81-107.
7. J. R. Mourant, T. M. Johnson, V. Doddi, and J. P. Freyer, "Angular dependent light scattering from multicellular spheroids," *J. Biomed. Opt.* **7**, 93-99 (2002).
8. W. H. Press, B. P. Flannery, S. A. Teukolsky, and W. T. Vetterling, *Numerical Recipes in C: The Art of Scientific Computing*, (Cambridge University Press, New York, 1992).
9. G. E. Palade, "An electron microscope study of the mitochondrial structure," *J. Histochem. Cytochem.* **1**, 188-211 (1953).

## **Chapter 4. Light scattering from intact cells reports oxidative-stress-induced changes in mitochondrial morphology.**

### **4.1 Introduction**

For decades, changes in mitochondrial morphology such as swelling and condensation have been associated with a wide range of important biological functions and pathologies [1]. In addition, relatively recent work has established that mitochondrial volume dysregulation may result from the opening of the permeability transition pore in response to a variety of insults, including oxidants. The opening of channels or swelling sufficient to rupture the outer mitochondrial membrane may cause the release of cytochrome c, which in turns leads to necrotic or apoptotic cell death [2].

There has been significant renewed interest in the use of rigorous light scattering techniques to interrogate intracellular structure in cell systems and in tissue. With the exception of the extreme forward scattering direction where cell volume effects are important, Mourant et al. [3] showed that scattering of visible light from cells is governed predominantly by the size and composition of intracellular organelles rather than by the volume of the cell as a whole. A study

by Perelman et al. [4] demonstrated that oscillations in the wavelength-dependent backscattering from cells and from tissue could be interpreted on the basis of nuclear size distributions. Backman et al. [5] and Sokolov et al. [6] extended the backscattering measurement to include polarization, which enabled the discrimination between singly- and multiply-scattered light in thick samples such as tissue. These reports and a related investigation using angle-resolved low coherence interferometry [7] shared with Perelman et al. [4] an emphasis on the estimation of nuclear size in normal and malignant cell populations.

Mitochondria are also important scatterers of light in cells and tissue at visible wavelengths [8]. Optical property measurements of intact cells by Mourant et al. [3] revealed a distribution of intracellular scatterers with volumes equivalent to spheres with diameters in the range 0.2 - 1.0  $\mu\text{m}$ . Subsequent investigations by this group [9,10] supported the idea that the dominant populations of scatterers in cells are smaller than nuclei. The 1.0 – 2.0  $\mu\text{m}$  diameters at the high end of the range reported in their more recent papers are certainly compatible with mitochondria. Simple optical transmission measurements are sensitive to changes in mitochondrial morphology in preparations of isolated mitochondria, and such measurements have been used and reported for many years [11]. There are, however, very few reports of mitochondrial shape changes and swelling from optical measurements performed on intact cells. One such recent example is that of Boustany et al. [12], who used

---

an optical scatter imaging microscope to identify mitochondrial rounding in endothelial cell monolayers subjected to increased intracellular calcium.

In this chapter we describe the results of angle-resolved light scattering measurements performed on suspensions of intact murine mammary carcinoma cells, on these cells subjected to photodynamically-induced oxidative stress, and on suspensions of mitochondria isolated from rabbit liver. The particular photosensitization strategy that we chose induces oxidative stress directly within the mitochondria, and this stress is known to lead to the demise of the cell through rapid apoptosis and/or necrosis, depending on the specific cell line and the details of the treatment [13,14]. Our analysis reveals that the changes to the scattering induced by photodynamic stress are consistent with an inhomogeneous mitochondrial swelling in which cytosol pools in the center of the organelle, displacing mitochondrial material to the periphery. Transmission electron microscopy images of the control and treated cells confirm these particular changes in mitochondrial morphology.

## **4.2 Materials and methods**

### ***4.2.1 Cell culture and photodynamic treatment***

EMT6 mouse mammary carcinoma cells were maintained in a monolayer culture in Eagle's basal medium with 10% fetal bovine serum (complete media). Approximately  $10^7$  cells were lifted from monolayer with 0.25% trypsin and

suspended in at least 1 part complete media per part trypsin. They were then centrifuged and washed in serum free media. The cells were again centrifuged, suspended in serum free media, and incubated with 50  $\mu\text{M}$  aminolevulinic acid-hexylester (h-ALA) for 3 hours to allow for the accumulation of the mitochondrial-localizing photosensitizer protoporphyrin IX [15].

Following h-ALA incubation, the cells were again centrifuged and washed with serum free media and then centrifuged and washed in Hanks' balanced salt solution (HBSS). After a final centrifugation, the pellet was suspended in HBSS at a final volume of 2 ml. All handling of cells after incubation was done at very low light levels.

The cell suspension was then split into two groups. The control group was protected from any exposure to light. The treatment group was irradiated with 514 nm light at a fluence rate of 50  $\text{mW}/\text{cm}^2$  for 200s, conditions that were established by preliminary electron microscopy experiments. Greater than 90% of EMT6 cells subjected to this fluence stained with trypan blue immediately after treatment, indicating the onset of rapid necrosis [16]. Less than 1 hour elapsed between the time that the cells were taken out of incubation and the end of the light scattering experiments, and the time between irradiation and the end of the scattering measurements did not exceed 20 minutes.

---

### **4.2.2 Isolation of mitochondria**

Mitochondria were isolated from fresh rabbit liver following the method of Senior et al. [17]. Immediately after the animal was sacrificed, the liver was harvested and kept on ice in a 10% saline solution. It was then sliced and washed in a buffer of 0.3 M sucrose, 1 mM EDTA, and 1 mM Tris HCl (hereafter Tris buffer) at a pH of 7.4. The tissue was homogenized in Tris buffer with 1 mg/ml bovine serum albumin (BSA) in a potter, and the slurry was centrifuged at 900 g for 5 minutes. The supernate was kept and centrifuged at 11500 g for 5 minutes. The pellet was resuspended in buffer and BSA and centrifuged again. The fat layer was removed, and the pellet was suspended in Tris buffer and BSA.

The viability of the mitochondria was evaluated by measurements of oxygen consumption. A 3 ml covered cuvette was filled with 2 ml of a reaction buffer (24 mM glycylglycine, 10 mM MgCl<sub>2</sub>, 60 mM KH<sub>2</sub>PO<sub>4</sub>, and 87 mM sucrose) and 15 µl rotenone. The tip of an oxygen-sensitive electrode (Model OM-4, Microelectrodes, Inc, Bedford, NH) was placed through a small hole in the top of the cuvette. Sufficient mitochondria were added to the cuvette to establish easily-detectable oxygen consumption. Succinate (100 µl) was added to establish state 4 respiration, and then 20 µl ADP was added to establish state 3 respiration. After state 4 and state 3 respiration were verified with the oxygen electrode, the

---

mitochondria were considered viable. The mitochondria were kept on ice, and all subsequent handling was done in the Tris buffer.

### ***4.2.3 Angularly resolved light scattering***

Angularly resolved light scattering measurements were performed using the goniometer instrumentation described in Chapter 3. For experiments with cells, we measured scattering from suspensions of  $10^5$  cells/ml in HBSS. For experiments with isolated mitochondria, we measured scattering from dilute suspensions in Tris buffer.

### ***4.2.4 Electron microscopy methods***

For electron microscopy cells were grown on glass chamber slides and fixed in 0.1M phosphate-buffered 2.0% glutaraldehyde at room temperature for 2 hours. After repeated rinsing in 0.1 M phosphate buffer, the cells were post-fixed in 1.0% osmium tetroxide for 20 minutes. The slides were passed through a graded series of ethanol, infiltrated with Spurr epoxy resin, and fitted to inverted capsular molds containing fresh Spurr resin. After polymerization at 70° C, the hardened capsules containing the cells of interest were then “popped off” the surface of the glass slides by dipping the slides into liquid nitrogen. These blocks were trimmed and sectioned at 60-70 nm intervals with a diamond knife onto mesh copper grids. The grids were contrast-enhanced with uranyl acetate for 15 minutes and lead citrate for 10 minutes and examined and photographed for

---

quantitative analysis with a Hitachi 7100 transmission electron microscope at magnifications ranging from 3000x to 30,000x.

#### **4.2.5 Coated sphere modeling and fitting**

A Mie theory model was fit to the control-cell angularly resolved scattering data as described in Chapter 3. Based on the results from that chapter, we assumed the functional form of the particle size distribution to be a bimodal log-normal distribution.

On the basis of our initial electron microscopy results, we fit a coated sphere model to the scattering from photodynamically treated cells. In the coated sphere case, we let the larger of the two log normal distributions obtained from fits to the control cell data swell as

$$r \rightarrow \alpha r \quad (4.1)$$

where  $r$  is the initial radius of the scattering sphere. This is equivalent to allowing the mean,  $\mu_j$ , and standard deviation,  $SD_j$ , of the distribution,  $\ell_j$ , to scale by the same constant  $\alpha$ . Mitochondria swelled by means of cytosol penetrating and forming a core in the center of the organelle, as shown in figure 4.5 C. The diameters of the core ( $D_{core}$ ) and of the coating ( $D_{coat}$ ) were fixed for a particular  $\alpha$  by conservation of mitochondrial mass and are related by

---

---

$$D_{core} / D_{coat} = \sqrt[3]{1 - (1/\alpha)^3} . \quad (4.2)$$

The index of refraction for the core and the surrounding medium was fixed at 1.38, and the index of the coating layer was fixed at 1.40 (see figure 4.5 D). With these assumptions based on the electron microscopy appearance of the treated mitochondria, the analysis of the angularly resolved scattering from the treated cells was then a one parameter fit in  $\alpha$ . As in the initial Mie theory fits, we constructed test functions,  $T$ , from particle size distributions. The difference was that for one log normal distribution, we used a coated sphere instead of a homogenous sphere model. The fit was again done with the simple downhill simplex by minimizing  $\chi^2$ . Uncertainties in  $\alpha$  were estimated by determining the values on either side of the  $\chi^2$  minimum that increased  $\chi^2$  by 1 [18].

## 4.3 Results

### 4.3.1 Scattering measurements from suspensions of intact cells

The plots in figure 4.1 show the angularly-resolved light scattering from intact control EMT6 cells and from cells subjected to ALA-sensitized photodynamic insult. The scattering from these two groups of cells is noticeably different for angles less than about 30 degrees. For larger angles, scattering from the two groups is virtually identical. It is apparent that the photodynamically-

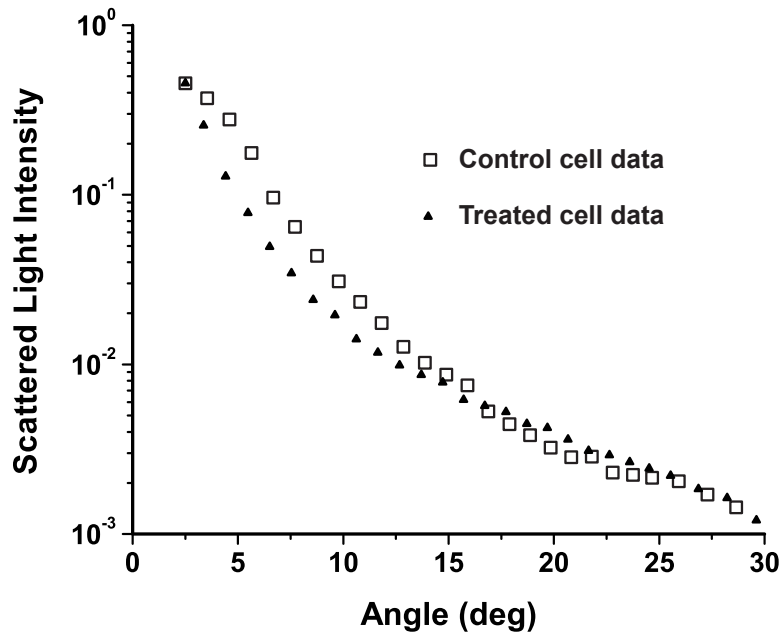


**Figure 4.1.** Angularly resolved light scattering from untreated, intact EMT6 cells (open squares) and from EMT6 cells subjected to photodynamically-induced oxidative stress (filled triangles). The treated cells scatter less light at small angles and the distribution is more forward peaked. Error bars are omitted for clarity.

---

treated cells scatter less total light than the control cells over this angular range and that the scattering distribution from the treated cells is more forward directed.

### **4.3.2 Scattering results from isolated mitochondria**

Scattering measurements from mitochondria isolated from rabbit liver were done in much the same manner as were the measurements from whole cells. Instead of HBSS, we used Tris buffer to suspend the mitochondria. We fit a log normal Mie theory model with a single particle size distribution to the angularly resolved data from the mitochondria and found a mean diameter of 0.89  $\mu\text{m}$  and a standard deviation of 0.2  $\mu\text{m}$ . Figure 4.2 displays representative scattering data with the Mie theory fit. The particle size distribution for the isolated mitochondria and the larger of the two distributions from the whole cells are compared in figure 4.3. The means of the distributions obtained from fits to the scattering data from isolated mitochondria and whole cells are very close (0.89 vs. 1.15  $\mu\text{m}$ , respectively), and the peaks of the distributions are almost identical (0.85 vs. 0.89  $\mu\text{m}$ ). This supports the assignment of the larger distribution in the cells to a predominantly mitochondrial origin.

### **4.3.3 Electron microscopy results**

We analyzed transmission electron microscopy images to obtain information about changes in mitochondrial morphology induced by ALA-

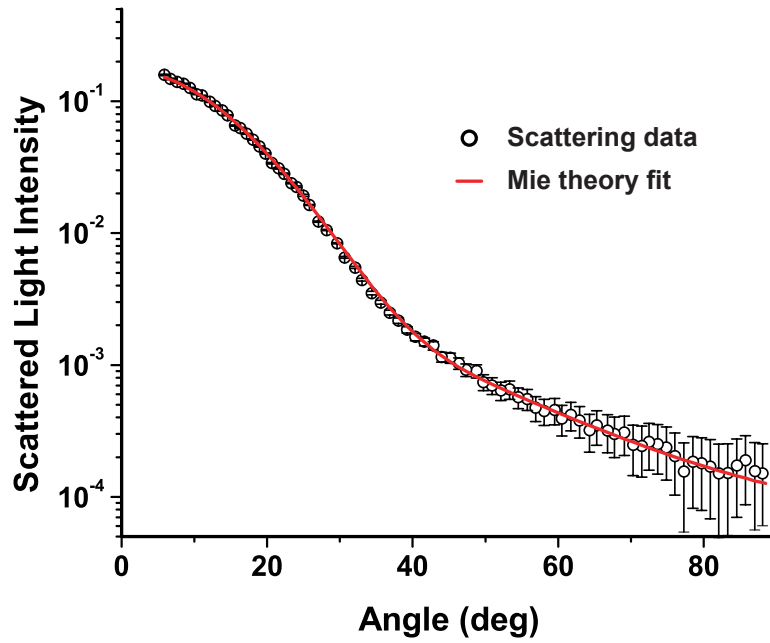


**Figure 4.2.** Scattering data from mitochondria isolated from rabbit liver (open circles) and a Mie theory fit (solid line).

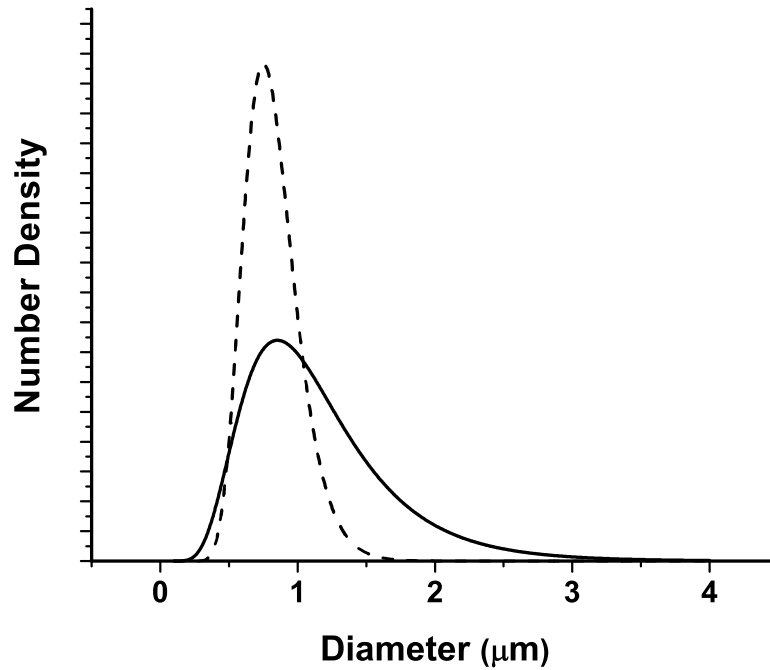


**Figure 4.3.** Particle size distributions obtained from the fits to the scattering data from whole cells (solid line) and isolated mitochondria (dashed line). The peaks of these two distributions are 0.89 and 0.85  $\mu\text{m}$ , respectively, and the corresponding means are 1.15 and 0.89  $\mu\text{m}$ .

---

sensitized oxidative stress. Because the absolute mitochondrial size may not be preserved in the fixation process, we did not attempt to use these data for rigorous size estimates. Rather, the electron microscopy images enabled us to determine gross morphologic features as well as relative changes between the two groups of cells.

We examined 70 nm-thick sections through the mitochondria, organelles with dimensions between 0.5 - 1.0  $\mu\text{m}$  and 1.0 – 4.0  $\mu\text{m}$  along the minor and major axes, respectively [19]. These cross sections are ellipsoidal in nature. Our basis for comparison of the control vs. treated cells was a measure of the major axis of this elliptical section for many mitochondria from both groups. Using the image processing package Image Pro (Media Cybernetics, San Diego, CA) we obtained 94 measurements of the major axes from EM sections of mitochondria that had been exposed to oxidative stress and 59 similar measurements from mitochondrial sections taken from the control group. A schematic of the sampling method is displayed as an inset of figure 4.4.

Figure 4.4 shows histograms of the major axes of the 70 nm-thick sections through mitochondria measured in the electron micrographs. Because of the elongated nature of a mitochondrion, the minor axis of the organelle is much more likely to be sampled than is the major axis. General features of these distributions of measurements are that the width of the mitochondrion is reported in the peak,

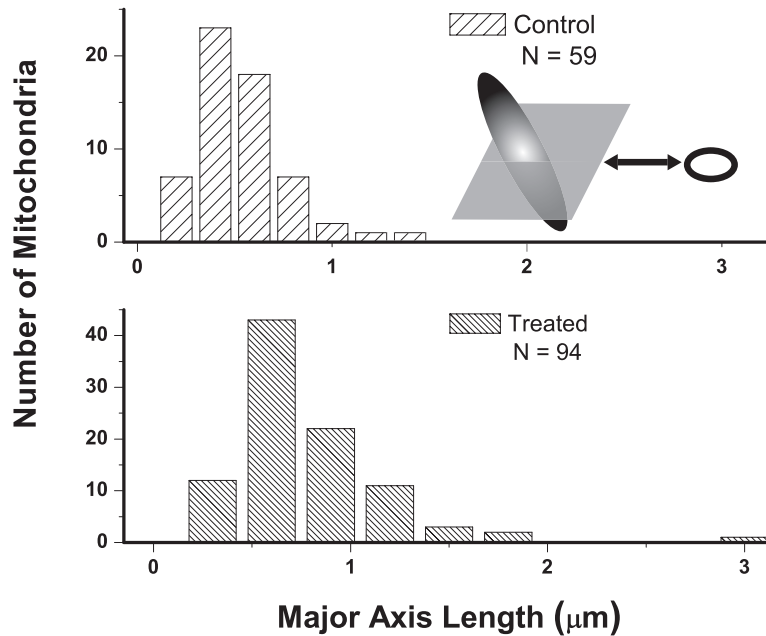


**Figure 4.4.** Histograms of the major axis dimensions of 70 nm-thick mitochondrial sections measured on electron micrographs obtained from cells pre- and post-oxidative stress. The major axis of each slice through an individual mitochondrion is depicted schematically in the inset. When an ellipsoidal object such as a mitochondrion is sectioned in this way, the peak of the distribution of major axis lengths corresponds to the width of the object, and the length is reflected in the tail of the distribution. Comparison of the peaks of these two distributions indicates a 20 % increase in the width of the mitochondria post photodynamic insult.

and the length is reported in the tail. The mitochondria in the cells exposed to photodynamic damage are swollen by 20% peak to peak relative to the control.

Important features of the mitochondrial structure and the response to photodynamic insult are shown in the electron micrographs of figure 4.5 (A,C). The distribution of the mitochondrial material becomes less homogeneous post treatment, and the mitochondria take on the appearance of a coated sphere, as depicted schematically in figures 4.5 B and D. The original mitochondrial material appears to be concentrated in the outer region of the organelle, and a core of non-electron-dense material is present in most of the organelles.

#### ***4.3.4 Scattering results for photodynamically-treated cells***

The model for interpreting the light scattering from the ALA-sensitized, irradiated cells was created to be consistent with both the electron microscopy data as well as the Mie theory fits to the control cells as described above. The Mie theory fits to control cells and isolated mitochondria provide strong evidence that mitochondria dominate the forward angle scattering in intact cells. Electron microscopy shows that the mitochondria undergo swelling as a result of the photodynamically-induced oxidative stress.

We considered several possible models based on various physical interpretations. A Mie theory model in which the mitochondria swelled in response to photodynamic insult and retained their original index of refraction

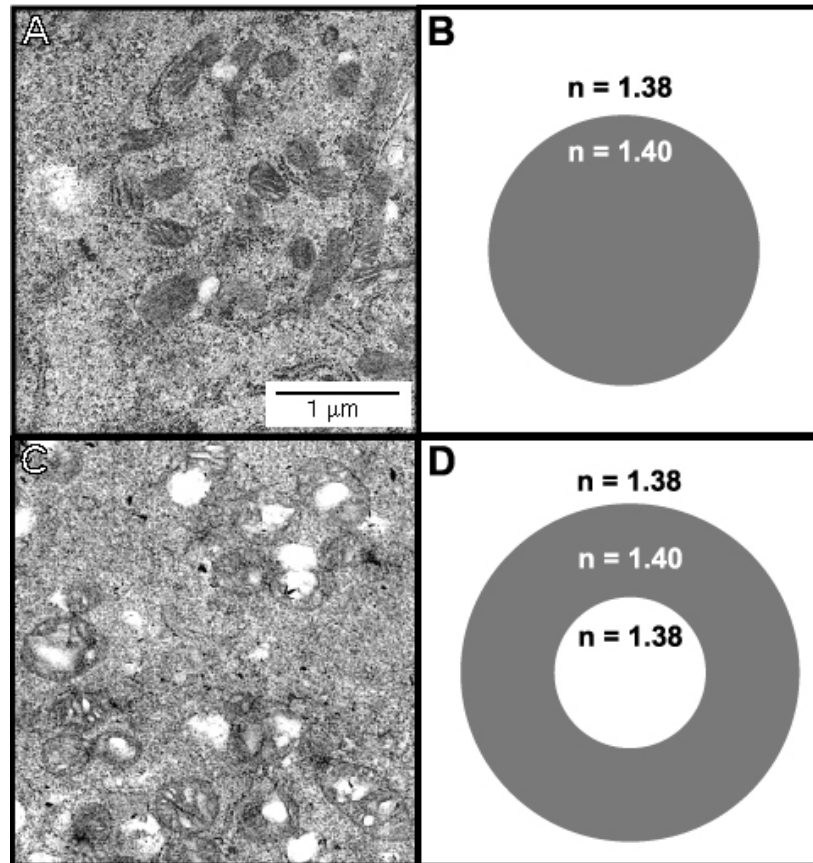


**Figure 4.5.** Electron microscopy images and dielectric models for control and photodynamically- treated mitochondria in EMT6 cells. (A) and (B) correspond to the control cells, while (C) and (D) correspond to mitochondria subjected to photodynamic insult. In the coated sphere model, the oxidative stress allows cytosol to penetrate the mitochondrion forming a swollen organelle with a cytosolic core in the center with refractive index 1.38.

---

could not represent the data, as this would cause the total scattering cross section to increase, and the data presented in figure 4.1 shows that the cross section in fact decreases. The possibility that, as a mitochondrion swelled, it took on a lower, homogeneous, volume-averaged index of refraction,

$$n_{swollen} V_{swollen} = n_0 V_0 + n_{cytosol} (V_{swollen} - V_0) \quad (4.3)$$

was also examined. Figure 4.6 shows how such a homogeneous swelling would affect the angularly resolved scattering from whole cells. It is clear that such a swelling effect is not consistent with the scattering angular distribution observed from the treated cells.

Again using the electron microscopy results such as those shown in figure 4.5, we adopted a coated sphere model as described above in the Methods section. We found that the index of refraction used for the material comprising the core (i.e., water vs. cytosol) was very important in terms of the resulting angularly resolved scattering signatures. Figure 4.7 illustrates the effects of mitochondria swelling by means of a ‘water filled’ coated sphere, where the index of refraction of the core was held at 1.33. As shown in the figure, this also is clearly not an appropriate model for the scattering from the cells subjected to photodynamic insult.

We were, however, able to fit the data quite well with a coated sphere model in which the core of the sphere was cytosol with a refractive index of 1.38.

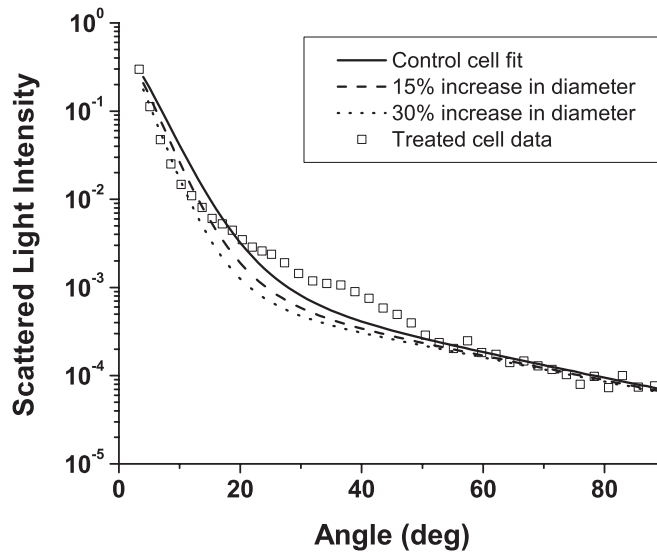


**Figure 4.6.** A Mie theory model based on a volume-averaged, homogeneous index of refraction is not compatible with scattering measured from cells subjected to photodynamic insult. The open squares are the angularly resolved scattering data from the treated cells. The solid line is the Mie theory fit to the control cell data, and the two dashed lines show the predictions of a model based on a homogeneous refractive index that is diluted by influx of cytosol into the mitochondrial volume.

---

As mentioned previously, we included mitochondria within the “large” population of scatterers obtained by the fits to the control cells, and we therefore let this population swell as coated spheres as described in Methods. The fits reported a 13% (+/- 2%) increase in diameter for this population in the PDT-treated cells as compared to the control case. The angularly-resolved scattering data from the photodynamically-treated cells and a cytosol core, coated sphere model fit are displayed in figure 4.8. The 13% swelling reported by the analysis of the scattering measurements is less than the 20% obtained by direct measurements of mitochondria using electron microscopy, a result which is consistent with the fact that the larger population of intracellular scattering centers contains a non-mitochondrial component. If one assumes that these non-mitochondrial scatterers do not swell immediately in response to photodynamic insult, the dilution of the magnitude of the mitochondrial swelling extracted from the fits to the whole-cell scattering data suggests that approximately 65% ( $0.13/0.20$ ) of the larger population are mitochondria.

## 4.4 Discussion

The data and analysis presented in this chapter establish the feasibility of monitoring stress-induced changes in mitochondrial morphology in intact, living cells without administration of exogenous agents. Our experiments confirm that, in this cell line, mitochondria contribute significantly to light scattering at angles

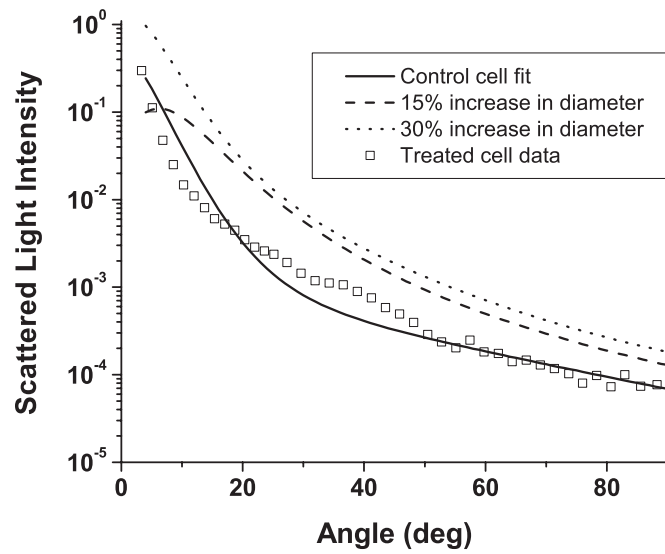


**Figure 4.7.** A coated sphere model assuming a water core (refractive index = 1.33) is not compatible with scattering from cells whose mitochondria have swelled in response to oxidative stress as shown in figure 4.5. The open squares are the measured scattering data from cells subjected to photodynamic stress, and the solid line is the Mie theory fit to the control cell scattering data. The two dashed curves are the theoretical results for 15% and 30% increases in mitochondrial diameter using a water-filled coated sphere model.

from approximately  $5 - 90^\circ$ . Evidence for this comes first from the comparison of the size distributions extracted from fits to the whole cell and isolated mitochondria scattering data. Probably more convincing, however, is the fact that the analysis of the angle-resolved scattering from cells subjected to mitochondrial oxidative stress is remarkably compatible with the morphology changes observed under electron microscopy of identically treated cells.

The angle-resolved scattering plotted in figure 4.1 shows clear differences between the EMT6 cells subjected to photodynamic insult and the control, untreated cells. We emphasize that these measurements were made immediately after irradiation, and that the cells were intact; no significant lysis was observed at these early time points. Although some loss of cell volume regulation is probably also happening concurrently, our measurements would likely not be sensitive to this. Whole-cell volume is reported in the extremely forward-directed scattering [20] that is not detected in our experiments, which begin sampling at about  $5^\circ$  from the incident laser beam.

Figure 4.2 presents angle-resolved data from a suspension of rabbit liver mitochondria. Here the Mie-theory fit is excellent, and the resulting size distribution, shown in figure 4.3, is significantly narrower than the large-diameter distribution that results from fits to the control cell data. There are two explanations for these observations. First, as stated above the larger-diameter

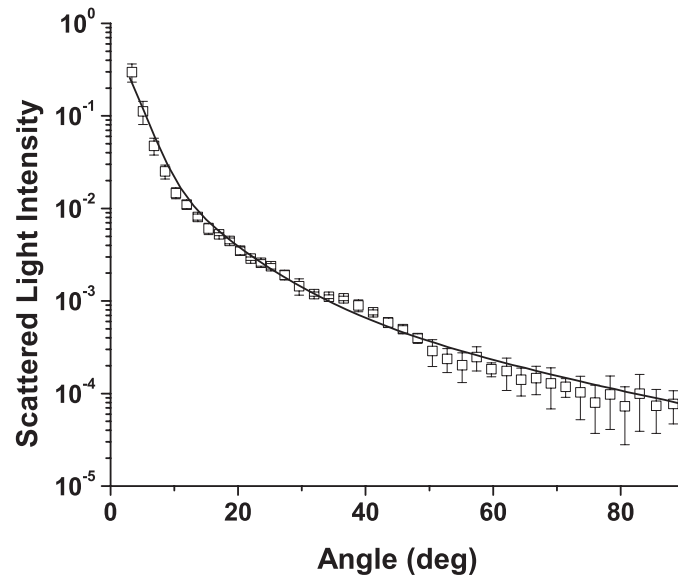


**Figure 4.8.** Scattering data (squares) from the cells subjected to photodynamic insult and a coated sphere fit that incorporates cytosolic filling of the inner mitochondrial compartment. The refractive index of the cytosol was assumed to be 1.38.

population of scatterers in the whole-cell case probably includes contributions from organelles other than mitochondria, and this will widen the size distribution. Second, with respect to the mitochondrial contribution itself, because the mitochondria in intact cells are ellipsoidal and randomly oriented while mitochondria in suspension tend to round, the isolated mitochondria will have a more tightly distributed range of effective diameters. Nevertheless, the peak and the mean of this distribution are in good agreement with those of the larger of the two scatterer populations from whole cells, as depicted in figure 4.3.

As noted above, this agreement is *one* piece of evidence that the larger size distribution extracted from fits to the whole cell scattering data includes a significant contribution from mitochondria. The second, and perhaps more compelling evidence, comes from the fact that photodynamic insult *changed* the mitochondria in specific ways, and a coated sphere interpretation of the scattering measurements reported this change correctly. Figures 4.4 and 4.5 summarize results of electron microscopy imaging performed on intact cells pre- and post-photodynamic stress. In particular, the representative EM images shown in Figures 4.5 A and C provided the rationale for the use of homogenous and coated sphere models in analyzing the scattering angular distributions from the control and treated EMT6 cells, respectively. Before leaving the images of figure 4.5, we note that the photodynamically-treated mitochondria shown in figure 4.5 C bear a

---

striking resemblance to mitochondria during state 4 to state 3 transition, as depicted for example in figure 14 of Hackenbrock [1].

In Figures 4.6, 4.7, and 4.8, we show the results of fitting the whole-cell scattering data from the treated cells using various candidate models that incorporated different assumptions about the morphology of the mitochondrial subjected to oxidative stress. The data are dramatically incompatible with models based on a homogeneously swollen sphere with a uniformly diluted refractive index (figure 4.6) and on a coated sphere in which the core has a refractive index equal to that of water (figure 4.7). The fact that the data are able to discriminate between these interpretations and one that incorporates a coated sphere with a cytosolic core is a measure of the excellent sensitivity of angularly-resolved light scattering to very specific changes in the morphology of mitochondria, at least in this cell line. Interestingly, a coated sphere model was used previously by Brunsting and Mullaney [21] to interpret scattering from Chinese hamster ovary (CHO) and from HeLa cells in terms of a nucleus surrounded by cytosol. Over part of the angular range studied in that work, the authors demonstrated in the CHO cells modestly better agreement with experiment using a coated vs. homogeneous sphere model. Results with the HeLa cells were not shown but were apparently less encouraging. In a study of the angular dependence of visible light scattering from *E. coli* cells, Cross and Latimer [22] had good success by treating the bacteria as a coated ellipsoid, with the coat in this case representing

the cell wall. As far as we are aware, ours is the first use of a coated sphere model to analyze the influence of morphological changes in mitochondria induced by any means on scattering angular distributions from whole cells, and it is the first direct experimental validation of a coated sphere model with EM. Although our coated sphere extension to a Mie theory analysis worked very well in this situation and seems to have captured the critical physical features of the problem, there does appear to be some structure in the angular distribution near 40 degrees from the treated cells (see figure 4.8) that is not reproduced by the fitting function. It is possible that a rigorous comparison with other methods of treating these kinds of data, such as the finite-difference time-domain approach described by Drezek et al. [23], would yield further insight. Finally, we emphasize that our measurements and analysis cannot strictly exclude the possibility that other organelles may also be responding to this form of oxidative stress in ways that may influence the scattering angular distributions.

There are several lines of investigation suggested by this study. It may be possible, for example, to use the methods described here to identify where changes in mitochondrial morphology occur in the apoptotic cascade and in the demise of cells subjected to a variety of insults [2]. This would enable a non-invasive assay capable of predicting the fate of cells without exogenous fluorescent reporters or other labeling. Encouraging work along these lines using optical scatter imaging microscopy has just been reported by Boustany et al. [24].

The sensitivity of the angle-resolved scattering to mitochondrial morphology and the similarity between the EM appearance of the mitochondria undergoing a state 4 to state 3 transition shown by Hackenbrock [1] and those of our figure 4.5 C suggest that these measurements could be useful in fundamental studies of mitochondria in intact cells. While studies of these kinds and others could be performed in suspension as we have done, the applicability of the light scattering technique would greatly expanded if it could be implemented using adherent cells. In this regard, it is encouraging that Bartlett et al. [25] recently suggested that mitochondrial signatures may be detected in a reflectance geometry using polarized light spectroscopy.

---

---

## References

1. C. R. Hackenbrock, "Ultrastructural bases for metabolically linked mechanical activity in mitochondria. I. Reversible ultrastructural changes with change in metabolic steady state in isolated liver mitochondria," *J. Cell Biol.* **30**, 269-297 (1966).
2. D. R. Green and J. C. Reed, "Mitochondria and apoptosis," *Science* **281**, 1309-1312 (1998).
3. J. R. Mourant, J. P. Freyer, A. H. Hielscher, A. A. Eick, D. Shen, and T. M. Johnson, "Mechanisms of light scattering from biological cells relevant to noninvasive optical-tissue diagnostics," *Appl. Opt.* **37**, 3586-3593 (1998).
4. L. T. Perelman, V. Backman, M. Wallace, G. Zonios, R. Manoharan, A. Nusrat, S. Shields, M. Seiler, C. Lima, T. Hamano, I. Itzkan, J. Van Dam, J. M. Crawford, and M. S. Feld, "Observation of periodic fine structure in reflectance from biological tissue: A new technique for measuring nuclear size distribution," *Phys. Rev. Lett.* **80**, 627-630 (1998).
5. V. Backman, R. Gurjar, K. Badizadegan, L. Itzkan, R. R. Dasari, L. T. Perelman, and M. S. Feld, "Polarized light scattering spectroscopy for quantitative measurement of epithelial cellular structures in situ," *IEEE J. Select. Top. Quant. Electron.* **5**, 1019-1026 (1999).
6. K. Sokolov, R. Drezek, K. Gossage, and R. Richards-Kortum, "Reflectance spectroscopy with polarized light: is it sensitive to cellular and nuclear morphology," *Opt. Express* **5**, 302-317 (1999).
7. A. Wax, C. Yang, V. Backman, K. Badizadegan, C. W. Boone, R. R. Dasari, and M. S. Feld, "Cellular organization and substructure measured using angle-resolved low-coherence interferometry," *Biophys. J.* **82**, 2256-2264 (2002).
8. B. Beauvoit, S. M. Evans, T. W. Jenkins, E. E. Miller, and B. Chance, "Correlation between the light scattering and the mitochondrial content of normal tissues and transplantable rodent tumors," *Anal. Biochem.* **226**, 167-174 (1995).

9. J. R. Mourant, T. M. Johnson, and J. P. Freyer, "Characterizing mammalian cells and cell phantoms by polarized backscattering fiber-optic measurements," *Appl. Opt.* **40**, 5114-5123 (2001).
10. J. R. Mourant, T. M. Johnson, V. Doddi, and J. P. Freyer, "Angular dependent light scattering from multicellular spheroids," *J. Biomed. Opt.* **7**, 93-99 (2002).
11. L. Packer, "Metabolic and structural states of mitochondria. I. Regulation by adenosine diphosphate," *J. Biol. Chem.* **235**, 242-249 (1960).
12. N. N. Boustany, R. Drezek, and N. V. Thakor, "Calcium-induced alterations in mitochondrial morphology quantified in situ with optical scatter imaging," *Biophys. J.* **83**, 1691-1700 (2002).
13. D. Kessel and Y. Luo, "Photodynamic therapy: a mitochondrial inducer of apoptosis," *Cell Death. Differ.* **6**, 28-35 (1999).
14. N. L. Oleinick, R. L. Morris, and I. Belichenko, "The role of apoptosis in response to photodynamic therapy: what, where, why, and how," *Photochem. Photobiol. Sci.* **1**, 1-21 (2002).
15. Q. Peng, K. Berg, J. Moan, M. Kongshaug, and J. M. Nesland, "5-Aminolevulinic acid-based photodynamic therapy: principles and experimental research," *Photochem. Photobiol.* **65**, 235-251 (1997).
16. M. Lam, N. L. Oleinick, and A. L. Nieminen, "Photodynamic therapy-induced apoptosis in epidermoid carcinoma cells. Reactive oxygen species and mitochondrial inner membrane permeabilization," *J. Biol. Chem.* **276**, 47379-47386 (2001).
17. A. E. Senior, S. E. McGowan, and R. Hilf, "A comparative study of inner membrane enzymes and transport systems in mitochondria from R3230AC mammary tumor and normal rat mammary gland," *Cancer Res.* **35**, 2061-2067 (1975).
18. P. R. Bevington, *Data Reduction and Error Analysis for the Physical Sciences*, (McGraw-Hill, New York, 1969).
19. G. E. Palade, "An electron microscope study of the mitochondrial structure," *J. Histochem. Cytochem.* **1**, 188-211 (1953).

- 
20. G. C. Salzman, S. B. Singham, R. G. Johnston, and C. F. Bohren, "Light scattering and cytometry," *Flow Cytometry and Sorting*, M. R. Melamed, T. Lindmo, and M. L. Mendelshoh, eds., (Wiley-Liss, New York, 1990), 81-107.
  21. A. Brunsting and P. F. Mullaney, "Differential light scattering from spherical mammalian cells," *Biophys. J.* **14**, 439-453 (1974).
  22. D. A. Cross and P. Latimer, "Angular dependence of scattering from Escherichia Coli cells," *Appl. Opt.* **11**, 1225-1228 (1972).
  23. R. Drezek, A. Dunn, and R. Richards-Kortum, "Light scattering from cells: finite-difference time-domain simulations and goniometric measurements," *Appl. Opt.* **38**, 3651-3661 (1999).
  24. N. N. Boustany, Y. C. Tsai, B. Pfister, W. M. Joiner, G. A. Oyler, and N. V. Thakor, "BCL-xL-dependent light scattering by apoptotic cells," *Biophys. J.* **87**, 4163-4171 (2004).
  25. M. Bartlett, G. Huang, L. Larcom, and H. Jiang, "Measurement of particle size distribution in mammalian cells in vitro by use of polarized light spectroscopy," *Appl. Opt.* **43**, 1296-1307 (2004).

# **Chapter 5. Index-of-refraction-dependent light scattering observed with organelle- localizing dyes**

## **5.1 Introduction**

There is an increasing body of work in the literature on the subject of light scattering from intact cultured cells and in tissues to quantify sub-cellular morphology. These reports initially focused on wavelength-resolved or angularly-resolved backscattering measurements from tissues, where nuclear sizes could be extracted [1, 2, 3]. In cultured cells, where scattering measurements are free from the diffusive background present in tissues, there have been a variety of reports demonstrating that light scattering is sensitive to smaller organelles, and particularly to mitochondrial morphology changes induced by a variety of stresses. Boustany et al. used an optical scatter imaging microscope to observe mitochondrial swelling from intact cells in response to calcium insult [4] as well as from cells undergoing apoptosis by staurosporine exposure [5]. Schuele et al. [6] were able to observe heat-induced mitochondrial morphology changes using wavelength-resolved backscattering measurements in cultured cells. Our own

studies revealed that angularly-resolved light scattering could be used to monitor oxidative-stress-induced changes in mitochondrial morphology [7].

Light scattering, in principle, has the ability to report both organelle sizes and relative changes in organelle sizes that are below the diffraction limit of an optical microscope. This was demonstrated by Fang et al. [8], who used wavelength-resolved backscattering measurements with 450-750 nm light to size polystyrene microspheres as small as 175 nm with 20-nm accuracy. The authors were also able to size zymogen granules, extracted from cells, with length scales as small as 150 nm and confirm their results with electron microscopy.

While light scattering from cells has been modeled using more complicated methods [4, 9], most researchers have used various Mie theory-based models to extract morphological information from their measurements. Mie theory, or the exact solution to scattering of an infinite plane wave by a homogeneous sphere, incorporates the parameters of particle size, particle refractive index, wavelength of light, and the refractive index of the surrounding medium. It has been shown that for organelle sizes smaller than nuclei and for refractive indices of organelles in cytoplasm reported in the literature [10, 11], the shape of both angularly-resolved [12] and wavelength-resolved light scattering [8] distributions from a single particle depends strongly on particle size and weakly on the refractive index. The relative refractive index of the particle primarily affects the total scattering cross section. Because of this, in many studies it has

been assumed in their respective inversion algorithms that all organelles have the same refractive index.

When measurements are made from an ensemble of particles, such as organelles within intact cells, it has been shown that the observable signal is governed by the product of the number density of particles of a particular size and their scattering cross sections [13]. In an angularly resolved measurement, we showed that we were sampling a phase function,  $P(\theta)$ , which when measured from a collection of particles that obeyed a size distribution  $\rho(r)$ , was written

$$P_{total}(\theta) = \frac{\int \sigma(r)\rho(r)P(r, \theta)dr}{\int \sigma(r)\rho(r)dr}, \quad (5.1)$$

where  $\sigma(r)$  is the scattering cross section. There is an analogous expression for a wavelength-resolved measurement. Because each particle's scattering cross section is dependent on its index of refraction, it is clear from equation (5.1) that a rigorous model of light scattering from cells needs to have a priori knowledge of the indices of refraction for different organelle populations that may blend together in size.

In this Chapter, we report results of light scattering measurements from cells stained with high extinction lysosomal- and mitochondrial-localizing dyes. We both model and exploit experimentally the effects of adding absorbing dyes to organelles, with specific emphasis on the dependence of absorber-induced

scattering changes on the inherent refractive index of organelles. Using these measurements and models, we provide strong evidence that there is a significant difference in the refractive index of mitochondria and lysosomes in EMT6 cells.

## 5.2 Materials and methods

### 5.2.1 Organelle localizing dyes

To stain lysosomes, we used N-aspartyl chlorin e6 (NPe6) (Light Sciences Corporation, Snoqualmie, WA). NPe6 has been shown to strongly localize to lysosomes [14]. Beyond this affinity to lysosomes, NPe6 has a high molar extinction, with a maximum of  $26,000 \text{ M}^{-1} \text{ cm}^{-1}$  at 642 nm in saline or  $45,600 \text{ M}^{-1} \text{ cm}^{-1}$  at 666 nm when bound to BSA.

As a mitochondrial stain with similar selectivity and extinction to NPe6, we chose the dye 2-(1-hexyloxyethyl)-2-devinyl pyropheophorbide- $\alpha$  (HPPH), which was prepared from pyropheophorbide- $\alpha$  according to the method of Pandey et al. [15]. This dye has been shown to localize strongly to mitochondria [16] and has a molar extinction of  $47,500 \text{ M}^{-1} \text{ cm}^{-1}$  at 665 nm. Representative fluorescence excitation and emission spectra for NPe6 and HPPH in EMT6 cells are shown in figure 5.1.

To verify that these experiments could be repeated with other organelle-localizing dyes, we used MitoTracker Deep Red 633 (Molecular Probes, Eugene,

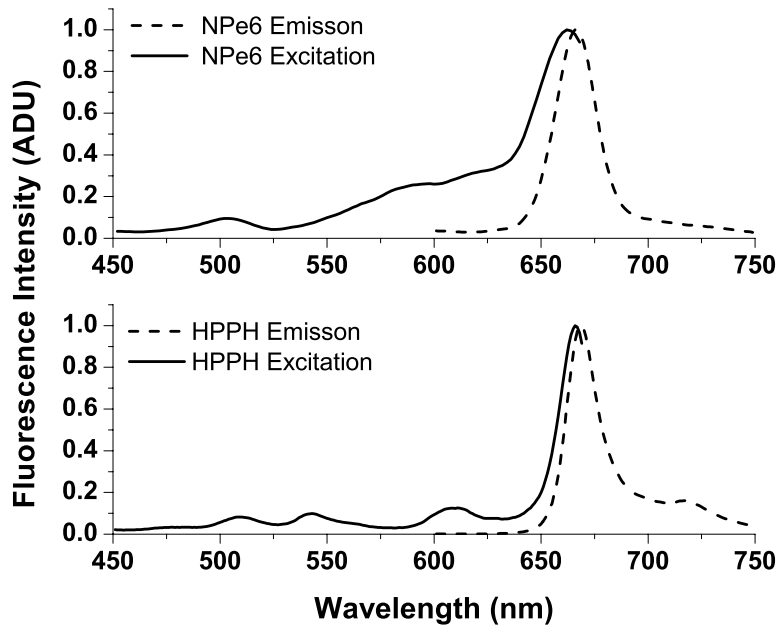


**Figure 5.1.** Fluorescence excitation and emission spectra for EMT6 cells loaded with NPe6 (upper panel) or HPPH (lower panel). For NPe6, emission spectra were excited at 400 nm, and excitation spectra were acquired monitoring emission at 720 nm. For HPPH, emission spectra were excited at 425 nm, and excitation spectra were acquired monitoring emission at 725 nm.

OR) with an extinction of  $194,000 \text{ M}^{-1} \text{ cm}^{-1}$  at 640 nm and LysoTracker Green (Molecular Probes, Eugene, OR) with an extinction of  $78,000 \text{ M}^{-1} \text{ cm}^{-1}$  at 505 nm to stain mitochondria and lysosomes, respectively.

### **5.2.2 Cell culture and staining**

For angularly-resolved light scattering and fluorescence excitation measurements, EMT6 mouse mammary sarcoma cells were maintained in monolayer in Eagle's basal medium with 10% fetal bovine serum (complete media) at  $37^\circ \text{ C}$  and 5%  $\text{CO}_2$ . When the cells reached 60-70% confluence, the media was removed, and cells were loaded with the appropriate dye. For NPe6 and HPPH loading, cells were incubated overnight in complete media at concentrations of  $50 \text{ }\mu\text{g/ml}$  and  $0.5 \text{ }\mu\text{M}$ , respectively. For MitoTracker Deep Red and LysoTracker Green loading, cells were incubated at  $250 \text{ nM}$  for 45 minutes and  $75 \text{ nM}$  for 2 h, respectively. The cells were then washed twice with Hanks' Balanced Salt Solution (HBSS), lifted from the plate with 0.25% trypsin, and then suspended in at least 1 part complete media per part trypsin. They were then centrifuged and re-suspended in HBSS at a concentration of approximately  $5 \times 10^6$  cells/ml.

For darkfield scattering spectroscopy measurements, EMT6 cells were grown on 25 mm round No. 1 thickness coverslips in complete media. They were

then incubated for 24 h in 50  $\mu\text{g/ml}$  NPe6 in complete media in the dark. Prior to a measurement, the cells were washed twice in HBSS.

### **5.2.3 Fluorescence spectroscopy**

Fluorescence measurements of cells stained with either NPe6 or HPPH as described above were made using a Varian Eclipse (Palo Alto, CA) fluorometer. Approximately  $10^9$  cells suspended in 400  $\mu\text{l}$  of HBSS were pipetted into a 1 cm pathlength cuvette. For NPe6, excitation scans were taken monitoring fluorescence emission at 720 nm, and emission spectra were taken with an excitation wavelength of 400 nm. For HPPH, excitation scans were taken monitoring fluorescence emission at 725 nm, and emission spectra were taken with an excitation wavelength of 425 nm.

### **5.2.4 Angularly-resolved light scattering measurements**

Our goniometer measurements have been described in Chapter 3. A scattering sample in aqueous suspension is placed in a cylindrical cuvette, which is positioned above the center of a rotary stage, and light from a laser is directed through the cuvette. In these experiments, we used 20 mW of 633 nm light from a HeNe laser, 20 mW of 488 nm light from an argon laser, or 5 mW of 658 nm light from a diode laser. Both the diode laser and the argon laser are coupled into

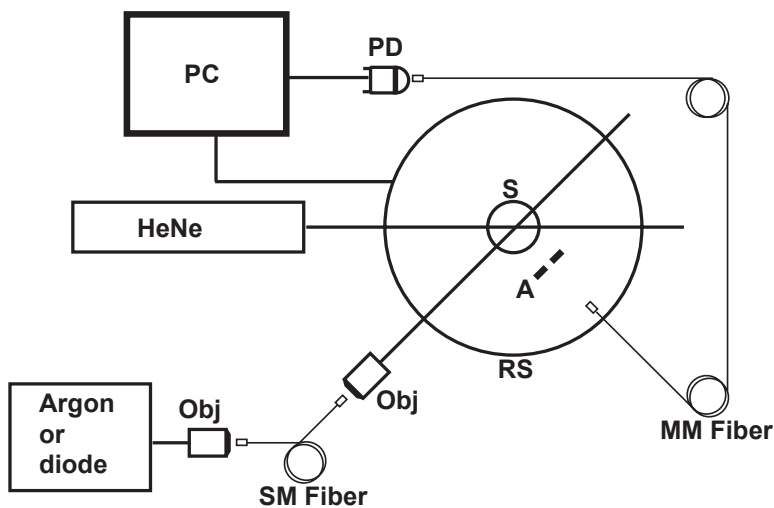


**Figure 5.2.** Schematic of our goniometer for multi-color angularly-resolved light scattering measurements. A sample, S, is placed above a rotary stage, RS. Light from a HeNe (633 nm), argon (488 nm), or diode (658 nm) laser is directed through the sample. The argon or diode lasers are coupled into a single mode (SM) fiber and then re-collimated using a pair of objectives, Obj. Scattered light is collected through an aperture, A, into a multimode (MM) fiber and measured by a photodiode (PD).

a single-mode optical fiber and then re-collimated using a 20x microscope objective with an NA of 0.4, while the collimated beam from the HeNe is sent directly to the cuvette. In all of our measurements, the laser light is linearly polarized perpendicular to the surface of the rotary stage. Light scattered from the sample is passed through a pinhole mounted midway to the edge of the rotary stage and collected by an optical fiber that is mounted at the edge. Light exiting the fiber is measured by a photodiode (New Focus model 2001, San Jose, CA). A PC-controlled stepper motor rotates the stage, and the angular position is read out from an optical encoder. The stage position and photodiode voltage are simultaneously recorded every  $2.5^\circ$ . The data acquisition is automated and controlled by a lab-built program written in LabView (National Instruments, Austin, TX). A schematic of our setup is shown in figure 5.2.

For each measurement, a background is taken with only HBSS in the cuvette. Cells are then added to a concentration of  $10^5$  cells/ml, and the measurements are taken over the angular range  $5-90^\circ$ . The background is subtracted from the data, and a factor of  $\text{Sin}(\theta)$  is multiplied to the data to correct for the intersection volume of the laser beam and the detector field of view [17].

### **5.2.5 Darkfield scattering spectroscopy measurements**

Darkfield scattering spectroscopy measurements are made using a method similar to that described by Curry et al. [18]. We use a Nikon Diaphot inverted

microscope with its oil-immersion darkfield condenser ( $NA = 1.43 - 1.2$ ) and a 20x,  $NA = 0.75$ , objective. The light source is the 50 W filament lamp normally used for brightfield. At the 35 mm camera port, a 1 inch diameter lens tube is mounted via a Nikon bayonet-to-C-mount adapter (B&H Photo Video #GBCMN, New York, NY). Light scattered into the objective is collected by a plano-convex lens ( $f = 50.0$  mm) mounted in the end of the lens tube proximal to the microscope. This light is then coupled into a 200  $\mu\text{m}$  core, 0.22 NA multimode fiber mounted at the focus of the lens. The output of the optical fiber is spectrally resolved with a resolution of 3 nm and digitized at 16 bits by a spectrometer (BWTek BTL111-OEM, Newark, DE). Figure 5.3 shows a schematic of this setup.

To measure darkfield spectra of cells grown on coverslips, the 25 mm round coverslip is placed cell-side down on a second 43 x 50 mm square No. 1 thickness coverslip to form a slide. Approximately 10  $\mu\text{l}$  of HBSS is placed between these two coverslips. The slide is then placed on the stage as shown in figure 5.3, and brought into focus under darkfield using the eyepiece. A spectrum of the field is then taken with integration times of 3-5 s.

The darkfield spectra were corrected for dark counts and the system spectral throughput. For each measurement, a dark spectrum was acquired and subtracted from the data. The spectral throughput of the system was measured by removing the darkfield condenser, which is reflective and should have minimal

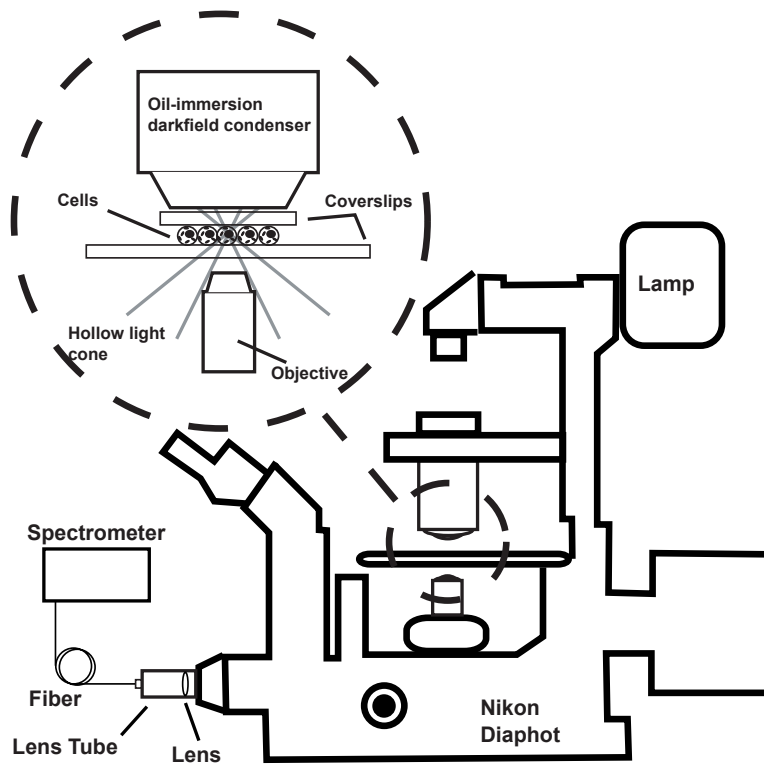


**Figure 5.3.** Schematic of our darkfield spectroscopy setup. This experiment is built around a standard inverted microscope fit with a darkfield condenser. The oil-immersion darkfield condenser forms a hollow light cone that misses the objective. Light scattered from the cell monolayer is collected by the objective. This light is transmitted through the internal microscope optics to the camera port, where it is collected by an optical fiber via a lens mounted inside a lens tube. The scattered light is then spectrally resolved and detected by a spectrometer.

---

chromatic aberrations, and placing the TiO<sub>2</sub> diffusing plate described by Hull and Foster [19] at the focus of the objective. As a second method of measuring the throughput, we created a slide as described above with a paste of the scattering standard MgO [20] in water, and recorded a spectrum with the darkfield condenser in place. This second method gave us an identical correction spectrum.

The darkfield spectrum is a wavelength-resolved measurement of light scattered from the sample and into the objective. As stated above, the NA range of the oil-immersion darkfield condenser is 1.43-1.2, which corresponds to an effective ‘air NA’ of 0.94-0.8, and the objective has an NA of 0.75. These NAs are such that the smallest angle into which light could be scattered from the sample and into the objective is 3.8°, and the largest angle is 116.2°. Thus we can model our darkfield scattering spectrum,  $I(\lambda)$ , as

$$I(\lambda) = A \int_{\theta=3.8^\circ}^{116.2^\circ} P_{total}(\theta, \lambda) \sin(\theta) d\theta, \quad (5.2)$$

where  $A$  is a constant and  $P_{total}$  is as written in equation (5.1). The signal as written in equation (5.2) is similar to an integration of our angularly resolved measurements described above.

### 5.2.6 Mie theory fitting to angularly resolved light scattering data

A Mie theory model was fit to angularly-resolved light scattering data by methods similar to those reported in Chapter 3. We assumed that our bulk light scattering signal was a sum of uncorrelated scattering from homogeneous spheres characterized by their radius,  $r$ , and a refractive index of 1.4 surrounded by medium of refractive index of 1.38 to approximate organelles in cytosol [10,11]. We further assumed that these spheres obeyed a particle size distribution,  $\rho$ , that was a weighted sum of log normal distributions,  $\ell_j(r)$ , as

$$\rho(r) = \sum_j a_j \ell_j(r). \quad (5.3)$$

Based on our previous results [13], we used a bimodal distribution in  $\rho$  to model whole-cell scattering from those cells not subjected to NPe6. We used Mie theory to calculate the angular scattering distribution,  $S(\theta, r)$ , which in the language of equation (5.1) is written

$$S(r, \theta) = \sigma(r)P(r, \theta) \quad (5.4)$$

for individual particles, and from these distributions we calculated test functions,  $T(\theta)$ , such that

$$T(\theta) = \int \sigma(r)\rho(r)P(r, \theta)dr . \quad (5.5)$$

These  $T(\theta)$  are functions of six parameters, which are the means,  $\mu_j$ , widths (standard deviations),  $w_j$ , and relative amplitudes,  $a_j$ , for two populations. These parameters were adjusted by an iterative, nonlinear fit to minimize the function

$$\chi^2 = \sum_n \frac{(D_n - T_n)^2}{v_n}, \quad (5.6)$$

where  $D_n$  represents the  $n$ th data point,  $T_n$  is the corresponding value of the test function, and  $v_n$  is the corresponding variance.

To model changes in angularly-resolved light scattering observed in the presence of NPe6, we fit an absorbing sphere model to our scattering data. Based on calculations presented in the Results section, we adopted a simplified absorbing sphere model in which the addition of absorption reduced the scattering cross section of an organelle population and had no effect on that population's angular distribution of scattered light. We fit this to the control cell and NPe6-stained cell data simultaneously, letting  $\rho(r)$  be a tri-modal version of equation (5.3) and forcing the particle size distribution to be the same for the two cell populations. We then built test functions for the two data sets independently as

$$\begin{aligned}
 T^{control}(\theta) &= \int \sigma(r)P(r, \theta) \times [a_1 \ell_1 + a_2 \ell_2 + a_3 \ell_3] dr \\
 T^{NPe6}(\theta) &= C_{cell} \int \sigma(r)P(r, \theta) \times [a_1 \ell_1 + a_2 \ell_2 + C_{\sigma} a_3 \ell_3] dr
 \end{aligned}
 \tag{5.7}$$

which are identical except for the constants  $C_{\sigma}$ , which is a model for the ratio of the scattering cross section of the stained population to its corresponding unstained population, and  $C_{cell}$ , which is an additional constant to account for any errors in the counting of the cell densities during the measurements.

The two test functions are cumulatively governed by 11 input parameters, namely the means,  $\mu_j$ , widths,  $w_j$ , and relative amplitudes,  $a_j$ , of the three populations and the additional two constants,  $C_{cell}$  and  $C_{\sigma}$ . We then minimized the function

$$\chi^2 = \sum_n \frac{(T_n^{control} - D_n^{control})^2}{v_n^{control}} + \sum_r \frac{(T_r^{NPe6} - D_r^{NPe6})^2}{v_r^{NPe6}}, \tag{5.8}$$

where  $T$ 's,  $D$ 's, and  $v$ 's are as in equation (5.6) but for the control or NPe6-stained case.

## 5.3 Results

### 5.3.1 Angularly resolved scattering in the presence of NPe6

Informed by the excitation spectrum of NPe6 shown in figure 5.1, we investigated light scattering from cells loaded with this dye versus scattering from cells that were unstained using three different laser lines, 488 nm, 633 nm, and 658 nm, representing wavelengths of low, medium, and high NPe6 absorption, respectively. As shown in panel (A) of figure 5.4, the angular distributions of scattered light for both NPe6-loaded and control cells at 488 nm are nearly indistinguishable. When these scattering data were fit by a Mie theory model as described by equations (5.5) and (5.6), the fitting algorithm returned virtually identical parameters for the two cases that were consistent with studies presented in Chapter 3, providing evidence that NPe6 staining does not change overall cell or organelle morphology.

As shown in panel (B) of figure 5.4, there are differences in the angularly-resolved light scattering at 633 nm between control cells and cells stained with NPe6. The two scattering spectra are very similar for scattering angles less than 15° and for angles greater than 60°, while the scattering changes are most pronounced near 30°. The statistical significance of this change was assessed by a  $\chi^2$  test between the control and NPe6-loaded data sets as described

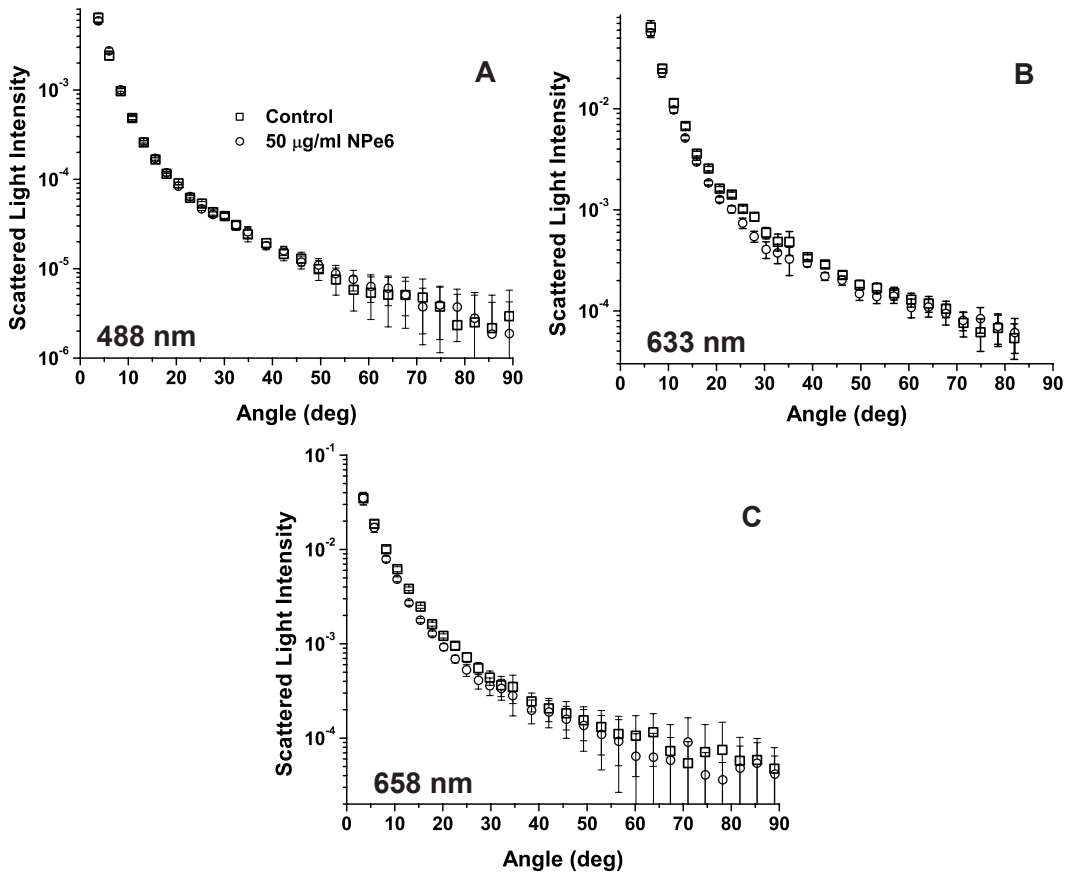


**Figure 5.4.** Representative angularly-resolved light scattering data for cells loaded with NPe6 (circles) and control cells (squares) at 488 nm (A), 633 nm (B), and 658 nm (C). At 488 nm, the two curves are indistinguishable. At 633 nm, the two curves are virtually identical in the forward- and side-scattering regions, but there is a reduction in scattering in the range 15-30° in the NPe6-loaded cells. At 658 nm, there is an angular-dependant scattering change similar to that at 633 nm, but with a slightly larger angular range and with a larger magnitude near 30°.

by Bevington and Robinson [21]. We found a  $p < 0.001$  that the differences in these data sets were due to statistical fluctuations. This scattering change is dramatically inconsistent with the mitochondrial-type perturbations reported in Chapter 4, where the scattering changes associated with mitochondrial swelling manifested themselves in the first  $20^\circ$ . Within a Mie theory model, changes at these larger angles are consistent with scattering from particles smaller than mitochondria.

The scattering comparison was made at a third wavelength, 658 nm, chosen to be near NPe6's absorption maximum. These data are displayed in panel (C) of figure 5.4. At this wavelength, we see a scattering change that is similar to that observed using 633 nm, but with a slightly greater magnitude, both in the angular range and maximum relative intensity, again providing evidence for a chromatic effect.

### **5.3.2 Darkfield spectroscopy**

Using darkfield spectroscopy we were able to further establish the relationship between scattering changes and NPe6 absorption. As stated in equation (5.2), a darkfield spectrum is derived from wavelength-resolved measurements of scattering integrated over a range of angles defined by the NAs of the illumination and detection optics. Darkfield scattering spectra were acquired for cells grown on coverslips with and without incubation with 50  $\mu\text{g/ml}$

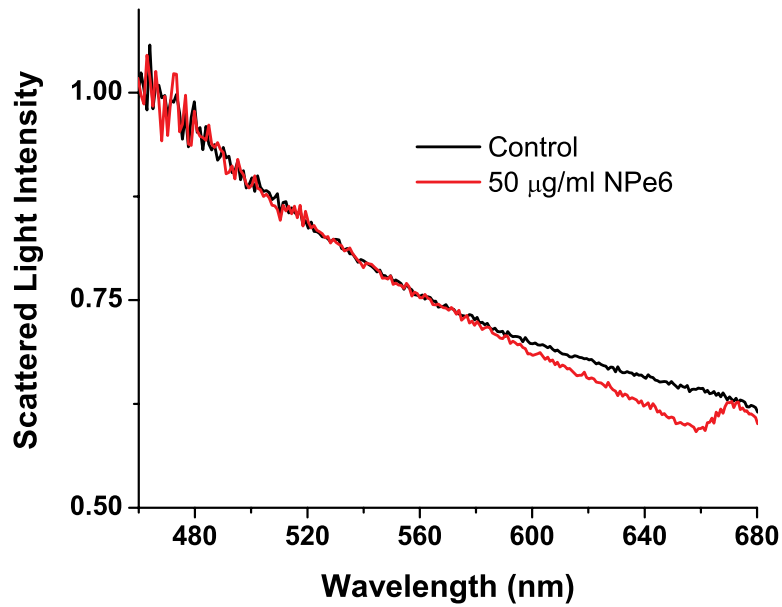


**Figure 5.5.** Representative darkfield spectra for NPe6-loaded (red) and control (black) cells. These curves were normalized to 1 at 480 nm. The feature near 680 nm is fluorescence emission from NPe6.

NPe6. Representative spectra are shown in figure 5.5. These two spectra are identical from approximately 480 nm to 560 nm. Beyond 580 nm, control cells scatter noticeably more light than cells loaded with NPe6. At wavelengths corresponding to the laser lines used in the angularly-resolved study, the darkfield spectra reveal that control cells scatter the same amount of light into the objective at 488 nm, roughly 4% more light at 633 nm, and 6% more light at 658 nm. The feature near 670 nm that appears in the scattering spectrum of NPe6-loaded cells is fluorescence emission (see figure 5.1). When the darkfield spectra displayed in figure 5.5 are compared to the fluorescence excitation spectrum for NPe6 displayed in figure 5.1, we see that the magnitude of the scattering change scales with the absorption coefficient of NPe6.

### **5.3.3 Modeling complex refractive index**

As observations both in darkfield spectroscopy and angularly-resolved light scattering measurements suggest that light scattering changes were associated with the absorption band of NPe6 in lysosomes, we used Mie theory to model the effects of adding a dye with large absorption directly to organelles. Absorption in a particle is represented by the imaginary part of the particle's complex refractive index,  $n$ , as

$$n = n_r + in_i . \tag{5.9}$$

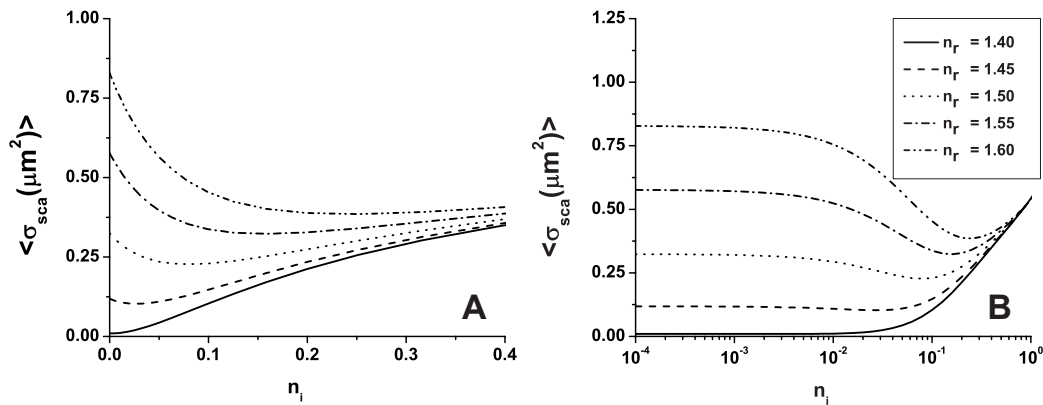
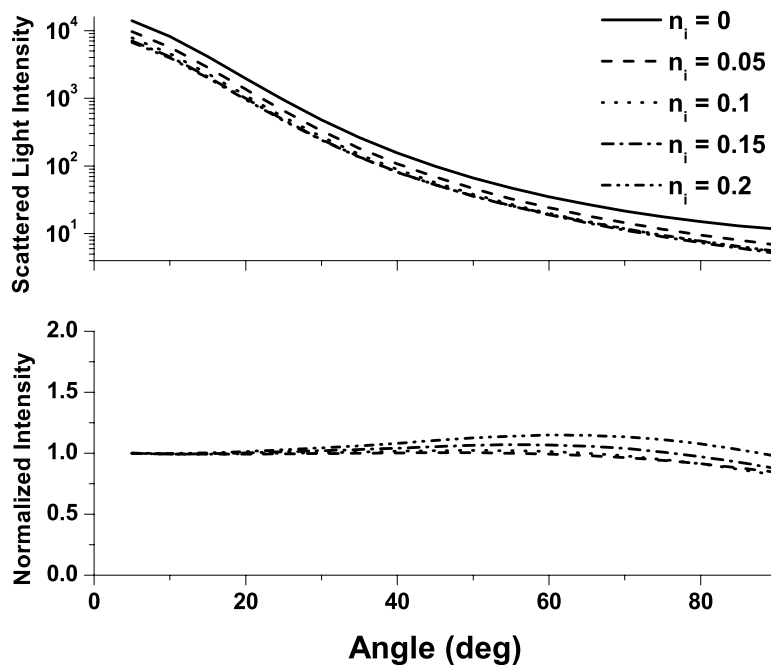


**Figure 5.6.** Mie theory calculations of the mean scattering cross section at 633 nm,  $\langle \sigma_{\text{sca}} \rangle$ , versus the imaginary part of the refractive index for a candidate population of lysosomes that obey a log-normal size distribution with mean and standard deviation of 0.7 and 0.3  $\mu\text{m}$ , respectively. The various curves represent populations with differing real parts of their refractive index. The horizontal axis was plotted on both a linear (A), and a logarithmic (B) scale. For particles with a high real part of the refractive index, the scattering cross section drops quickly with absorption for  $n_i$  less than 0.1 as demonstrated in (A). For smaller real parts of the refractive index, this effect is negligible as shown in (B).

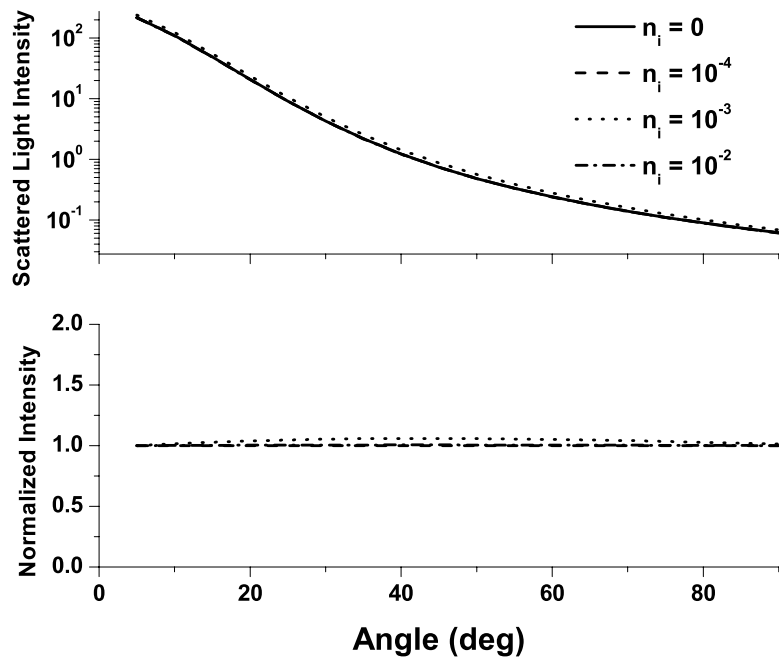
---

Figure 5.6 shows the mean scattering cross section,  $\langle\sigma_{\text{sca}}\rangle$ , of a candidate lysosomal population, with a mean diameter of  $0.7\ \mu\text{m}$  and a standard deviation of  $0.3\ \mu\text{m}$  at  $633\ \text{nm}$ . On the horizontal axis is  $n_i$  from equation (5.9), and the various curves represent different values of  $n_r$  spanning 1.4-1.6. As was observed by Kattawar and Plass [22], for particle sizes roughly the size of the incident wavelength there are regions of this space where increasing  $n_i$  can serve to reduce the mean scattering cross section, and this effect is highly dependent on  $n_r$ . For  $n_r = 1.4$ , which is near the value that has been reported for organelles in the literature [10, 11], there is negligible reduction in the mean scattering cross section as  $n_i$  increases, whereas for higher values such as  $n_r = 1.6$ , the mean cross section can differ by as much as a factor of 2.

Similar forward calculations were made to determine what, if any, effects on the angular distribution of scattered light would occur with the addition of an absorber. The results of these are displayed in figures 5.7 and 5.8. We chose to represent both  $n_r = 1.4$  and  $n_r = 1.6$  to bracket the range of refractive indices shown in figure 5.6. For  $n_r = 1.6$ , we found that for values of  $n_i$  less than 0.1, there was very little change in the angular dependence of scattered light. For larger values of  $n_i$ , there was a small shift in the angular distribution such that light scattered into large angles was as much as 15% higher relative to the light scattered into the forward direction. This is apparent in the lower panel of figure



**Figure 5.7.** Mie theory calculations of the angular dependence of light scattering at 633 nm for candidate populations of lysosomes with a mean size and standard deviation of 0.7 and 0.3  $\mu\text{m}$ , respectively, an  $n_r = 1.6$  and  $n_i$  ranging from 0 to 0.2. The upper panel shows the differential cross section for the various  $n_i$ . The lower panel displays the angularly-resolved light scattering distribution of a non-absorbing ( $n_i = 0$ ) particle, the solid curve from the top panel, divided by that of a distribution with an  $n_i$  as shown in the legend. These curves are then normalized to 1 at  $5^\circ$ .



**Figure 5.8.** Plots similar to those shown in figure 5.7 for populations with  $n_r = 1.40$ .

5.7. For the case of  $n_r = 1.4$ , which is close to the reported refractive index of organelles [11], we examined a broad range of  $n_i$  to look for any change in the angular distribution of scattered light. As displayed in figure 5.8, we saw no change in the angular distribution of light scattered for values of  $n_i$  less than 0.1. For larger values, there was a slight shift in the angular distribution, however this cannot be responsible for our observed scattering changes described above, as for these values the scattering cross section increases (see figure 5.6).

#### ***5.3.4 Angularly resolved scattering in the presence of HPPH***

The scattering changes induced by the addition of NPe6 raise the question of whether or not the phenomenon of adding absorption to mitochondria can also change the light scattering distribution from whole cells. To this end, angularly-resolved light scattering measurements were taken for cells loaded with 0.5  $\mu\text{M}$  HPPH, which was specifically chosen for its high extinction and its strong localization to mitochondria. Multiple angularly-resolved measurements were taken for control and HPPH-loaded cells at 658 nm, which is near the absorption maximum of HPPH as shown in figure 5.1. The results of these experiments are displayed in figure 5.9. There were no discernable changes in angularly-resolved light scattering between the control and HPPH-loaded cell groups.

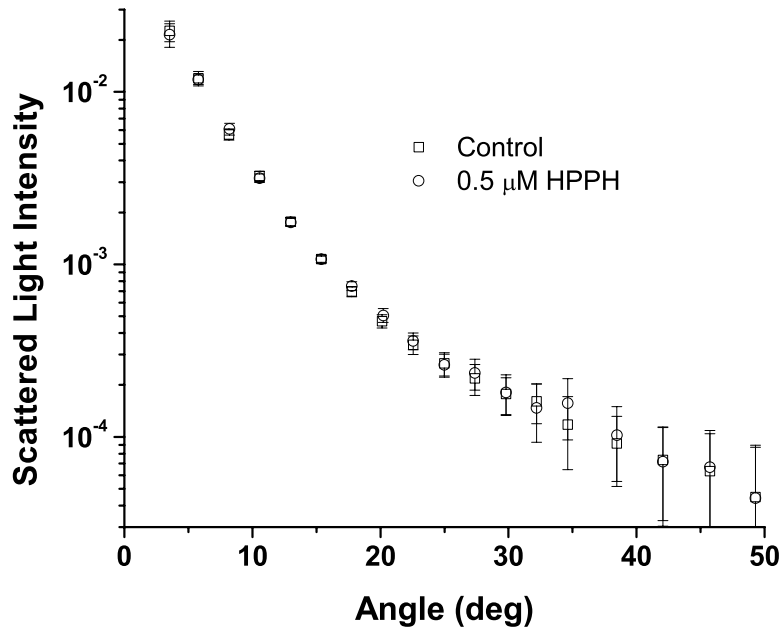


**Figure 5.9.** Representative angularly-resolved light scattering data for cells loaded with HPPH (circles) and control cells (squares) at 658 nm. There are no data points outside the error of the measurement. These data have been plotted over a smaller angular range to highlight the regions where we would expect to see any scattering changes due to mitochondria (0-20°) or lysosomes (20-50°).

---

### **5.3.5 Fits to angularly-resolved measurements**

A Mie theory model for angularly-resolved light scattering at 633 nm was fit to both control and NPe6-stained cells individually using the methods outlined in equations (5.5) and (5.6). When fit individually, both data sets were compatible with a bi-modal particle size distribution and were found to be incompatible with a tri-modal distribution in particle size using this analysis. There was, however, a shift toward larger particles being responsible for the light scattering signal from NPe6-stained cells, consistent with a lower scattering cross section from NPe6-stained lysosomes.

Informed by our calculations of scattering from spheres with a complex refractive index, we fit an absorbing sphere model to our angularly-resolved light scattering data at 633 nm using equations (5.7) and (5.8). As displayed in figure 5.6, the addition of absorption can have significant impact on the scattering cross section when the real part of the refractive index is sufficiently high. Also, there is minimal change in the angular distribution of scattered light for regions of figure 5.6 where  $\langle\sigma_{\text{sca}}\rangle$  is decreasing with increasing  $n_i$  (see figure 5.7). Thus, in our model, the addition of NPe6 simply changes the scattering cross section,  $\sigma_{\text{sca}}$ , of each lysosome by a dimensionless factor  $C_\sigma$ .

Using the contrast between the angularly-resolved light scattering measurements for NPe6-stained and the unstained cells at 633 nm shown in figure

5.4 B, we were able to isolate a third population made up of lysosomes,  $\ell_3$  from equation (5.7), whose scattering cross sections changed in response to staining with NPe6. The parameters for this population obtained by fitting our model to 5 different data sets taken on different days returned particle size distributions typical of 0.6 +/- 0.3  $\mu\text{m}$  particles, with the exact values extracted varying from data set to data set within this range. To bracket the returned parameters, the smallest particle size distribution had a mean of 0.4  $\mu\text{m}$  with a standard deviation of 0.2  $\mu\text{m}$ , while the largest had a mean and standard deviation of 0.8 and 0.3  $\mu\text{m}$ , respectively. We found that  $C_\sigma$  varied between 0.7-0.2, with a typical value near 0.5. If we define the relative contribution to the total cross section of the  $j^{\text{th}}$  population,  $R_j$ , as

$$R_j = \frac{\int a_j \ell_j(r) \sigma(r) dr}{\sum_k \int a_k \ell_k(r) \sigma(r) dr}, \quad (5.10)$$

where the sum is over the three populations, then the contribution of this population was found to be between 10-16 % of the scattering cross section. This is remarkably consistent with darkfield spectroscopy measurements at 633 nm. We found experimentally that the darkfield signal was roughly 4% lower for NPe6-stained versus control cells at 633 nm, and with  $C_\sigma$  from equation (5.7) being 0.5, our model for the angularly-resolved data predicts that NPe6-stained

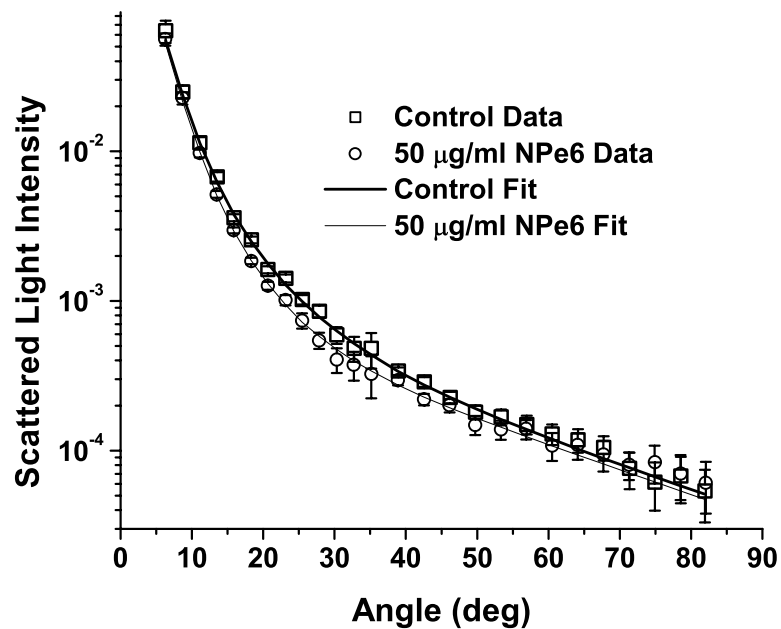


**Figure 5.10.** Angularly-resolved light scattering data and absorbing sphere fit as described in the text. The fit parameters returned a stained population of spheres of sizes consistent with lysosomes.

cells scatter between 5-8% less light than control cells at this wavelength. Representative absorbing sphere fits to the data are displayed in figure 5.10. To determine whether the returned fits for control and NPe6-stained cells were statistically different, we calculated the  $\chi^2$  goodness of fit parameters [21] for the best fits to the control and NPe6-stained data sets, which are the thin and thick solid lines in figure 5.10, respectively. We then asked whether the best fit to the control cell data was a good fit to the data from NPe6-stained cells and vice versa. In both of these mismatched cases,  $\chi^2$  increased by a factor of 25.

An interesting result of this study is that when this tri-modal absorbing sphere model was applied, the organelle population  $\ell_1$  from equation (5.7), which was responsible for 75-85% of the signal, was virtually identical for each measurement that was made. This population was characterized by a mean particle size and standard deviation of 1.3 and 0.6  $\mu\text{m}$ , respectively. The mean size extracted by our tri-modal model for this population was slightly larger, 1.3 versus 1.1  $\mu\text{m}$ , than for a similar population reported in Chapter 3, which was attributed to a combination of mitochondria and lysosomes. This discrepancy is consistent with the smaller organelles, lysosomes, now being isolated from this population in the absorbing-sphere tri-modal model, and the size parameters for  $\ell_1$  here principally representing mitochondria. The final population,  $\ell_2$  from equation (5.7), with a contribution to the total scattering cross section,  $R_2$ , of only

5%, was characterized by particles with a mean size and a standard deviation of 0.2 and 0.05  $\mu\text{m}$ , which is very similar to the population previously identified in Chapters 3 and 4 to be made up of secretory granules or other small subcellular compartments. The three populations, their mean diameters, and their contributions to the scattering cross sections in whole cells are summarized in Table 5.1.

### ***5.3.6 Scattering from cells stained with Mito- and LysoTracker dyes***

NPe6 and HPPH were chosen for their organelle selectivity and high extinction, as well as for their red absorption bands, which could be readily sampled by our lasers. To address whether or not these observations could be repeated using more common organelle-specific stains, we chose LysoTracker Green, and MitoTracker Deep Red. We observed changes in angularly-resolved scattering between cells stained with LysoTracker Green and control cells at 488 nm that were consistent with 0.7  $\mu\text{m}$  particles when both data sets were fit simultaneously using equations (5.7) and (5.8). There were no scattering changes in angularly-resolved light scattering between these two cell groups when the measurement was made at 633 nm. When angularly-resolved scattering was measured from cells loaded with MitoTracker Deep Red versus control cells at 633 nm, no changes were observed (data not shown).

Population Number ( $l$ )	Organelle	Mean ( $\mu\text{m}$ )	Std. Dev. ( $\mu\text{m}$ )	$R$ (%)
1	Mitochondria	1.3	0.6	80
2	Secretory Granules	0.2	0.05	5
3	Lysosomes	0.6	0.3	15

**Table 5.1.** Summary of typical diameters (means +/- std. dev.) of three populations of scatterers returned from simultaneous fits to angle-resolved scattering from NPe6-loaded and control cells. The population numbers,  $l$ , are defined in equation (5.7).  $R$  is the relative contribution to the total scattering cross section for each of the populations, as defined by equation (5.10) in the text.

## 5.4 Discussion

The data presented in this Chapter demonstrate a phenomenon that, to the best of our knowledge, has not been described before. We found that adding a lysosome-specific, strongly absorbing dye to EMT6 cells affects the scattering of light from these cells. At wavelengths near the absorption maximum of NPe6, scattering changes manifested themselves both in an angularly-resolved and integrated sense. Using a combination of angularly-resolved scattering measurements at three different wavelengths (figure 5.4) and a method to obtain a wavelength-resolved measurement of angle-integrated scattering (figure 5.5), we were able to show that these effects were prominent only in regions of significant NPe6 absorption. Because this phenomenon only occurs at wavelengths where absorption is high, it cannot be due to an NPe6-induced morphology change.

The forward calculations shown in figure 5.6 are striking in terms of how differently the average scattering cross section of these particle populations responds to the addition of an absorber, depending on the real part of the inherent refractive index. For organelle refractive indices reported in the literature, which are near 1.4, increasing the imaginary refractive index has little effect on the scattering cross sections for modest absorptions. As shown in figure 5.6, for regions of very high absorption the scattering cross section increases for all values

of  $n_r$ . The physical interpretation of this is one of a particle becoming increasingly metallic [23], which is an effect that is likely beyond what could be achieved by staining an organelle. In addition, for weakly absorbing particles,  $\langle\sigma_{\text{sca}}\rangle$  increases as the real part of the refractive index increases. As noted by Fang et al. [8], within the Rayleigh-Gans approximation for non-absorbing particles, the cross section should be proportional to  $(m-1)^2$ , where  $m$  is the ratio of the refractive index of the particle to that of the surrounding medium. In light of figure 5.4 A, where we see no significant scattering changes between the NPe6-labeled and unlabeled cell populations at 488 nm, we conclude that the addition of NPe6 to lysosomes has little effect on the real part of their refractive index.

When the absorbing sphere model for scattering changes, represented by equation (5.7), was fit simultaneously to the angularly-resolved scattering data obtained from control and NPe6-labeled EMT6 cells, the most interesting parameter to consider from the fitting algorithm was  $C_\sigma$ . We did not attempt to directly extract the refractive index of lysosomes by fitting an exact absorbing sphere Mie theory model to the data, but this parameter served as an approximation to it. In almost all measurements, we obtained a value for  $C_\sigma$  near 0.5. If we assume that the NPe6 staining brought the mean cross section,  $\langle\sigma_{\text{sca}}\rangle$ , in figure 5.6 from its non-absorbing value to its minimum value, which is

modeled by the parameter  $C_\sigma = 0.5$ , then we must conclude that the real refractive index of lysosomes in this cell line is near 1.6. Indeed, in figure 5.6, the  $n_r = 1.6$  curve is the only one that exhibits absorption-induced changes consistent with  $C_\sigma = 0.5$ .

When the absorbing sphere model was applied to angularly-resolved scattering at 633 nm from control and NPe6-loaded cells, the fitting algorithm returned parameters that were consistent with a stained lysosomal population, though the size distributions that were recovered showed some variability. From the analysis shown in figure 5.7, we were probably underestimating the contribution of NPe6-stained lysosomes at angles greater than  $60^\circ$  during fits, as this is where our approximation that the addition of absorption did not change the angular distribution of scattering for the lysosomal population is least valid. This assumption may have contributed to some minimal parameter cross-talk. Therefore, we are not proposing this study as a method to accurately size lysosomes by using an organelle-specific staining contrast agent in scattering measurements. However, the size distributions captured by these fits provide sound evidence that we are in fact observing lysosomes. To the best of our knowledge, these are the first scattering signatures from intact cells identified to come directly from lysosomes reported in the literature.

When we examined angularly-resolved light scattering measurements from cells stained with HPPH at a wavelength near its absorption maximum, we

did not see any discernable scattering changes between the HPPH-loaded and control cells. The concentrations of HPPH used in these measurements were guided by the literature [16] as well as from fluorescence microscopy that we performed to maximize the intracellular concentration while retaining selectivity to mitochondria. It is not surprising that there were no scattering changes between control and HPPH-loaded cells in light of figures 5.6 and 5.8. For indices of refraction of mitochondria cited in the literature, near 1.4, there should be no absorption-induced scattering changes. The fact that a study designed to stain mitochondria with a high extinction dye revealed no changes in the scattering provides strong evidence that the refractive index of mitochondria differs significantly from that of lysosomes.

We cannot leave this discussion without commenting on what this study implies about the mitochondrial contribution to our observed scattering signals. From the HPPH staining experiments, we conclude that the refractive index of these mitochondria is within the range reported in the literature. When we fit our absorbing-sphere model to the NPe6-stained and control cell data at 633 nm, we extracted information about a population of light scattering centers within cells,  $\ell_1$  from equation (5.7), with a mean diameter and standard deviation of 1.3 and 0.6  $\mu\text{m}$ , respectively, that scatters between 75-85 % of the light. This represents a population that is similar to that reported in Chapter 3, which had a mean diameter and standard deviation of 1.1 and 0.6  $\mu\text{m}$ , respectively. In that earlier

report, we concluded that this signal originated from a mixture of mitochondria and lysosomes. In the present study, we focused on isolating the contribution to the scattering signal from the NPe6-stained lysosomes. As mitochondria are larger organelles than lysosomes, the larger mean size extracted in the present study, 1.3 versus 1.1, is not surprising. We believe that the  $\ell_1$  population extracted in the present study represents the mitochondria and is relatively free from contamination from scattering associated with lysosomes. This lends further evidence to support previous assertions that mitochondria scatter a large majority of the light from EMT6 cells at 633 nm and that scattering measurements from these cells are very sensitive to mitochondrial morphology.

The results of this study are significant in that they are the first to effectively isolate a lysosomal population of light scattering centers within cells, as well as demonstrate a refractive index difference between two organelle populations. We also believe that the observation that staining can cause scattering changes from certain organelle populations is important in that this could inform the data analysis for other researchers studying cell morphology with light scattering. A future study that this Chapter suggests is a complete characterization of the lysosomal contribution to whole-cell scattering. NPe6, with proper irradiation, has the ability to deposit oxidative stress to lysosomes in much the same way that aminolevulinic acid-induced protoporphyrin IX was used to perturb mitochondria [7]. Since we now have an understanding of how these

staining effects can influence the scattering data, this should be relatively straightforward. As we continue to generate knowledge about how individual organelle populations contribute to whole-cell light scattering signals, light scattering measurements can fulfill their promise as an important tool for studying morphology in cell biology.

---

---

## References

1. L. T. Perelman, V. Backman, M. Wallace, G. Zonios, R. Manoharan, A. Nusrat, S. Shields, M. Seiler, C. Lima, T. Hamano, I. Itzkan, J. Van Dam, J. M. Crawford, and M. S. Feld, "Observation of periodic fine structure in reflectance from biological tissue: A new technique for measuring nuclear size distribution," *Phys. Rev. Lett.* **80**, 627-630 (1998).
2. V. Backman, R. Gurjar, K. Badizadegan, L. Itzkan, R. R. Dasari, L. T. Perelman, and M. S. Feld, "Polarized light scattering spectroscopy for quantitative measurement of epithelial cellular structures in situ," *IEEE J. Sel. Top. Quant. Elect.* **5**, 1019-1026 (1999).
3. A. Wax, C. Yang, V. Backman, K. Badizadegan, C. W. Boone, R. R. Dasari, and M. S. Feld, "Cellular organization and substructure measured using angle-resolved low-coherence interferometry," *Biophys. J.* **82**, 2256-2264 (2002).
4. N. N. Boustany, R. Drezek, and N. V. Thakor, "Calcium-induced alterations in mitochondrial morphology quantified in situ with optical scatter imaging," *Biophys. J.* **83**, 1691-1700 (2002).
5. N. N. Boustany, Y. C. Tsai, B. Pfister, W. M. Joiner, G. A. Oyler, and N. V. Thakor, "BCL-xL-dependent light scattering by apoptotic cells," *Biophys. J.* **87**, 4163-4171 (2004).
6. G. Schuele, E. Vitkin, P. Huie, C. O'Connell-Rodwell, D. Palanker, and L. T. Perelman, "Optical spectroscopy noninvasively monitors response of organelles to cellular stress," *J. Biomed. Opt.* **10**, 051404 (2005).
7. J. D. Wilson, C. E. Bigelow, D. J. Calkins, and T. H. Foster, "Light scattering from intact cells reports oxidative-stress-induced mitochondrial swelling," *Biophys. J.* **88**, 2929-2938 (2005).
8. H. Fang, M. Ollero, E. Vitkin, L. M. Kimerer, P. B. Cipolloni, M. M. Zaman, S. D. Freedman, I. J. Bigio, I. Itzkan, E. B. Hanlon, and L. T. Perelman, "Noninvasive sizing of subcellular organelles with light scattering spectroscopy," *IEEE J. Sel. Top. Quant. Elect.* **9**, 267-276 (2003).

- 
9. R. Drezek, A. Dunn, and R. Richards-Kortum, "Light scattering from cells: finite-difference time-domain simulations and goniometric measurements," *Appl. Opt.* **38**, 3651-3661 (1999).
  10. J. Beuthan, O. Minet, J. Helfmann, M. Herrig, and G. Muller, "The spatial variation of the refractive index in biological cells," *Phys. Med. Biol.* **41**, 369-382 (1996).
  11. H. Liu, B. Beauvoit, M. Kimura, and B. Chance, "Dependence of tissue optical properties on solute-induced changes in refractive index and osmolarity," *J. Biomed. Opt.* **1**, 200-211 (1996).
  12. J. R. Mourant, T. M. Johnson, S. Carpenter, A. Guerra, T. Aida, and J. P. Freyer, "Polarized angular dependent spectroscopy of epithelial cells and epithelial cell nuclei to determine the size scale of scattering structures," *J. Biomed. Opt.* **7**, 378-387 (2002).
  13. J. D. Wilson and T. H. Foster, "Mie theory interpretations of light scattering from intact cells," *Opt. Lett.* **30**, 2442-2444 (2005).
  14. J. J. Reiners, Jr., J. A. Caruso, P. Mathieu, B. Chelladurai, X. M. Yin, and D. Kessel, "Release of cytochrome c and activation of pro-caspase-9 following lysosomal photodamage involves Bid cleavage," *Cell Death Differ.* **9**, 934-944 (2002).
  15. R. K. Pandey, A. B. Sumlin, S. Constantine, M. Aoudla, W. R. Potter, D. A. Bellnier, B. W. Henderson, M. A. Rodgers, K. M. Smith, and T. J. Dougherty, "Alkyl ether analogs of chlorophyll-a derivatives: Part 1. Synthesis, photophysical properties and photodynamic efficacy," *Photochem. Photobiol.* **64**, 194-204 (1996).
  16. I. J. MacDonald, J. Morgan, D. A. Bellnier, G. M. Paszkiewicz, J. E. Whitaker, D. J. Litchfield, and T. J. Dougherty, "Subcellular localization patterns and their relationship to photodynamic activity of pyropheophorbide-a derivatives," *Photochem. Photobiol.* **70**, 789-797 (1999).
  17. C. F. Bohren and D. R. Huffman, *Absorption and Scattering of Light by Small Particles*, Wiley, New York (1998).
  18. A. Curry, G. Nusz, A. Chilkoti, and A. Wax, "Substrate effect on refractive index dependence of plasmon resonance for individual silver nanoparticles

- observed using darkfield micro-spectroscopy," *Opt. Exp.* **13**, 2668-2677 (2005).
19. E. L. Hull and T. H. Foster, "Steady-state reflectance spectroscopy in the P-3 approximation," *J. Opt. Soc. Am. A* **18**, 584-599 (2001).
  20. J. R. Lakowicz, *Principles of Fluorescence Spectroscopy*, Kluwer Academic/Plenum, 2nd ed., New York (1999).
  21. P. R. Bevington and D. K. Robinson, *Data Reduction and Error Analysis for the Physical Sciences*, 3rd ed, McGraw Hill, New York (2003).
  22. G. W. Kattawar and G. N. Plass, "Electromagnetic scattering from absorbing spheres," *Appl. Opt.* **43**, 1377-1382 (1967).
  23. Hecht E., *Optics*, Addison Wesley, San Francisco (2002).

# **Chapter 6. Characterization of the lysosomal contribution to whole-cell light scattering as quantified by photodynamic organelle ablation**

## **6.1 Introduction**

In Chapter 3 we showed that angularly resolved light scattering measurements from intact EMT6 cells are consistent with mitochondria and lysosomes being the dominant light scattering centers. The coated-sphere model of scattering attributed to mitochondrial swelling that was developed in Chapter 4, however, assumes that the lysosomal contribution to cellular light scattering is negligible. In Chapter 5, we observed a scattering contrast between cells stained with a high-extinction lysosomal-localizing dye and cells that were unstained, and through an absorbing-sphere model we extracted a size distribution and scattering contribution that we assigned to lysosomes. As that model was an approximation designed primarily to identify the refractive index of lysosomes, we need an independent set of experiments to verify that the size distributions and scattering

contributions of lysosomes identified in that Chapter are correct. The dye N-aspartyl chlorin e6 (NPe6) is a photosensitizer used in photodynamic therapy (PDT) that localizes in lysosomes [1]. It is well established that with proper irradiation of cells loaded with lysosomal-localizing photosensitizers, oxidative stress is deposited to these organelles causing lysosomal ablation [1-3]. PDT has been shown to destroy the overwhelming majority of lysosomes with a variety of lysosomal-localizing photosensitizers [2] in cell lines including EMT6 [3] and specifically using NPe6 in other cell lines [1]. In this Chapter, we find conditions under which NPe6-PDT causes lysosomal ablation and use angularly-resolved light scattering measurements from control- and lysosome-ablated-EMT6-cells to measure lysosomal particle size distributions and the lysosomal contribution to cellular light scattering.

## 6.2 Materials and methods

For fluorescence microscopy studies, EMT6 cells were grown on 25 mm round coverslips in Eagle's basal medium with 10% fetal bovine serum (complete media) at 37° C and 5% CO<sub>2</sub>. After three days, the media was removed and cells were incubated in complete media containing 50 µg/ml of NPe6 overnight in the dark. They were then co-stained with 75 nM LysoTracker Blue (Molecular Probes, Eugene, OR) for 1 h. The cells were then washed twice in Hank's Balanced Salt Solution (HBSS) and placed in a coverslip dish that accommodates 1 ml of HBSS. Fluorescence images of cells were acquired using a Nikon

Diaphot inverted microscope with filter sets appropriate for LysoTracker Blue. Cells were irradiated on the microscope stage with  $20 \text{ mW cm}^{-2}$  of light from a 662 nm diode laser at fluences ranging from  $100 \text{ mJ cm}^{-2}$  –  $50 \text{ J cm}^{-2}$ , with fluorescence images captured at various fluences spanning this range.

For angularly-resolved light scattering measurements, cells were maintained in monolayer culture in complete media. When cells reached 60-70% confluence, the media was removed, and cells were incubated overnight in complete media containing  $50 \text{ }\mu\text{g/ml}$  NPe6. The cells were then washed twice with HBSS, lifted from the plate with 0.25% trypsin, and then suspended in at least 1 part complete media per part trypsin. They were then centrifuged and re-suspended in HBSS at a concentration of approximately  $5 \times 10^6$  cells/ml. Using a goniometer described in detail in Sections 3.2 and 5.2.4, angularly-resolved light scattering measurements at 633 nm were taken on intact, control EMT6 cells and cells that had been incubated with NPe6 and irradiated with a  $20 \text{ J cm}^{-2}$  treatment at 662 nm.

### 6.3 Results and discussion

Representative fluorescence images demonstrating lysosomal ablation are shown in figure 6.1. In the pre-treatment image (A), we see a punctate pattern of fluorescence characteristic of lysosomal staining. After a  $10 \text{ J cm}^{-2}$  irradiation (B), the fluorescence pattern is more diffuse, consistent with redistribution of the LysoTracker into the cytosol. After  $20 \text{ J cm}^{-2}$  (C), the majority of the punctate

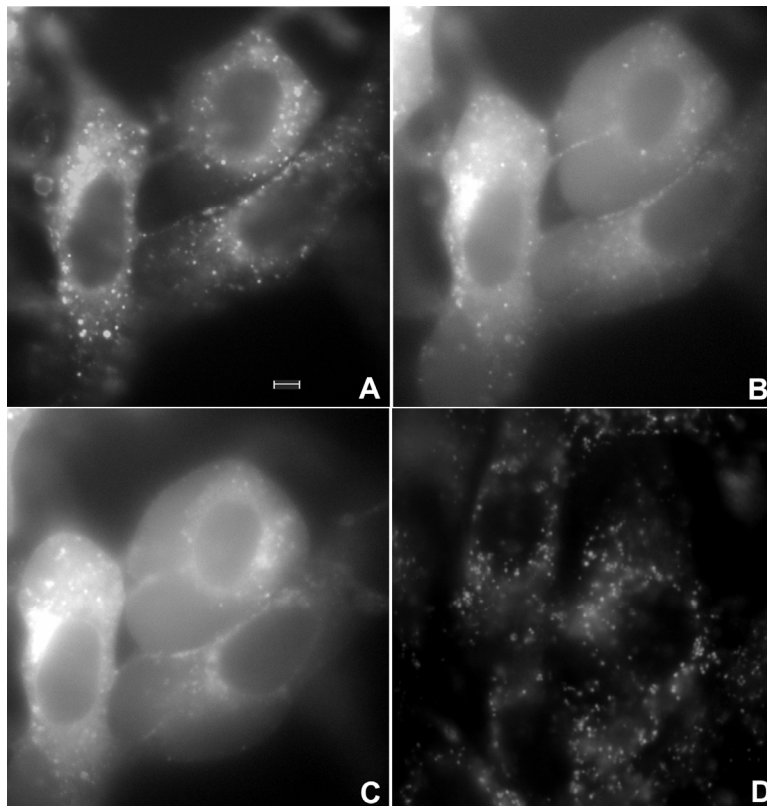


**Figure 6.1.** (A-C) Fluorescence images of EMT6 cells loaded with 50  $\mu\text{g/ml}$  NPe6, stained with 75 nM LysoTracker Blue, and imaged with a filter set appropriate for LysoTracker Blue. (A) Cells with no irradiation show a punctate pattern of fluorescence. (B) After 10  $\text{J cm}^{-2}$  of 662 nm irradiation, we see a more diffuse pattern of fluorescence, and (C) after 20  $\text{J cm}^{-2}$ , the majority of lysosomes are ablated. (D) An image of cells labeled with LysoTracker Blue only and irradiated at 662 nm (20  $\text{J cm}^{-2}$ ). The punctate pattern of fluorescence is maintained in the absence of NPe6-mediated PDT. The scale bar is 4  $\mu\text{m}$ .

foci of fluorescence have disappeared, indicating the ablation of a significant fraction of lysosomes. The fluorescence pattern did not significantly change when a  $50 \text{ J cm}^{-2}$  irradiation was delivered to the cells. Cells loaded with LysoTracker Blue in the absence of NPe6 were imaged pre- and post-irradiation with  $20 \text{ J cm}^{-2}$  at 662 nm to insure that changes in the fluorescence pattern were not due to photobleaching of the LysoTracker. The post-irradiation image is shown in figure 6.1(D).

Angularly-resolved light scattering data from control, intact cells and cells with PDT-ablated lysosomes are shown in figure 6.2. The scattering data for PDT-treated cells reveal that cells subjected to a  $20 \text{ J cm}^{-2}$  treatment scatter less light than control cells into angles greater than 15 degrees, while forward directed scattering is similar for the two cell groups. Scattering changes in this angular range are consistent with previous findings attributed to lysosomes in Chapter 5 and dramatically inconsistent with our findings following mitochondrial perturbations shown in Chapter 4. Within a Mie theory model, scattering changes in this range of angles are consistent with perturbations to particles smaller than mitochondria.

We fit our Mie theory model described in detail in Chapter 3 to both the control-cell scattering data and data from cells subjected to a  $20 \text{ J cm}^{-2}$  NPe6-PDT. Briefly, we assumed that the functional form of the particle size distribution,  $\rho$ , was a sum of log-normal distribution as

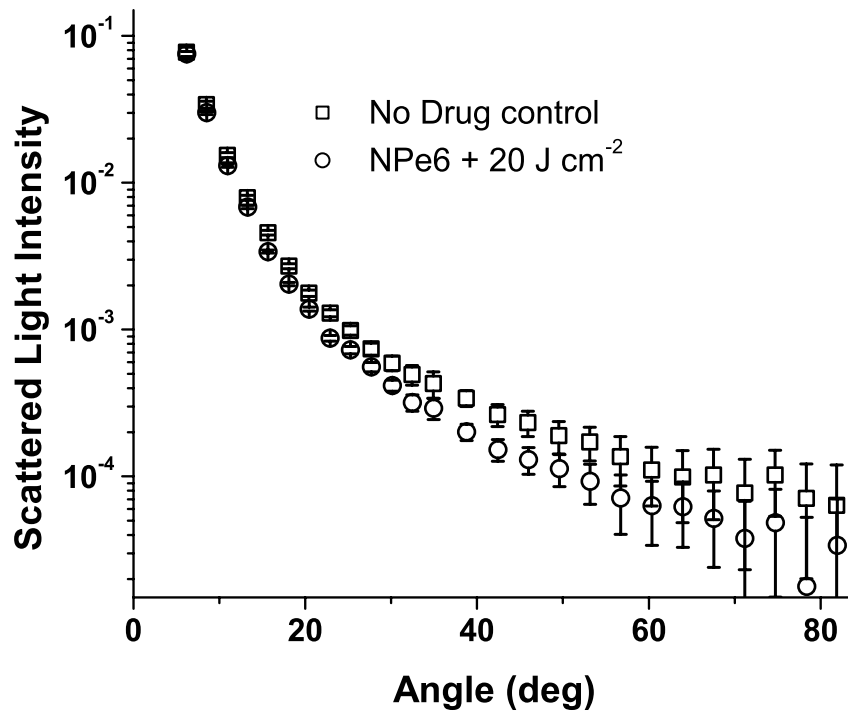


**Figure 6.2.** Angularly-resolved light scattering data from intact control EMT6 cells (squares) and cells given a 20 J cm<sup>-2</sup> NPe6-PDT treatment. These two cell populations have similar angular scattering distributions in the forward direction, while the PDT-treated group scatters less light beyond 15 degrees, characteristic of a population of light scattering centers being ablated.

$$\rho(r) = \sum_j a_j \ell_j(r) \quad (6.1)$$

where  $a_j$  are constants representing relative numbers of particles in each log-normal distribution,  $\ell_j(r)$ , that is described completely by its mean,  $\mu_j$ , and standard deviation,  $SD_j$ . Angular scattering distributions for the assumed particle size distributions are calculated from Mie theory, and the  $\mu_j$ 's,  $SD_j$ 's, and  $a_j$ 's are adjusted to minimize  $\chi^2$  using a downhill simplex routine. A notable result of these fits is that, consistent with results reported in Chapter 3, the particle size distributions returned from fits to both control and PDT-treated cells are bimodal and are incompatible with a trimodal size distribution. Representative plots of scattering-cross-section-( $\sigma$ )-weighted particle size distributions,  $\sigma\rho$ , are displayed in figure 6.3. In these curves, which represent the amount of light scattered as a function of particle diameter, it is evident that the effect of lysosomal ablation on light scattering from these cells is modest and that changes in the  $\sigma\rho$  plots are apparent for particle sizes smaller than 2  $\mu\text{m}$ . Parameters returned by these fits, the means,  $\mu$ , standard deviations,  $SD$ , and scattering contribution defined as

$$R_j = \frac{\int a_j \ell_j(r) \sigma(r) dr}{\sum_k \int a_k \ell_k(r) \sigma(r) dr}, \quad (6.2)$$

are summarized in Table 6.1.

<b>Parameter</b>	<b>20 J cm<sup>-2</sup></b>	<b>Control</b>	<b>Simultaneous</b>
Mean <sub>1</sub> (μm)	1.3	1.1	1.3
SD <sub>1</sub> (μm)	0.6	0.6	0.65
R <sub>1</sub> (%)	90	91	77
Mean <sub>2</sub> (μm)	0.12	0.14	0.14
SD <sub>2</sub> (μm)	0.08	0.07	0.08
R <sub>2</sub> (%)	10	9	9
Mean <sub>3</sub> (μm)	***	***	0.8
SD <sub>3</sub> (μm)	***	***	0.4
R <sub>3</sub> (%)	***	***	14

**Table 6.1.** Summary of parameters that were returned by fits to angularly resolved light scattering data from control and NPe6 PDT-treated cells. When the control- and PDT-treated data sets were fit individually, each returned a bimodal distribution in particle size, with the treated cells favoring slightly larger particles. When we fit the two sets simultaneously, we obtained information about a third population of ablated lysosomes.

As the fits to each individual data set do not reveal the existence of a lysosomal population of light scattering centers, we fit a model to the control-cell and PDT-treated-cell scattering data simultaneously by methods similar to that described in Section 5.2.6 to quantify the contribution of lysosomes to angularly-resolved light scattering data. The model we adopted was that intact control cells had a tri-modal size distribution of the form of equation (6.1). When cells were treated with  $20 \text{ J cm}^{-2}$  in the presence of NPe6, one of these log-normal distributions, representing the contribution from lysosomes, is completely ablated while the other two populations remain intact. Then the particle size distributions for control and lysosome-ablated cells are written as

$$\begin{aligned} \rho_{PDT} &= a_1 \ell_1 + a_2 \ell_2 \\ \rho_{control} &= \rho_{PDT} + a_3 \ell_3 \end{aligned} \quad (6.3)$$

When we fit these data sets simultaneously, we were able to recover 3 distinct populations of light scatterers. The particle distribution that we identified as lysosomes, or  $\ell_3$  in equation (6.3), is characterized by a mean size and standard deviation of  $0.8 \text{ }\mu\text{m}$  and  $0.4 \text{ }\mu\text{m}$ , respectively. Its contribution to the scattering signal,  $R$  from equation (6.2), is 14%. The most dominant light scattering population,  $\ell_1$ , with an  $R$  parameter of 77%, had a mean diameter and standard deviation of  $1.3 \text{ }\mu\text{m}$  and  $0.65 \text{ }\mu\text{m}$ , respectively. This population has size parameters very similar to those that we have attributed to mitochondria in

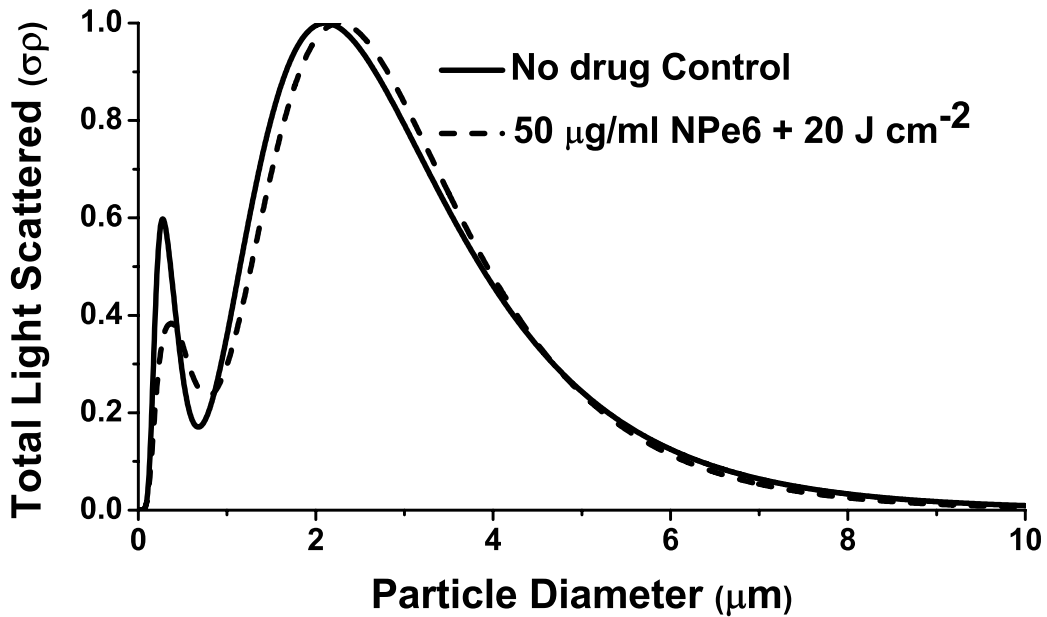


**Figure 6.3.** Plots of cross-section-weighted particle size distributions returned from fits to the angularly-resolved light scattering data from control and 20  $\text{J cm}^{-2}$  NPe6-PDT treated data. Analysis of these data shows that lysosomes are 0.5-1  $\mu\text{m}$  in size, and contribute roughly 14% of the total scattering signal at 633 nm.

Chapters 4 and 5. The third population,  $\ell_2$ , had a mean and standard deviation of 0.14  $\mu\text{m}$  and 0.08  $\mu\text{m}$ , respectively, and accounted for only 9% of the signal. These parameters are summarized in Table 6.1.

Figure 6.4 shows the log-normal particle size distributions returned by fits to control cell scattering data and distributions returned from simultaneous fits to control and PDT-treated cell data sets. The particle size distributions that we have attributed to lysosomes and mitochondria, which were obtained using equation (6.3), are shown in dots ( $\cdots$ ) and dashes (---), respectively. It is clear that these curves blend together in size. In fact, when we plot the weighted sum of these distributions, represented by open circles (ooo), it takes the form of a single log-normal distribution, which accounts for the fact that we cannot isolate mitochondrial and lysosomal light scattering contributions without some form of contrast. What is striking is that when we overlay the distribution  $\ell_1$  returned from our bi-modal fit to the control-cell data, represented by the solid black curve, it is indistinguishable from the weighted sum of the lysosomal and mitochondrial populations.

We have reported on our results using photodynamic ablation to quantify the lysosomal contribution to angularly-resolved light scattering from intact EMT6 cells. We found both the particle size distributions and the relative scattering contribution for lysosomes to be in remarkable agreement with those reported in Chapter 5. The lysosomal contribution to cellular light scattering of

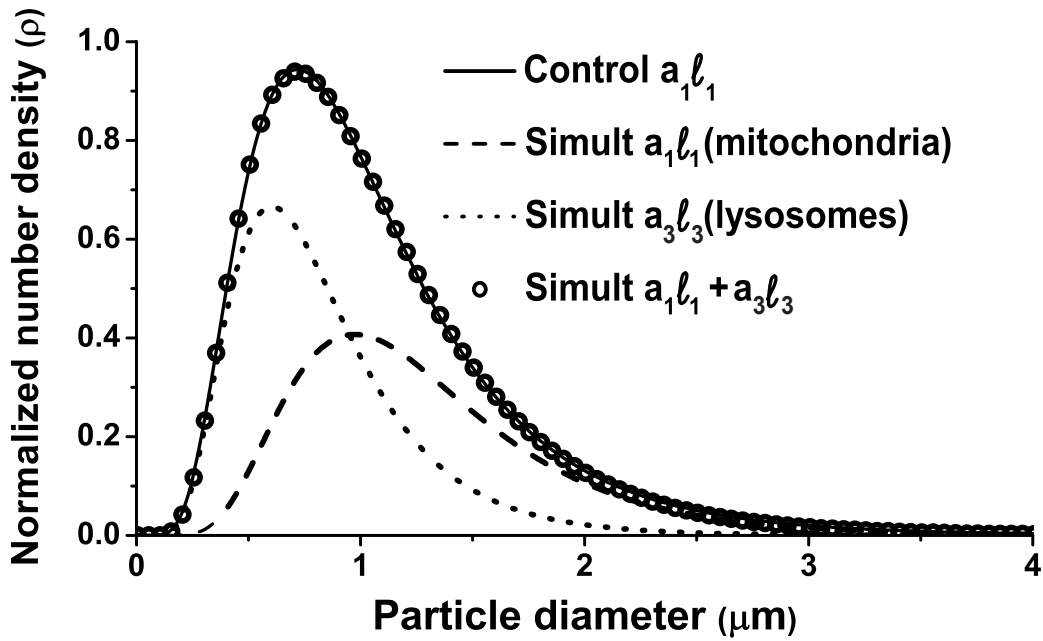


**Figure 6.4.** Particle size distributions extracted from fits to scattering data. The control distribution (solid line) refers to population 1 from the control column in Table 6.1. The simultaneous fits represent populations 1 (dash) and 3 (dot) from the simultaneous column of Table 6.1, which we attribute to mitochondria and lysosomes, respectively. The open circles (ooo) are the weighted sum of the simultaneous populations 1 and 3.

14% that we found in this study in one sense represents a lower limit, as the possibility that some lysosomes were left intact after PDT cannot rigorously be excluded. However, taken together with our previously reported estimate of 15% obtained using a completely independent method in Chapter 5 and the electron microscopy results reported in Lin et al. [2], we conclude that the overwhelming majority of lysosomes were effectively ablated by photodynamic action. This study demonstrates that angularly-resolved light scattering measurements can be used to quantify lysosomal morphology; however the light scattering measurements are significantly more sensitive to the population of light scattering centers that we identify as primarily mitochondria.

## References

1. J. J. Reiners, Jr., J. A. Caruso, P. Mathieu, B. Chelladurai, X. M. Yin, and D. Kessel, "Release of cytochrome c and activation of pro-caspase-9 following lysosomal photodamage involves Bid cleavage," *Cell Death Differ.* **9**, 934-944 (2002).
2. C. W. Lin, J. R. Shulok, S. D. Kirley, C. M. Bachelder, T. J. Flotte, M. E. Sherwood, L. Cincotta, and J. W. Foley, "Photodynamic destruction of lysosomes mediated by Nile blue photosensitizers," *Photochem. Photobiol.* **58**, 81-91 (1993).
3. I. Georgakoudi and T. H. Foster, "Effects of the subcellular redistribution of two Nile blue derivatives on photodynamic oxygen consumption," *Photochem. Photobiol.* **68**, 115-122 (1998).

## **Chapter 7. Biological implications of mitochondrial-morphology-induced light scattering changes**

### **7.1 Introduction**

In the preceding chapters we developed a framework from which to interpret light scattering from intact cells and reported on the use of various strategies of photodynamic therapy (PDT) as a biophysical tool to discern the contributions of different organelle populations to whole-cell light scattering. Organelle morphology is highly relevant to the fate of a damaged cell, with mitochondrial swelling in response to a variety of insults being particularly important [1]. There is an extensive body of literature supporting the fact that both lysosomal- and mitochondrial-targeted PDT can induce apoptosis and that mitochondria are involved in apoptotic signaling in response to photodynamic damage to each of these organelles [2,3]. In Chapter 4, we showed that light scattering is exquisitely sensitive to both the gross and fine details of mitochondrial swelling in response to mitochondrial-targeted PDT. In Chapter 6 we demonstrated that through angularly-resolved light scattering measurements it is possible to quantify the lysosomal contribution by photodynamic organelle

ablation, however scattering measurements are considerably more sensitive to mitochondrial morphology. The exquisite sensitivity of light scattering measurements to mitochondrial morphology, together with the morphology-dependent role that mitochondria play in cell death pathways raise the question of what potential role light scattering measurements can play in future biological studies. Here we report on two sets of experiments that highlight the significance of mitochondrial scattering signatures in studies of cell death biology.

## **7.2 Coated-sphere swelling parameter and cell survival in Pc 4-PDT**

### ***7.2.1 Introduction***

We first report on a study that links the coated-sphere swelling amplitude from Chapter 4 to the percent of cell survival as quantified by colony forming assays in response to PDT. In these experiments, we use the photosensitizer Pc 4, which is a promising second-generation drug that is currently in clinical trials at Case Western Reserve University. The intracellular localization of Pc 4 has been well characterized using dual-label confocal fluorescence microscopy [4] and fluorescence resonance energy transfer (FRET) [5], and these studies have shown that Pc 4 is localized predominately in the mitochondria. Pc 4 is also a strong inducer of apoptosis; several articles have demonstrated that the antiapoptotic proteins Bcl-2 and Bcl-xL are among the primary targets of Pc 4-PDT [6-8]. Lam et al. [2] demonstrated a variety of mitochondrial responses to Pc 4-PDT in

vitro, including mitochondrial membrane depolarization, changes in permeability, mitochondrial swelling, and the release of cytochrome c leading to apoptotic death. Consistent with these findings, we observed through angular resolved light scattering measurements a fluence-dependent mitochondrial swelling during Pc 4-PDT. In this study we show that the changes in the amplitude of mitochondrial swelling reported by light scattering and that of the loss of cell survival occur over the same range of fluences.

## **7.2.2 Materials and methods**

### **7.2.2.1 Cell culture and Pc 4-PDT protocols**

EMT6 cells were maintained in monolayer culture in Eagle's basal medium (BME) with 10% fetal bovine serum (complete media) at 37°C and 5% CO<sub>2</sub> until they reached the desired confluence, which was approximately 90% for clonogenic assays and 60-80% for scattering experiments. For scattering measurements, the cells were first lifted from the culture dishes using 0.25% trypsin, then centrifuged to a pellet, and washed in Hanks' Balanced Salt Solution (HBSS). Irradiations were performed on cells suspended in HBSS at a concentration of 10<sup>8</sup> cells/ml. Scattering measurements were performed on cells suspended in HBSS diluted to a concentration of 10<sup>5</sup> cells/ml.

The photosensitizer Pc 4 was synthesized according to methods reported by Anula *et al.* [9]. A 0.5 mM stock solution was prepared by dissolving dry Pc 4 in *N,N'*-dimethylformamide (DMF) and stored at 4°C. The stock was diluted to

a working concentration of 250 nM in complete media, and cells were incubated for 24 h in the dark. PDT irradiation was performed on Pc 4-sensitized cells using 667 nm laser light from a diode laser (Power Technology Inc., Little Rock, AR), the output of which was coupled into a GRIN-lens-terminated multimode fiber (OZ Optics, Ottawa, ON, Canada). Cells were exposed to the prescribed fluences delivered at an irradiance of  $2.5 \text{ mW cm}^{-2}$ .

### **7.2.2.2 Light scattering measurements and models**

Angularly resolved light scattering measurements were made using instrumentation and methods described in Chapter 3. Scattering measurements were taken from cells given drug and a prescribed fluence as well as from unirradiated cells. The Mie theory model and coated-sphere mitochondrial swelling model was fit to the control and Pc 4-PDT treated cell scattering data, respectively, as described in Chapters 3 and 4.

### **7.2.2.3 Clonogenic cell survival assay**

After incubation with 250 nM Pc 4 overnight, the cells were washed with HBSS twice and harvested by trypsinization. They were diluted at least 1:1 in complete media and then centrifuged to a pellet. To obtain approximately 50-100 colonies after PDT, the number of cells counted by hemacytometer (Hausser Scientific, Horsham, PA) was adjusted for each fluence and seeded into 100-mm-diameter tissue culture dishes. In order to minimize the leaching of Pc 4 from the

sensitized cells, they were incubated in serum free BME during the irradiation period. Each dish was exposed to a prescribed fluence at  $2.5 \text{ mW cm}^{-2}$ . After the irradiation, additional BME with serum was added to the dishes such that the percentage of serum was maintained at 10%. After 7-8 days, colonies were stained with 0.005% crystal violet in water and counted visually. The percent clonogenic survival of the Pc 4-PDT-treated cells is reported as the ratio of the plating efficiency of the treated cells to that of cells incubated with 250 nM Pc 4 but not irradiated. The plating efficiencies of the completely untreated cells (no drug, no light) and the Pc 4-sensitized but not irradiated cells were approximately 90% and 81%, respectively.

A radiobiological linear-quadratic model was adopted to describe the cell survival curve [10]. The model is expressed,

$$Survival = e^{-\alpha F - \beta F^2}, \quad (7.1)$$

where  $F$  is fluence, and  $\alpha$  and  $\beta$  are fitting parameters.

## 7.2.3 Results

### 7.2.3.1 Scattering results

We observed Pc 4-PDT- induced changes in the angular distribution of scattered light that were both fluence- and time-dependent. Representative angularly-resolved light scattering data sets are shown in figure 7.1 for treatments of  $0.15 \text{ cm}^{-2}$  at the 1 h post-irradiation time point (a) and  $0.6 \text{ J cm}^{-2}$  immediately

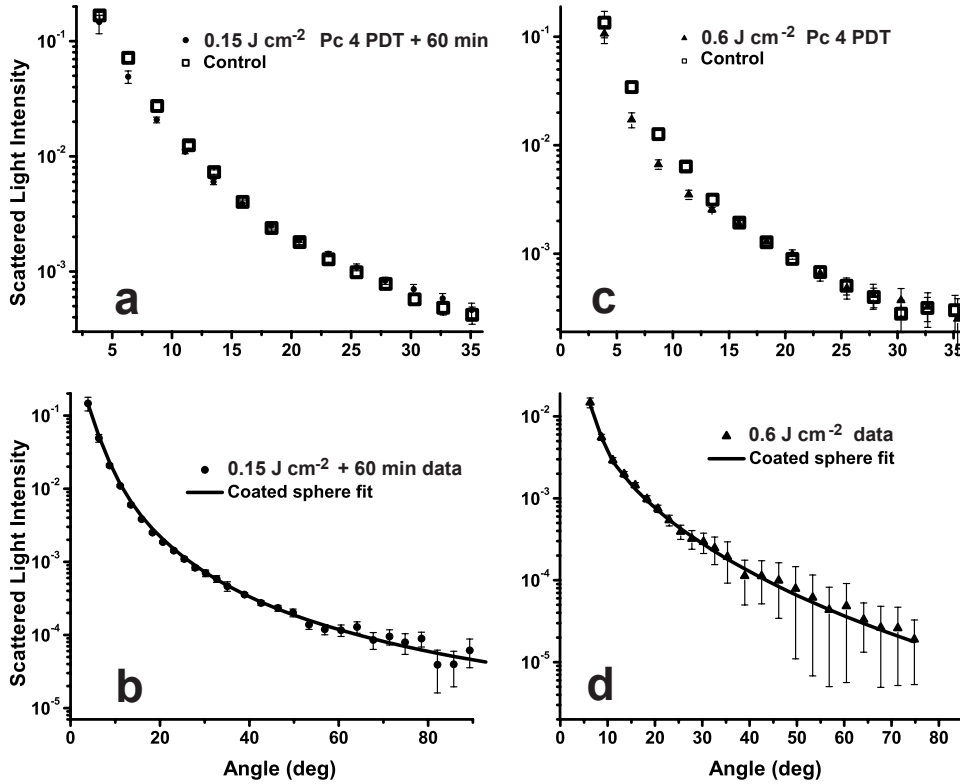


**Figure 7.1.** Angularly resolved light scattering data and coated sphere model fits to data from 250 nM Pc 4-PDT-treated EMT6 cells in suspension. Panels (a) and (b) show the scattering changes for 0.15 J cm<sup>-2</sup> Pc 4-PDT-treated cells relative to control and the coated sphere fit to the data from the PDT-treated cells, respectively. Panels (c) and (d) depict the same comparisons for the case of 0.6 J cm<sup>-2</sup> Pc 4 PDT.

after irradiation (c) relative to control. The coated sphere Mie theory model for mitochondrial swelling, described in Chapter 4, represents the data well in both cases, as shown in the lower panels (b, d) of figure 7.1.

A summary plot of the swelling parameter,  $\alpha$  from equation (4.1), returned from the coated-sphere model fits is shown in figure 7.2. The vertical axis is the fitting parameter, and the horizontal axis is time post irradiation. For cells irradiated with  $0.15 \text{ J cm}^{-2}$ , there is initially no change in the angular distribution of scattered light. At the 30 min time point, our model shows a 2.3% swelling that grows to 4.3% at 1 h. For fluences of 0.3 and  $0.6 \text{ J cm}^{-2}$ , we see immediate swelling of 8% and 13%, respectively, which does not change at 30 and 60 minutes after irradiation.

### 7.2.3.2 Clonogenic cell survival results

Figure 7.3 shows the measured clonogenic survival of Pc 4-PDT-treated EMT6 cells in response to the treatment conditions described above. Each data point is a mean of at least three independent experiments. All of the data points are normalized to the clonogenic survival measured in cells subjected to 250 nM Pc 4 overnight but not irradiated. To quantify the EMT6 cell surviving fraction vs. fluence, equation (7.1) was fit to these data. The values of the fitting parameters,  $\alpha$  and  $\beta$ , are 1.8 and 77.5, respectively. We obtain approximately 76%, 17%, 2.3% and 0.06% cell survival in response to fluences of 0.05, 0.15, 0.2 and  $0.3 \text{ J cm}^{-2}$ , respectively.

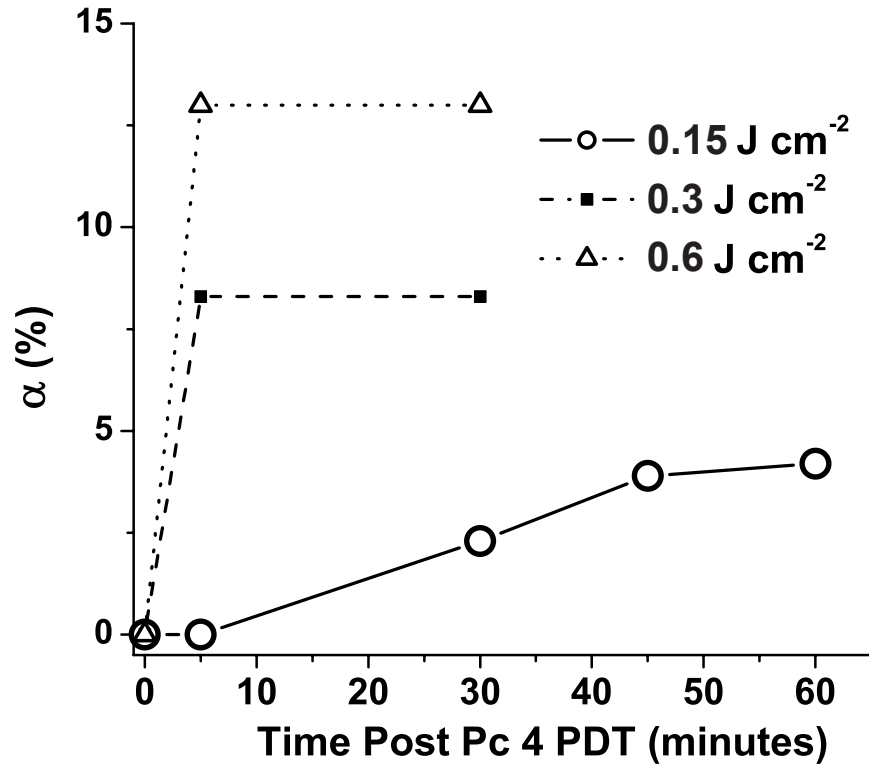


**Figure 7.2.** Time course of the swelling parameter  $\alpha$  from equation (4.1) for various fluences of 250 nM Pc 4-PDT. For the 0.3 and 0.6  $\text{J cm}^{-2}$  cases, immediate mitochondrial swelling is reported by scattering with magnitudes of 8% and 13%, respectively. For the case of the 0.15  $\text{J cm}^{-2}$  treatment, there is minimal initial swelling. Within 1 h swelling increases to approximately 4%.

### **7.2.4 Discussion**

When we compare figures 7.2 and 7.3, we can see that both the swelling parameter,  $\alpha$ , and the efficacy of cell killing increases with increased light dose. In the case of  $0.15 \text{ J cm}^{-2}$  Pc 4-PDT treatment, which corresponded to 17% cell survival, we saw no immediate scattering changes, however we observed increasing mitochondrial swelling beginning at 30 minutes and maximizing over the course of an hour. This result is very intriguing in light of the data from A431 human epidermoid carcinoma cells in response to  $0.15 \text{ J cm}^{-2}$  Pc 4 PDT presented in Lam et al. [2]. They observed cytochrome c release from the mitochondria beginning at the 30 minute time point post-irradiation, and maximizing by 60 minutes. This similarity in time courses motivated us to examine scattering in cell death in another model system in Section 7.3.

For irradiations such that we observed an immediate scattering change,  $0.3 \text{ J cm}^{-2}$ , the surviving fraction of cells had fallen to 0.06 %. This is very encouraging, and suggests the further development of a scattering-based assay for very early reporters of cell death both in vitro and possibly in vivo. Not only is scattering a much earlier reporter of cell death than colony forming assays (minutes versus weeks), but the measurement has a greater dynamic range. For treatments of  $0.6 \text{ J cm}^{-2}$ , we cannot quantify the surviving fraction with the clonogenic assay, however we can readily tell the difference between scattering changes induced by  $0.3$  and  $0.6 \text{ J cm}^{-2}$  Pc 4 PDT.

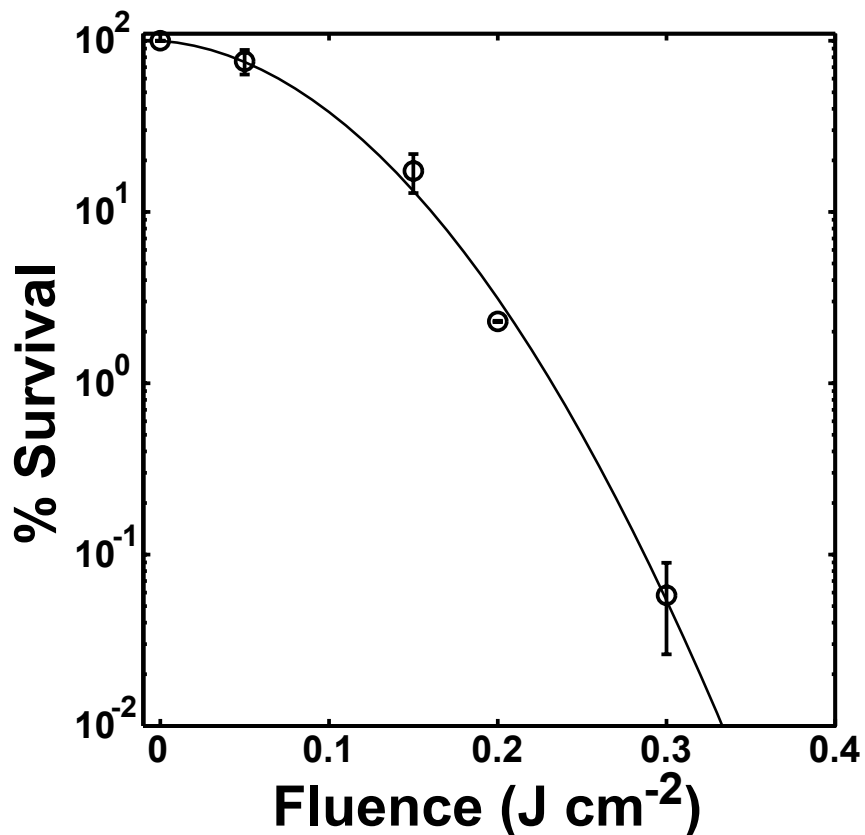


**Figure 7.3.** Clonogenic survival of EMT6 cells sensitized with 250 nM Pc 4 for 24 h and subjected to fluences of 0.05, 0.15, 0.2 and 0.3  $\text{J cm}^{-2}$ . These treatment conditions resulted in surviving fractions of approximately 76, 17, 2.3 and 0.06%, respectively. The number of colonies for each dish was 50 - 110 for the 0 - 0.2  $\text{J cm}^{-2}$  cases and 10-70 for the 0.3  $\text{J cm}^{-2}$  case. The solid line is the best fit of equation (7.1) to the data.

## **7.3 Lysosome-damage-induced mitochondrial scattering changes coincide with release of cytochrome c**

### ***7.3.1 Introduction***

During apoptosis, mitochondria release cytochrome c from their membranes into the cytosol, which initiates downstream signaling. For mitochondria-targeting PDT, the release of cytochrome c has been shown to be rapid and accompanied by mitochondrial depolarization and swelling [2]. For lysosomal sensitizers such as N-aspartyl chlorin e6 (NPe6), cytochrome c release has been shown to be a delayed effect [3]. The mechanism for cytochrome c release from the mitochondria following lysosomal PDT has not yet been proven, however Reiners et al. suggest that lysosomal enzymes are released and cleave/activate the pro-apoptotic Bcl-2 protein Bid [3].

Regardless of the pathway by which lysosomal PDT insults lead to the release of cytochrome c from the mitochondria, NPe6-PDT provides an excellent model system to study mitochondrial light scattering signatures in the context of cell death pathways. In this Section, we report on measurements of the time course of angularly-resolved light scattering changes and changes in the cellular distribution of cytochrome c in response to NPe6 PDT. Using experimental and theoretical models developed in previous chapters, we are able to measure

mitochondrial swelling with light scattering, while relating the time course of this swelling to the release of cytochrome c from the mitochondria into the cytosol.

### **7.3.2 Materials and methods**

#### **7.3.2.1 Cell culture and NPe6-PDT protocol**

EMT6 cells were maintained in monolayer culture in Eagles Basal Medium supplemented with 10% fetal bovine serum at 37° C and 5% CO<sub>2</sub>. Cells were loaded with 50 µg/ml NPe6 in complete media overnight in the dark. Cells were then washed with Hanks' Balanced Salt Solution (HBSS), harvested with 0.25% trypsin, and suspended in at least one part media per part trypsin. They were then spun down and resuspended in HBSS at a concentration of 10<sup>8</sup> cells/ml. Cells were irradiated with light from a 662 nm diode laser at 20 mW cm<sup>-2</sup> for a total treatment of either 0.5 or 1 J cm<sup>-2</sup>.

#### **7.3.2.2 Light scattering measurements and modeling**

Angularly resolved light scattering measurements were taken using 633 nm light and the goniometer setup described in Chapter 3. We acquired measurements of cells that were loaded with NPe6 and not irradiated and of cells that were irradiated with 0.5 or 1 J cm<sup>-2</sup> sampled at 15 minute intervals up to 75 minutes post-treatment.

Guided by the electron microscopy of Lin et al. [11] as well as by the details of the scattering data, we fit the homogenous-sphere swelling model

described in Chapter 4 to the scattering data from NPe6 drug control and NPe6-PDT-treated cells. This requires fitting the Mie theory model described in Chapter 3, which returns the mean diameters, standard deviations, and amplitudes of a bimodal log-normal particle size distribution, to the NPe6 drug control cell scattering data. As shown in Chapters 4, 5 and 6, one of these particle size distributions is composed primarily of mitochondria. Following irradiation, we allow these mitochondria to swell by the same percentage as  $r \rightarrow \alpha r$ , where  $r$  is the particle radius and  $\alpha$  is the swelling parameter. In this model, we further assume that swelling occurs by means of cytosol entering the mitochondria, and as these mitochondria swell, their index of refraction, which has an initial value of 1.4, is progressively diluted by the entering cytosol, which has an index of 1.38 as shown in equation (4.3).

### 7.3.2.2 Cytochrome c release assay

To assess the release of cytochrome c from the mitochondria, we adopted an imaging based method similar to that of Lam et al. [2]. Cells grown on coverslips were loaded with NPe6 as described above and irradiated at 662 nm with  $1 \text{ J cm}^{-2}$ . At 30 minute intervals post-irradiation as well as for unirradiated coverslips, cells were washed in phosphate buffered saline (PBS) and fixed in 4% formaldehyde for 15 minutes at room temperature. They were then washed twice with PBS and permeablized for 10 minutes in an immunofluorescence buffer (IFB) consisting of PBS with 1% bovine serum albumin (BSA) and 0.1% Tween

20. They were then incubated with IFB containing a FITC-conjugated anti-cytochrome c antibody (clone 6H2.B4 catalog # 612304, BioLegend, San Diego, California) at a 1:1000 dilution. Cells were then washed twice with IFB to remove any unbound antibody. Prior to imaging, the coverslips were mounted in an antifade medium (ProLong Gold, Molecular Probes, Eugene, Oregon). Cells were imaged under 20x or 60x using a Nikon Diaphot inverted fluorescence microscope and an appropriate filter set. At least 5 fields of view were captured for every coverslip, with 2 coverslips per time point, and the experiment was repeated four times on different days. Each cell was scored as having either a punctate, mitochondrial fluorescence pattern or a diffuse, whole-cell pattern of fluorescence.

### **7.3.3 Results**

#### **7.3.3.1 Scattering results**

The results of angularly resolved light scattering measurements are displayed in figure 7.4. The first three panels (A-C) of figure 7.4 represent angular scattering distributions from NPe6-PDT-treated cells compared to those from cells incubated with NPe6 without irradiation. One hour after treatment with  $1 \text{ J cm}^{-2}$  (A), the angular scattering distribution is significantly different than control, with  $p < 0.01$  as quantified by the  $\chi^2$  test [12]. These scattering changes are not present at earlier time points, with representative data from cells 30

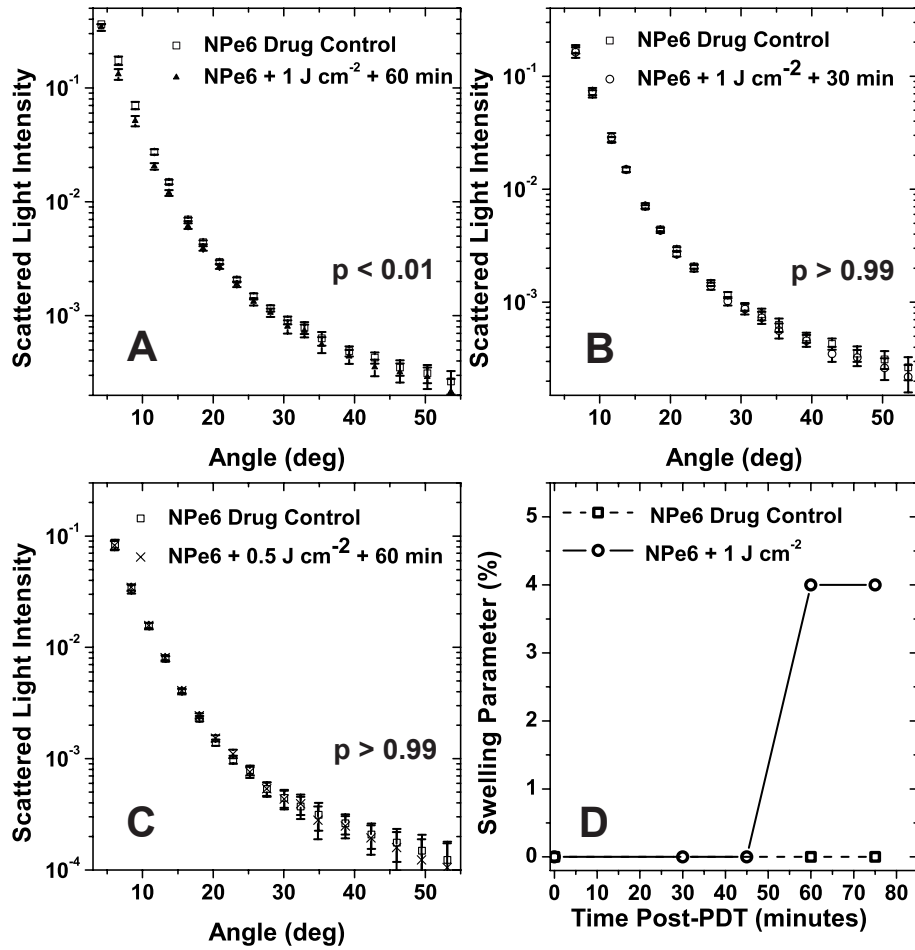


**Figure 7.4.** Angularly-resolved light scattering data. (A-C) Representative scattering data from intact cells sensitized with NPe6 (NPe6 Drug Control) versus cells sensitized and irradiated with either 0.5 or 1 J cm<sup>-2</sup> at two time points. P values as quantified by the  $\chi^2$  test [10] show that scattering from cells 1h after 1 J cm<sup>-2</sup> was significantly different from control. (D) A representative time course in the mitochondrial swelling parameter,  $\alpha$ , for NPe6 control and 1 J cm<sup>-2</sup> NPe6-PDT-treated cells.

minutes post-irradiation shown in panel (B). In the third panel (C), we display angularly resolved light scattering data from cells subjected to  $0.5 \text{ J cm}^{-2}$  compared to NPe6 control, which serves as a double control for both the fluence- and time-dependence of these scattering changes. Under these conditions, we observe no changes to angularly-resolved scattering between treated and control cells. In none of our scattering data do we observe changes for scattering angles greater than 30 degrees, the angular range that these measurements were shown in Chapter 6 to be sensitive to lysosomal ablation in response to  $20 \text{ J cm}^{-2}$  NPe6-PDT, leading us to conclude that these scattering changes are not the result of lysosomal morphology changes.

The scattering changes observed at the 1 h time point between the NPe6 control cells and cells given  $1 \text{ J cm}^{-2}$  occur in the forward angles, similar to the mitochondrial-swelling-induced scattering changes described in Chapter 4. However, guided by both electron microscopy studies reported in Lin et al. [11], which showed homogeneous mitochondrial swelling in response to lysosome-targeted PDT, and the details of the scattering data, we fit a homogenous-sphere model for mitochondrial swelling described above. The last panel of figure 7.4 (D) shows a representative time course in the swelling parameter,  $\alpha$ , for cells treated with  $1 \text{ J cm}^{-2}$  and for NPe6 drug control cells. For the drug control, our model predicts that there is no mitochondrial swelling throughout the 75 minute observation period. For cells treated with  $1 \text{ J cm}^{-2}$ , we see no swelling before the

60 minute time point. At one hour post-irradiation, our model predicts a 4% increase in mitochondrial radius.

### 7.3.3.2 Cytochrome c assay results

Representative fluorescence images of the FITC-anti-cytochrome-c in EMT6 cells are shown in figure 7.5 (A-F). Figure 7.5 (A) and (B) show representative fields of cells immediately pre- and post-irradiation. These fields show cells with punctate, mitochondrial patterns of fluorescence. At the 30 minute time point (C), the majority of cells are still displaying this mitochondrial fluorescence pattern. At 60-120 minutes (D-F), we see that the fluorescence pattern is more diffuse, indicative of cytochrome c having left the mitochondria. The bottom panel of figure 7.5 (G) displays the summary time course of cytochrome c release from NPe6-sensitized cells in response to  $1 \text{ J cm}^{-2}$ . Immediately following irradiation, we found that 3% of cells had released cytochrome c. At the 30 minute time point,  $22 \pm 13\%$  of cells had a staining pattern indicative of release, and by the 1 h time point this number had increased to  $63 \pm 18\%$ . At 2 hours nearly all of the cells showed a diffuse fluorescence pattern, with  $88 \pm 9\%$  of cells scored as having released their cytochrome c from the mitochondria.

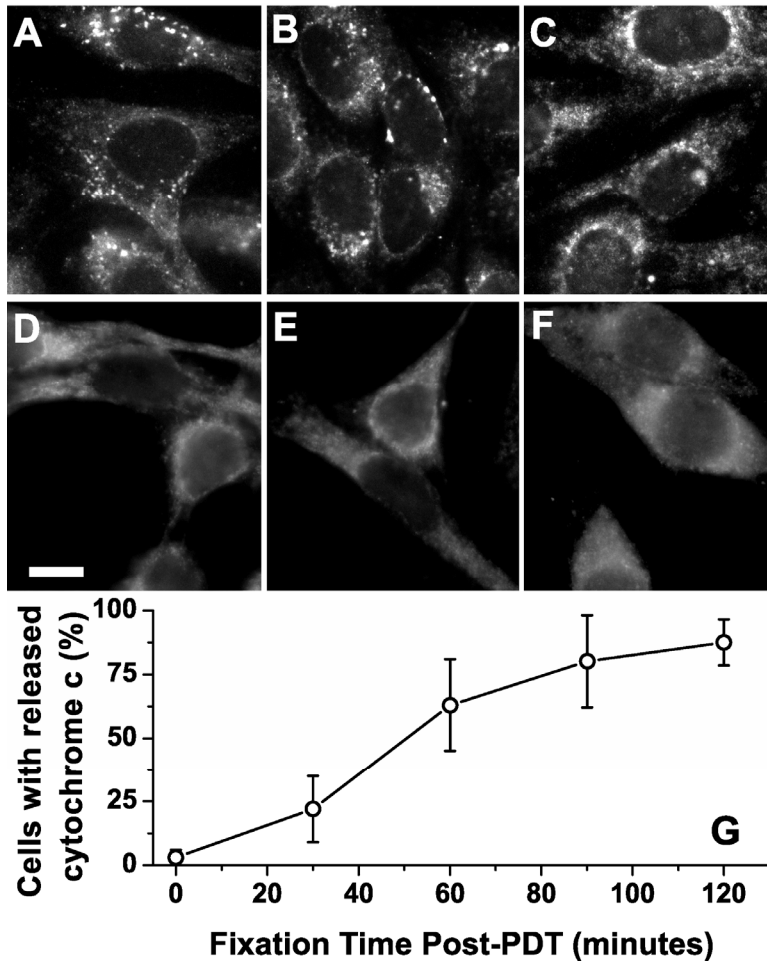


**Figure 7.5.** Results from cytochrome c imaging assay. (A-F) Representative microscopic fields of FITC-labeled anti-cytochrome c at various time points captured at 60x (scale bar = 10  $\mu\text{m}$ ). These time points represent pre-irradiation (A), and 0 (B), 30 (C), 60 (D) 90 (E), and 120 (F) minutes post-irradiation at 1 J  $\text{cm}^{-2}$ . (G) The summary time course of cytochrome c release as quantified by this assay.

### 7.3.4 Discussion

When the time courses of the swelling parameter reported in figure 7.4 (D) and of cytochrome c release shown in figure 7.5 (F) are compared, we see that the 60 minute time point is significant for both curves. Pertaining to the cytochrome c assay, this is the time at which both the largest increase in cytochrome c release occurs as well as where the condition that greater than 50% of cells have released their cytochrome is met. In regards to the scattering time course, 60 minutes is the time point at which we detect a scattering change in response to  $1 \text{ J cm}^{-2}$ . At 30 minutes, although 22% of cells had released their cytochrome, we did not detect any changes in scattering. A plausible explanation for this observation is that we are measuring scattering over an ensemble of cells but cytochrome c release on a cell-by-cell basis. To properly address this issue, one would need to adopt a method that is capable of measuring scattering changes and cytochrome release on a per-cell basis.

## 7.4 Summary

The data presented in these studies stresses the potentially significant role that light scattering has to play as a tool in cell biology. In Section 7.2, we showed that for the mitochondrial sensitizer Pc 4, the coated-sphere swelling parameter maps into clonogenic cell survival, and that the useful dynamic range of the scattering measurements is larger than that of the traditional colony forming

assay. In section 7.3, we reported that scattering changes attributed to the mitochondria coincide with the release of cytochrome c from the mitochondria.

For the study in section 7.3, we must emphasize that we used light scattering to find treatment conditions and time points under which lysosomal-PDT would cause cytochrome release, and not the other way around. Second, we detected very modest changes in mitochondrial radius, a 4% overall swelling, which provided a robust light scattering signature of apoptotic signaling. Last, our scattering data from the two studies in this chapter reported specific mitochondrial-morphological change, homogenous- versus coated-sphere swelling, in response to lysosomal versus direct mitochondrial photodynamic damage, stressing that forward angle scattering is exquisitely sensitive to the fine details of mitochondrial morphology.

## References

1. D. R. Green and J. C. Reed, "Mitochondria and apoptosis," *Science* **281**, 1309-1312 (1998).
2. M. Lam, N. L. Oleinick, and A. L. Nieminen, "Photodynamic therapy-induced apoptosis in epidermoid carcinoma cells. Reactive oxygen species and mitochondrial inner membrane permeabilization," *J. Biol. Chem.* **276**, 47379-47386 (2001).
3. J. J. Reiners, Jr., J. A. Caruso, P. Mathieu, B. Chelladurai, X. M. Yin, and D. Kessel, "Release of cytochrome c and activation of pro-caspase-9 following lysosomal photodamage involves Bid cleavage," *Cell Death Differ.* **9**, 934-944 (2002).
4. N. S. Trivedi, H. W. Wang, A. L. Nieminen, N. L. Oleinick, and J. A. Izatt, "Quantitative analysis of Pc 4 localization in mouse lymphoma (LY-R) cells via double-label confocal fluorescence microscopy," *Photochem. Photobiol.* **71**, 634-639 (2000).
5. R. L. Morris, K. Azizuddin, M. Lam, J. Berlin, A. L. Nieminen, M. E. Kenney, A. C. Samia, C. Burda, and N. L. Oleinick, "Fluorescence resonance energy transfer reveals a binding site of a photosensitizer for photodynamic therapy," *Cancer Res.* **63**, 5194-5197 (2003).
6. L. Y. Xue, S. M. Chiu, and N. L. Oleinick, "Photochemical destruction of the Bcl-2 oncoprotein during photodynamic therapy with the phthalocyanine photosensitizer Pc 4," *Oncogene* **20**, 3420-3427 (2001).
7. L. Y. Xue, S. M. Chiu, A. Fiebig, D. W. Andrews, and N. L. Oleinick, "Photodamage to multiple Bcl-xL isoforms by photodynamic therapy with the phthalocyanine photosensitizer Pc 4," *Oncogene* **22**, 9197-9204 (2003).
8. J. Usuda, S. M. Chiu, E. S. Murphy, M. Lam, A. L. Nieminen, and N. L. Oleinick, "Domain-dependent photodamage to Bcl-2. A membrane anchorage region is needed to form the target of phthalocyanine photosensitization," *J. Biol. Chem.* **278**, 2021-2029 (2003).

9. H. M. Anula, J. C. Berlin, H. Wu, Y. S. Li, X. Peng, M. E. Kenney, and M. A. Rodgers, "Synthesis and photophysical properties of silicon phthalocyanines with axial siloxy ligands bearing alkylamine termini," *J. Phys. Chem. A Mol. Spectrosc. Kinet. Environ. Gen. Theory.* **110**, 5215-5223 (2006).
10. B. J. Hall, *Radiobiology for the radiologist*, (J.B. Lippincott Company, Philadelphia, PA, 1994).
11. C. W. Lin, J. R. Shulok, S. D. Kirley, C. M. Bachelder, T. J. Flotte, M. E. Sherwood, L. Cincotta, and J. W. Foley, "Photodynamic destruction of lysosomes mediated by Nile blue photosensitizers," *Photochem. Photobiol.* **58**, 81-91 (1993).
12. P. R. Bevington, *Data Reduction and Error Analysis for the Physical Sciences*, (McGraw-Hill, New York, 1969).

# **Chapter 8. An inverted microscope enabling multi-modality imaging, angle-resolved scattering and scattering spectroscopy**

## **8.1 Introduction**

In Chapters 2 and 3, we reported that measurements of light scattered into forward angles from non-spherical particles can be modeled with Mie theory and then developed a Mie-theory-based analysis through which light scattering signals from a broad size distribution of particles can be understood. We went on in Chapters 4 through 6 to report the results of several experiments that identified the specific contributions of the mitochondria and lysosomes to whole-cell light scattering. In Chapter 7, we showed that scattering measurements of photodynamic therapy (PDT)-induced mitochondrial morphology changes are predictive of both cell survival and of cytochrome c release from the mitochondria. Taken as a whole, the preceding chapters demonstrate that light scattering has a large potential role to play in future studies of cell death pathways, which is an area of great interest in modern biology.

---

Epithelial cells, where the great majority of cancers form, are cultured in the laboratory as adherent monolayers. It is therefore important to adapt scattering measurements to this condition, which necessitates the development of scattering microscopes. Several designs have been published recently, many of which are based on measurements of backscattered light [1,2]. In this Chapter, we report the design, construction, and initial characterization of a multifunctional scattering and fluorescence microscope that exploits an angle-resolved forward-scattering geometry and significantly extends the capabilities of forward-scattering Fourier-optics-based scattering microscopes that have been described in the literature [3,4]. Specifically, the design accommodates brightfield, Fourier-filtered darkfield, direct imaging of the Fourier plane, angle-resolved scattering, and white-light scattering spectroscopy from the same field of view while preserving a fluorescence imaging channel. The work presented in this Chapter was done in collaboration with William J. Cottrell, and his contribution is gratefully acknowledged.

## 8.2 Fourier plane in an imaging system

The instrument design is centered on a series of image- and Fourier-plane relays. In a generic optical imaging system there is a plane whose spatial amplitude and phase distribution is the Fourier transform of the object plane [5].

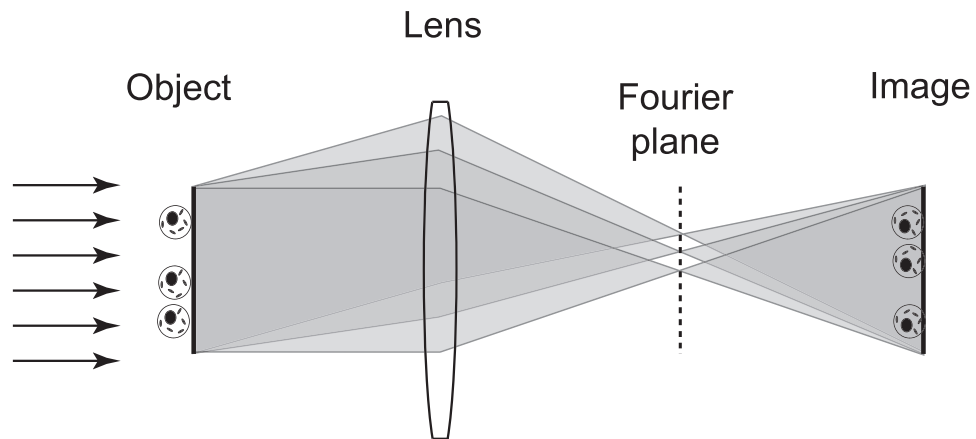


**Figure 8.1.** A schematic of a single-lens imaging system. Here we have labeled the Fourier plane. This is not only a Fourier transform of the image, but is the plane in which all light diffracted or scattered from the object at a given polar angle from the optical axis and collected within the NA of the system maps to an annulus. In a multi-lens system, the Fourier plane is in the plane in which the light source is imaged.

---

This is also the plane in which all light diffracted or scattered from the object at a given polar angle from the optical axis and collected within the NA of the system maps to an annulus. A schematic of a single-lens imaging system with the planes labeled is shown in figure 8.1. In such a one-lens system the Fourier plane is located at the rear focal plane of the lens. In a multi lens optical system such as a microscope, the Fourier transform resides in the plane in which the source is imaged.

### 8.3 Instrument design and construction

A Nikon Diaphot inverted microscope serves as the platform for the instrument design, which is shown in figure 8.2. A fiber-based collimated illumination system replaces the incandescent lamp and is attached to the condenser mount of the microscope with a custom-machined dovetail housing and a 1-inch lens tube assembly. For monochromatic illumination, the lens tube assembly includes an FC-terminated single-mode fiber that is coupled to one of several laser sources and connected to the lens tube via an FC chuck. The fiber output is collimated with a 5x, 0.12 NA microscope objective mounted in the tube. For white-light illumination, we use a similar assembly with an SMA-terminated 200  $\mu\text{m}$  core multimode fiber coupled to a tungsten halogen source (Avantes, Avalight HAL-S, Broomfield, CO). The angular divergences of the

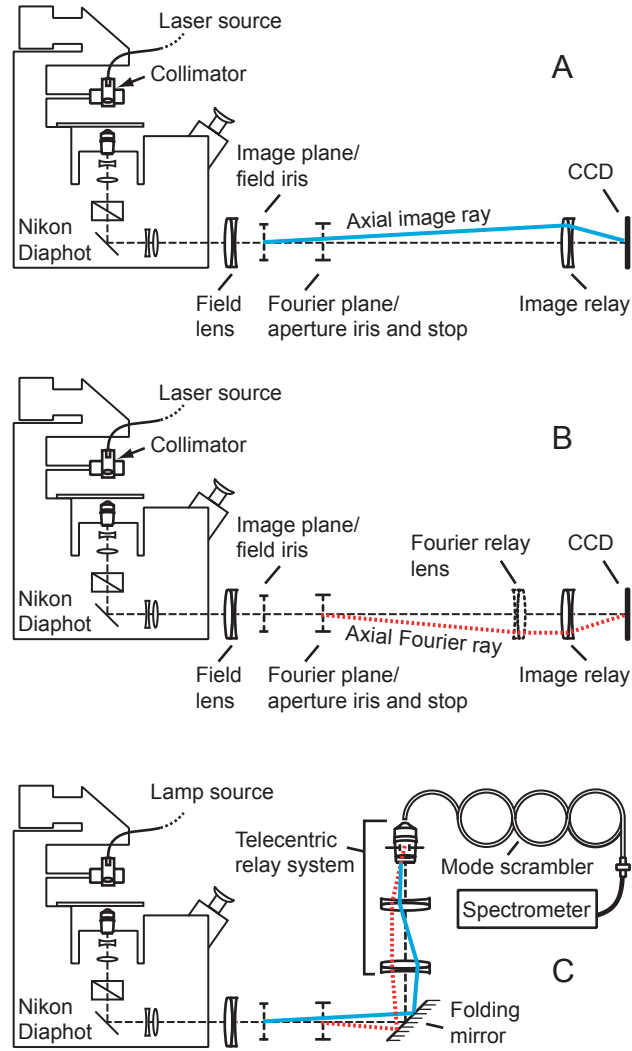


**Figure 8.2.** Schematic diagram of our system in imaging mode (A), in Fourier plane imaging and angle-resolved scattering mode (B), and in scattering spectroscopic acquisition mode.

---

monochromatic and white light beams are less than 1 and 3.5 mrad, respectively. The output beam is approximately 5 mm in diameter, thereby overfilling the sample field and maintaining a relatively flat illumination beam profile. Forward-scattered light from the sample plane is collected within the aperture of the objective and is imaged to the 35 mm camera port on the front of the microscope.

In imaging mode, a 200 mm focal length lens (Thorlabs, AC508-200-A1, Newton, NJ) is used to image the rear focal plane of the objective outside the microscope and together with a 100 mm lens (Edmund Optics, NT45-180, Barrington, NJ) forms an image relay with a magnification of approximately 0.15x onto a thermoelectrically (TE)-cooled CCD (Diagnostic Instruments, Inc., 9.0 Monochrome-6, Sterling Heights, MI). A 1.5 inch field iris in the intermediate image plane is used in conjunction with the translating microscope stage to discriminate regions of interest within the object field. A mask positioned on a kinematic mount in the Fourier plane of the objective allows control over the angular content of the detected light. This mask consists of a calibrated iris (Thorlabs, SM1D12C) and a central obscuration constructed by depositing a metallic layer on the center of a microscope cover glass. The central obscuration serves to block highly forward-scattered and directly transmitted light, producing darkfield images, and the iris allows control over the NA of the system. The microscope can similarly function in brightfield mode by toggling the mask out of the optical axis or in epifluorescence mode by using the Diaphot's

---

mercury arc lamp as the excitation source and an appropriate microscope filter set. When imaging the Fourier plane, an auxiliary 250 mm focal length doublet (Edmund Optics, NT45-353) on a kinematic mount (Thorlabs, FM90) is toggled into place, and the rear focal plane of the objective is imaged onto the CCD at a magnification of 0.5x. Similarly, during spectroscopic acquisition, a kinematic mounted mirror directs the signal along a second arm of the system. The scattering spectroscopy arm of the instrument consists of 175 mm (Edmund Optics, NT32-884) and 100 mm (Thorlabs, AC254-100-A1) focal length lenses and an infinity-corrected 20x, 0.5 NA microscope objective, which forms a telecentric image relay to the core of a 1.5 mm core-diameter 0.51 NA acrylic fiber (Edmund Optics, NT02-535). This fiber collects the entire optical signal, which is mode-scrambled using mandrel wrapping, sampled using a 200  $\mu\text{m}$  core-diameter 0.22 NA fiber, and finally spectrally resolved and measured by a TE-cooled 16-bit spectrometer (BWTek, BTC111, Newark, DE). The pupil relay and Fourier plane masks are each mounted on single-axis micrometer translation stages, which allow easy objective substitution within the microscope. Alignment of the system for each objective is accomplished by directing a collimated laser beam into the objective, locating the best focus in the Fourier plane using the Foucault knife edge test, and then imaging the knife edge onto the CCD by adjusting a pupil relay lens translator. The image plane requires no adjustment as the intermediate 35 mm image plane is fixed when the microscope is in focus.

---

## 8.4 Instrument calibrations and corrections

Angular calibrations, flat-field corrections, and background measurements are generated on an objective-by-objective basis. The angular response of the system in Fourier imaging mode is determined by using a 30 line-pairs  $\text{mm}^{-1}$  Ronchi ruling in the object plane under collimated monochromatic illumination. The resulting Fourier pattern is imaged onto the CCD in both vertical and horizontal orientations, and CCD pixels are calibrated for angle using Bragg's law,

$$\sin(\theta_{scatt}) = m\lambda / n_{water}d, \quad (8.1)$$

where  $\theta_{scatt}$  is the scattering angle,  $m$  is the diffraction order,  $\lambda$  is the wavelength,  $n_{water}$  is the refractive index of water (1.3387), and  $d$  is the slit width of the ruling. To correct for stray light, CCD dark counts, and background scattering, a measurement is taken using a sample of distilled water at the same exposure time and subtracted from the data. Flat-field correction terms are generated by measuring the response of the system to a Lambertian source comprised of a 7-mm-thick sample of a scattering emulsion. Under these conditions, photons in the medium are sufficiently randomized, and the emulsion-coverslip interface emits

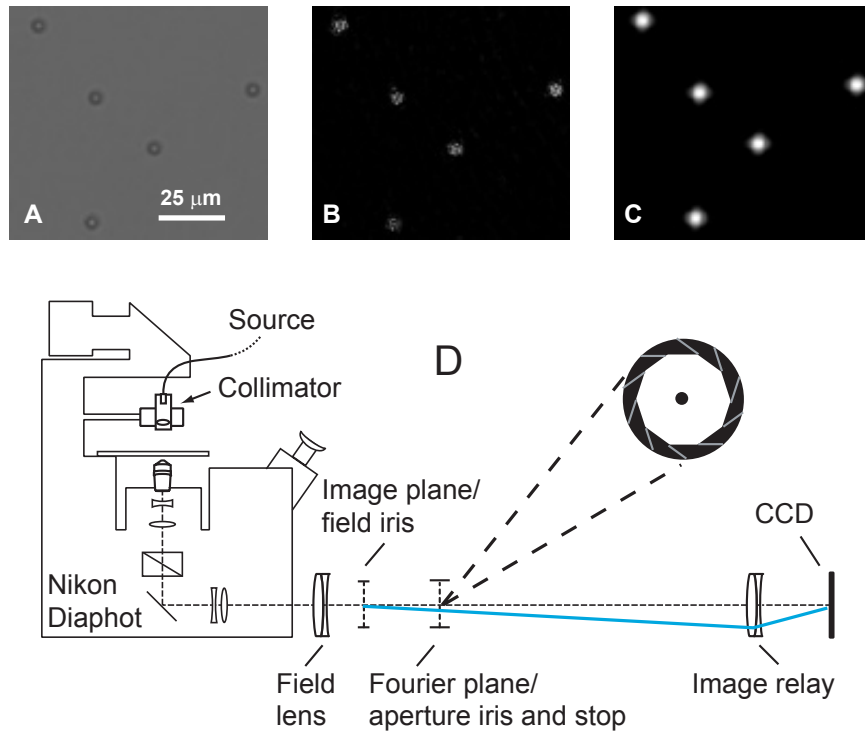


**Figure 8.3.** Representative data from 4 μm polystyrene microspheres from our system in imaging mode. Panel (A) is a brightfield image of these microspheres. When we toggle the Fourier mask (see panel D) into place, we block out the unscattered light and form a darkfield image (B). The system can also operate in epifluorescence mode (C). Panel (D) shows the system in imaging mode with a detailed schematic of the Fourier mask.

---

isotropically and uniformly over the entire field. Division of acquired data by this correction accounts for pixel-by-pixel response, variations in the excitation beam profile, and the optical response of the system.

## **8.5 Verification of instrumentation with a model system**

We demonstrate the functionality of the instrumentation in all modes of operation by measuring samples of fluorescent polystyrene microspheres (Molecular Probes, F-8859, Eugene, OR) suspended in distilled water. These spherical scattering centers have a narrow size distribution ( $4.0 \pm 0.014 \mu\text{m}$ ), a refractive index of 1.59 at 500 nm [6], and are both absorbing and fluorescent, providing a model system that can be exploited by every data acquisition mode of our instrument. To enhance the demonstration of our instrument's angle-resolved scattering mode, we also used a sample of  $2 \pm 0.08 \mu\text{m}$  polystyrene microspheres. For studies with microspheres, slides are created by pipetting  $10 \mu\text{l}$  of beads in suspension onto a  $45 \times 45 \text{ mm}$  square No. 1 thickness coverslip and covering the liquid with a second round  $25 \text{ mm}$  No. 1 coverslip. For monochromatic illumination, we use the  $457.9 \text{ nm}$  line from an  $\text{Ar}^+$  laser, and for collection, a  $10\times$ ,  $0.45 \text{ NA}$  water immersion objective.

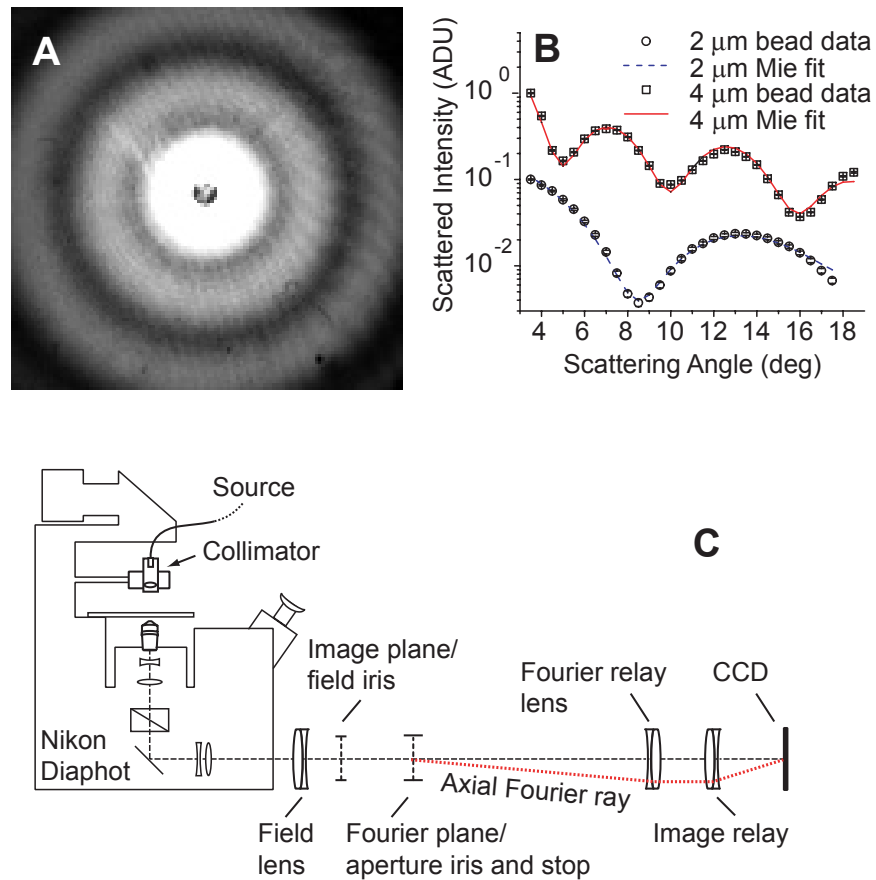


**Figure 8.4.** Representative data from 2 and 4  $\mu\text{m}$  beads taken with our system in Fourier imaging and angle-resolved scattering mode. Panel (A) shows an image of the Fourier plane from the same field of view as that of figure 8.3. When we annularly bin these data, we get an angular scattering distribution. Panel (B) shows such data for 2 and 4  $\mu\text{m}$  polystyrene microspheres. The symbols represent data, and the lines represent Mie theory fits as described in the text. Panel (C) shows the system in Fourier plane and angle-resolved mode.

---

Representative fields of the 4  $\mu\text{m}$  fluorescent microspheres acquired from the instrument in imaging mode are shown in figure 8.3. In brightfield imaging mode (A) we can clearly see the microspheres against a background of transmitted illumination light. When we toggle the Fourier mask into place, we get the corresponding darkfield image (B) which is an image of only that light scattered from the beads and collected by the objective. Shown in panel (C) is an image of this same field of view in epifluorescence mode. There is excellent spatial agreement in all three images.

When we toggle our pupil relay lens into place, we get data such as that displayed in figure 8.4. In Fourier-plane imaging mode (A), we see the far-field diffraction pattern from the spheres. Annular binning of the Fourier image provides an angle-resolved measurement (B) that can be fit with the Mie theory model described in Section 3.4. Here our fit predicts the size distribution to be  $4.05 \pm 0.001 \mu\text{m}$ . Shown on the same axis (offset for clarity) are data from the 2  $\mu\text{m}$  polystyrene spheres mentioned above with a Mie theory fit that predicts a diameter of  $2.01 \pm 0.10 \mu\text{m}$ .

When we switch our light source to the lamp, and toggle our folding mirror into place, we obtain light scattering spectroscopic data such as that shown for the 4  $\mu\text{m}$  beads in figure 8.5. These data are fit using an absorbing-sphere Mie

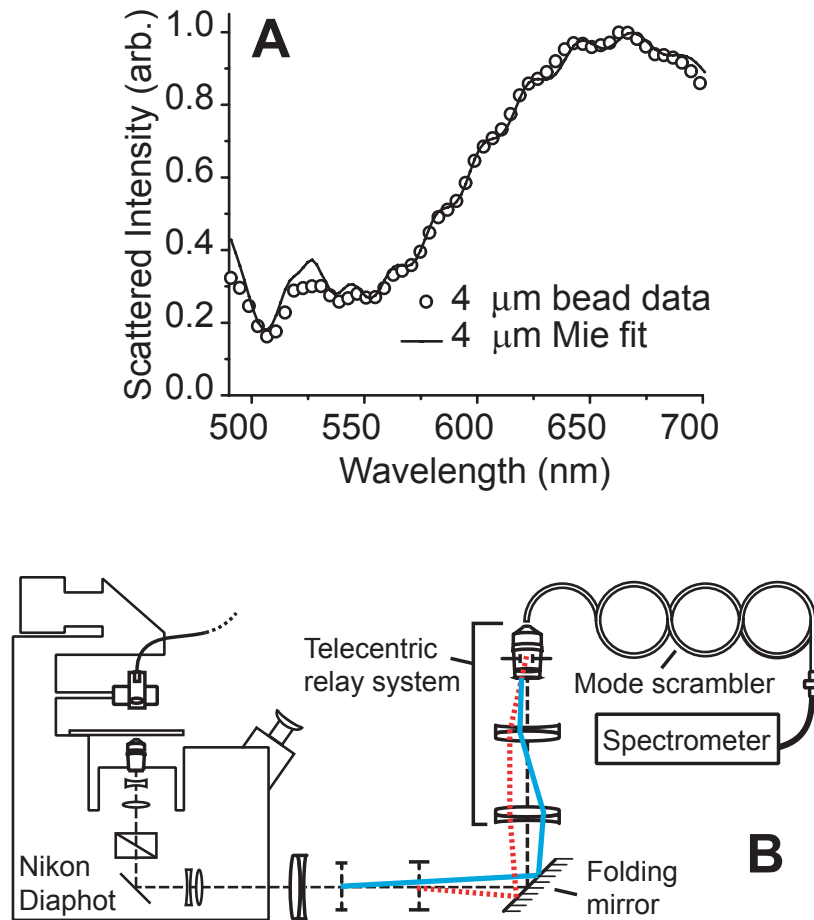


**Figure 8.5.** Representative data from 4  $\mu\text{m}$  beads taken with our system in scattering spectroscopy mode. Panel (A) shows scattering data in open circles and the absorbing-sphere Mie theory fit as a solid line. Panel (B) shows the schematic of our system in spectroscopy mode.

---

theory model in which the wavelength-dependent absorption is accounted for explicitly using a basis spectrum that was measured by fluorescence excitation. The free parameters are the mean,  $\mu$ , and standard deviation,  $SD$ , of the particle size, the absorber concentration  $c_a$ , and the real part of the particle refractive index,  $n_r$ . If we call the measured fluorescence excitation spectrum  $ex(\lambda)$ , then we let the wavelength-dependant index of refraction vary as

$$n(\lambda) = n_r + i c_a \frac{\lambda}{4\pi} ex(\lambda). \quad (8.2)$$

The fit, displayed as a solid line, predicts  $3.93 \pm 0.02 \mu\text{m}$  diameter particles. Although this measurement and model is less sensitive to particle size parameters than is the angle-resolved measurement, this fit is extremely sensitive to refractive index, predicting 1.599, while changing the refractive index by 0.01 degraded  $\chi^2$  by 50%.

## 8.6 Data from intact EMT6 cells

The ability of our instrument to measure fluorescence and angle-resolved scattering from the same field of an adherent cell monolayer is shown in figure 8.6. EMT6 mouse mammary tumor cells were grown on coverslips and incubated with the photodynamic therapy sensitizer Pc 4 at a concentration of 250 nM overnight in the dark. Upon irradiation in cells, Pc 4 undergoes enhanced

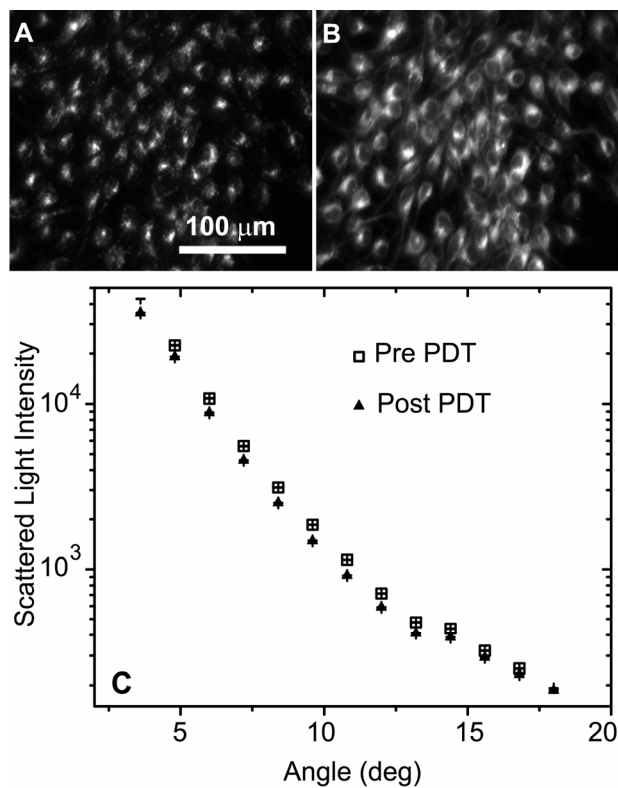


**Figure 8.6.** Fluorescence images of EMT6 cell monolayers following overnight incubation with 250 nM Pc 4 pre- (A) and post-PDT (B) with 600 mJ cm<sup>-2</sup> irradiation at 667 nm. Angularly resolved light scattering data (C) from the binned Fourier plane images for these same cell populations.

---

fluorescence emission and at low photodynamic doses induces scattering changes consistent with mitochondrial swelling [7]. The cells were imaged on the microscope in fluorescence mode and in Fourier imaging mode using light from a 658 nm diode laser. They were then irradiated on the stage of the microscope with  $600 \text{ mJ cm}^{-2}$  at 667 nm, and the measurements were repeated. As expected, the fluorescence intensity of Pc 4 is significantly lower pre-(A) vs. post-irradiation (B). The reduction in scattering in the treated cells in the angular range 3- 15 degrees is consistent with mitochondrial swelling, as shown in Chapters 4 and 7.

## 8.7 Discussion

The microscope in its present form represents a significant step forward in the field of organelle-specific light scattering. The design of this system extends the work of Boustany et al. [3] and that of Valentine et al. [4], by integrating all of the capabilities of both systems as well as adding a scattering spectroscopy mode. With the functionality of multimodal scattering data acquisition and multimodal imaging from the same field of view, the instrument enables several interesting lines of investigation. Motivated by the exquisite sensitivity of the spectroscopy arm to the index of refraction of absorbing particles, one can imagine a range of experiments in which different organelle populations are stained with high-extinction absorbing/fluorescent dyes, and their refractive indices are measured within the absorbing-particle model described in Chapter 5. Also, as

demonstrated by Boustany et al. [8], fluorescence-based molecular imaging techniques combined with light scattering measurements can help researchers to make connections between biochemical cellular signaling pathways and morphological changes measured with light scattering.

---

## References

1. Y. Liu, X. Li, Y. L. Kim, and V. Backman, "Elastic backscattering spectroscopic microscopy," *Opt. Lett.* **30**, 2445-2447 (2005).
2. H. Fang, L. Qiu, E. Vitkin, M. M. Zaman, C. Andersson, S. Salahuddin, L. M. Kimerer, P. B. Cipolloni, M. D. Modell, B. S. Turner, S. E. Keates, I. Bigio, I. Itzkan, S. D. Freedman, R. Bansil, E. B. Hanlon, and L. T. Perelman, "Confocal light absorption and scattering spectroscopic microscopy," *Appl. Opt.* **46**, 1760-1769 (2007).
3. N. N. Boustany, S. C. Kuo, and N. V. Thakor, "Optical scatter imaging: subcellular morphometry in situ with Fourier filtering," *Opt.Lett.* **26**, 1063-1065 (2001).
4. Valentine M.T., A. K. Popp, D. A. Weitz, and P. D. Kaplan, "Microscope-based static light-scattering instrument," *Opt. Lett.* **26**, 890-892 (2001).
5. J. W. Goodman, *Introduction to Fourier optics*, (McGraw-Hill, New York, 1996).
6. X. Ma, J. Q. Lu, R. S. Brock, K. M. Jacobs, P. Yang, and X. H. Hu, "Determination of complex refractive index of polystyrene microspheres from 370 to 1610 nm," *Phys. Med. Biol.* **48**, 4165-4172 (2003).
7. Wang K.K-H., J. D. Wilson, Kenney M.E., S. Mitra, and T. H. Foster, "Irradiation-induced enhancement of Pc 4 fluorescence and changes in light scattering are potential dosimeters for Pc 4-PDT," *Photochem. Photobiol.* DOI: 10.1111/j.1751-1097.2007.00128.x (2007)
8. N. N. Boustany, Y. C. Tsai, B. Pfister, W. M. Joiner, G. A. Oyler, and N. V. Thakor, "BCL-xL-dependent light scattering by apoptotic cells," *Biophys. J.* **87**, 4163-4171 (2004).

## **Appendix. Experimental details of the goniometer**

### ***A.1 Introduction***

This appendix is devoted to practical use of the goniometer experiment housed in the Foster Laboratory at the University of Rochester. Many of the details of the setup procedures would be of use to a general audience, but the intention of this appendix is for the benefit of future graduate students to be able to repeat and extend upon the work presented in the preceding chapters of this thesis. Detailed below are sections explaining the critical experimental components, procedures and protocols to align the goniometer, hardware and software settings for proper data acquisition, and the artifacts and limitations of the experimental setup in its present form.

### ***A.2 Critical experimental components***

A digital photograph of the goniometer setup is shown in figure A.1. The quality of the measurement in this experiment is substantially tied to the quality and placement of the sample cuvette. The cuvette acts to lens the incident light,

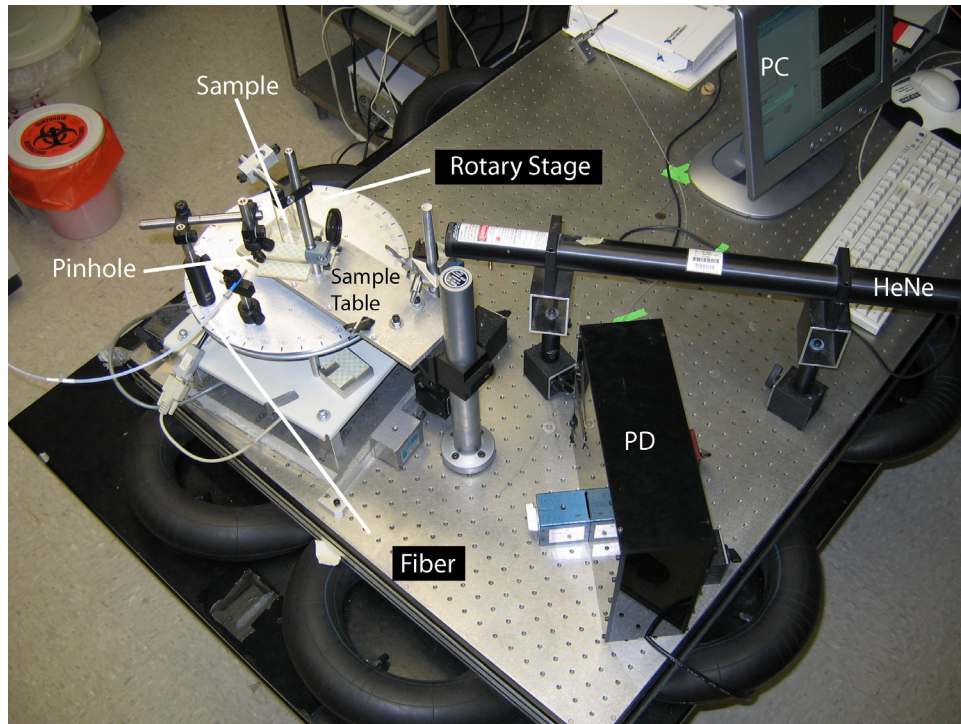


Figure A.1. Digital photograph of the Foster Laboratory goniometer experiment.

---

and imperfections in the cuvette such as scratches or dirt create stray light that is hard to remove via background subtraction. The greater the diameter of glass used, the less it lenses the incident light. The cuvette that we have chosen is a 2 cm path length quartz light scattering cell (Hellma #540.115, Plainview, NY).

The rotary table (RT-12, Arrick Robotics, Tyler, TX) has significant backlash/vibrations, and we have not found a way to reliably and repeatably set the cuvette directly in the center of the stage such that it will not move during the course of the measurement. To get around this, we mount the cuvette atop a fixed table that sits approximately 1 inch above the rotary stage. This eliminates any error due to the vibrations of the motor during operation, and holds the cuvette in a fixed position relative to the incident laser beam such that any lensing and diffraction due to the curvature and smoothness of the cuvette surface is at least constant throughout the angle-resolved measurement.

The detector has to strike a balance between sensitivity, dynamic range, and vulnerability to damage due to high light intensities. The detector that we chose is a photoreceiver built around a conventional PIN diode (New Focus, 2001, San Jose, CA). The receiver has an adjustable gain and frequency response, and operates on 9 V batteries, eliminating the usual 60 Hz noise found in detectors plugged into the wall socket. With the gain turned all the way down, the detector saturates at 10 mW, and with the gain turned all the way up, it saturates at 333 nW.

### ***A.3 System alignment protocol***

The alignment of the goniometer experiment proceeds in three basic phases: aligning the laser relative to the rotary stage, setting and centering the cuvette, and aligning the detection components. A basic 7-step schematic of this process is shown in figure A.2.

To align the HeNe laser, you must first remove all of the hardware from the rotary table and place two small-diameter irises at equal heights on opposing screw-holes on the rotary table. You then adjust the laser such that the beam goes straight through both apertures. As a check that the apertures are set correctly, turn the rotary table around such that the laser passes through both irises in the opposite orientation (see panels 1 and 2). Once the laser is aligned, you must align a second laser that is pointing as close to perpendicular to the HeNe as possible using the same procedure outlined above (see panel 3). This second laser will be used later to align the cuvette.

Next mount the sample table 1-2 inches above the rotary table in such a way that a sufficient portion of the table sits over the center of the rotary stage (see panel 4). Place the cuvette mount, which is a piece of clear plastic with a corner made from two pieces of double-stick tape (see panel 5), onto the sample table, and place the water-filled cuvette into the corner created by the double-stick tape. Remove one of the irises, and align the cuvette mount such that each laser passes through the remaining iris with or without the cuvette in the path. Once

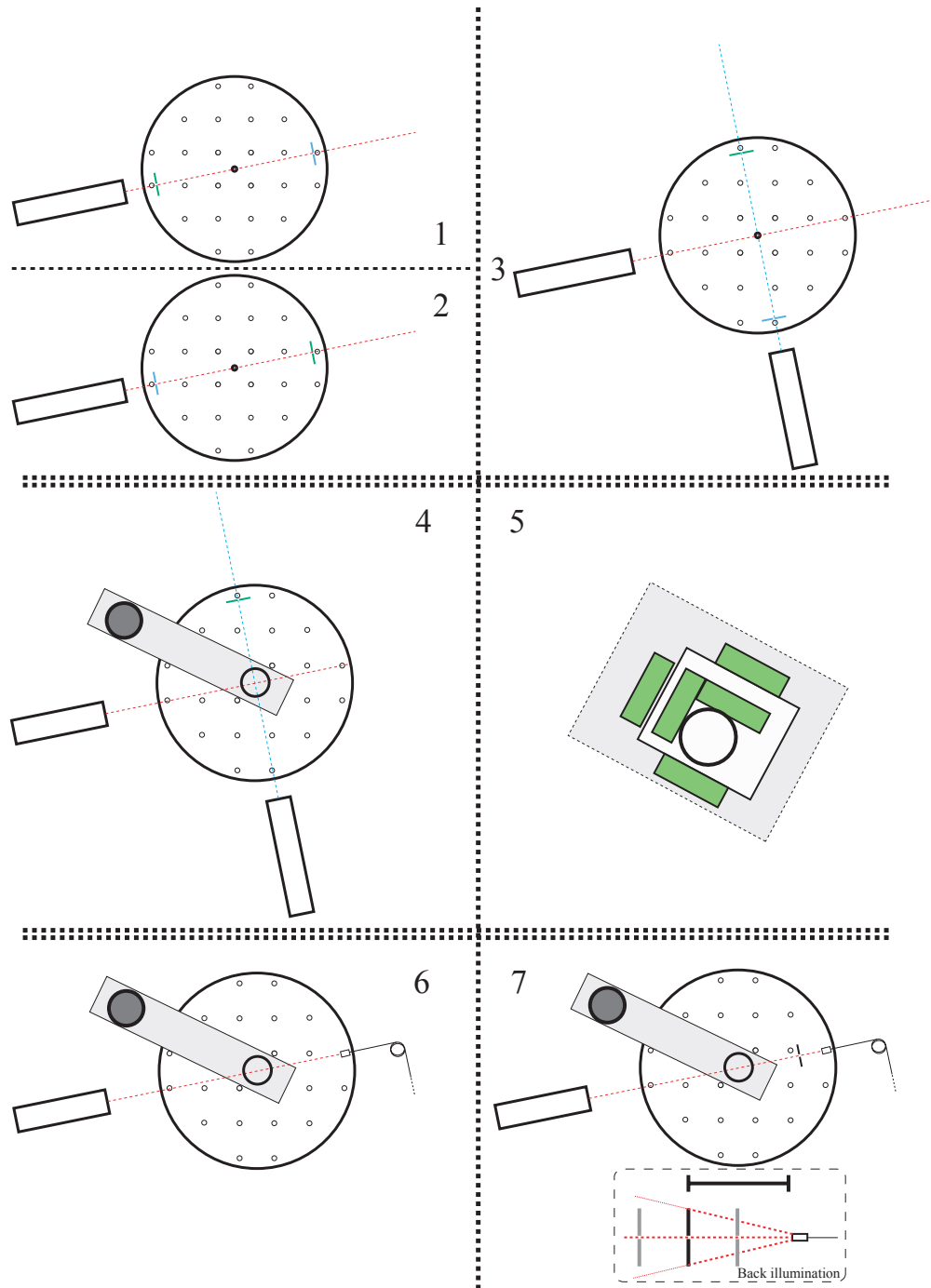


Figure A.2. Seven-step schematic for alignment of the goniometer experiment.

The three phases of alignment are separated by the horizontal double-lines.

the cuvette is perfectly centered, secure the holder into place with more double-stick tape (see panel 5).

We next set the detection fiber using a free-space fiber mount. Align the fiber such that the back-reflection off of the fiber tip goes directly back into the cavity of the laser. For a sanity check, do this for both the HeNe and the second alignment laser beam (see panel 6). Next set the aperture in front of the fiber such that the incident laser light goes straight through the aperture, and the back-reflection from the fiber tip also goes straight through the aperture. Set the distance between the fiber tip and aperture such that when the fiber is back-illuminated, the NA of the fiber exactly fills the aperture. This will maximize angular resolution while not allowing the fiber to ‘look around’ the aperture. Once the aperture is in place, close the iris as far as it will go.

#### ***A.4 Hardware and software settings***

Aside from the hardware and proper alignment, there are three settings that needed to be adjusted to make a good measurement. The first is the gain on the photoreceiver. For measurements with cells, the gain should be turned all the way up, and the frequency response should be set to DC. The output of the detector is split, and is read out by analogue channels 0 and 2 on the daqboard. These channels should be read out at +/- 156 mV and 0 - 2.5 V, respectively. The final software issue is to select “HeNe” on the toggle button on the front page of the data acquisition VI.

---

### **A.5 Data acquisition**

The angular position of the rotary stage is read out by an optical encoder. The instrumentation in its present form is only capable of measuring relative changes in the angular position of the stage. When you start acquiring data, the LabView VI assumes that you are at the position  $\theta = 0$ . The hardware of the rotary stage is such that there is a magnetic ‘home’ position, and there is a LabView VI called ‘motor\_home.VI’ that drives the motor in the counterclockwise direction until the home position is detected. This VI is called as a subroutine at the end of every VI that involves motor control. The motor\_home VI should be run prior to the start of any experiments on a given day. It is a good idea to purposefully rotate the motor *clockwise* past the home position by hand before sending the table to the home position under computer control, as the motor will only run counterclockwise and will run into your sample table if it is on the wrong side of home.

In order to re-calibrate the angles read out by the LabView VI, you need to first measure the angular position of your laser beam relative to the home position. You first need to send the rotary table home. After turning the gain of the photoreceiver all the way down, run the LabView VI ‘MyAngleandDataAquisition.VI.’ This VI only records the diode voltage and the relative angular position. Scan the rotary table by hand through the laser beam such that you can re-calibrate your angles with that position being zero.

When you are ready to acquire data, set the cuvette with 15 ml of HBSS and take a background measurement. Add a concentrated stock solution of your sample such that the final concentration yields a mean free path of 5-10 cm. This can be measured directly in the spectrophotometer. You need to take several angle-resolved measurements of both the data and background, as the motor driver as implemented in LabView can be off by as much as  $1^\circ$  from measurement to measurement.

### ***A.6 Limitations on measurements***

There are several experimental artifacts that must be understood in order to make meaningful measurements on the goniometer. The first is the fact that the curved cuvette serves to lens the incident light, meaning that the first  $2^\circ$  are inaccessible by this measurement. Furthermore, as measurements are made closer to  $\theta = 0^\circ$ , the  $\text{Sin}(\theta)$  correction to account for the overlap between the incident light and the detector field of view breaks down (see figure A.3). This artifact makes it difficult to reliably obtain good angle-resolved scattering data for angles  $5^\circ$  or smaller.

The second artifact that cannot be ignored in these measurements is the effects of back-reflections from the cuvette. This is illustrated in figure A.4. When light is passed through the cuvette, some light (approximately 5 %) reflects off of the final surface of the chamber and travels a second path through the cuvette in the opposite direction. As Mie-type scattering is highly forward-

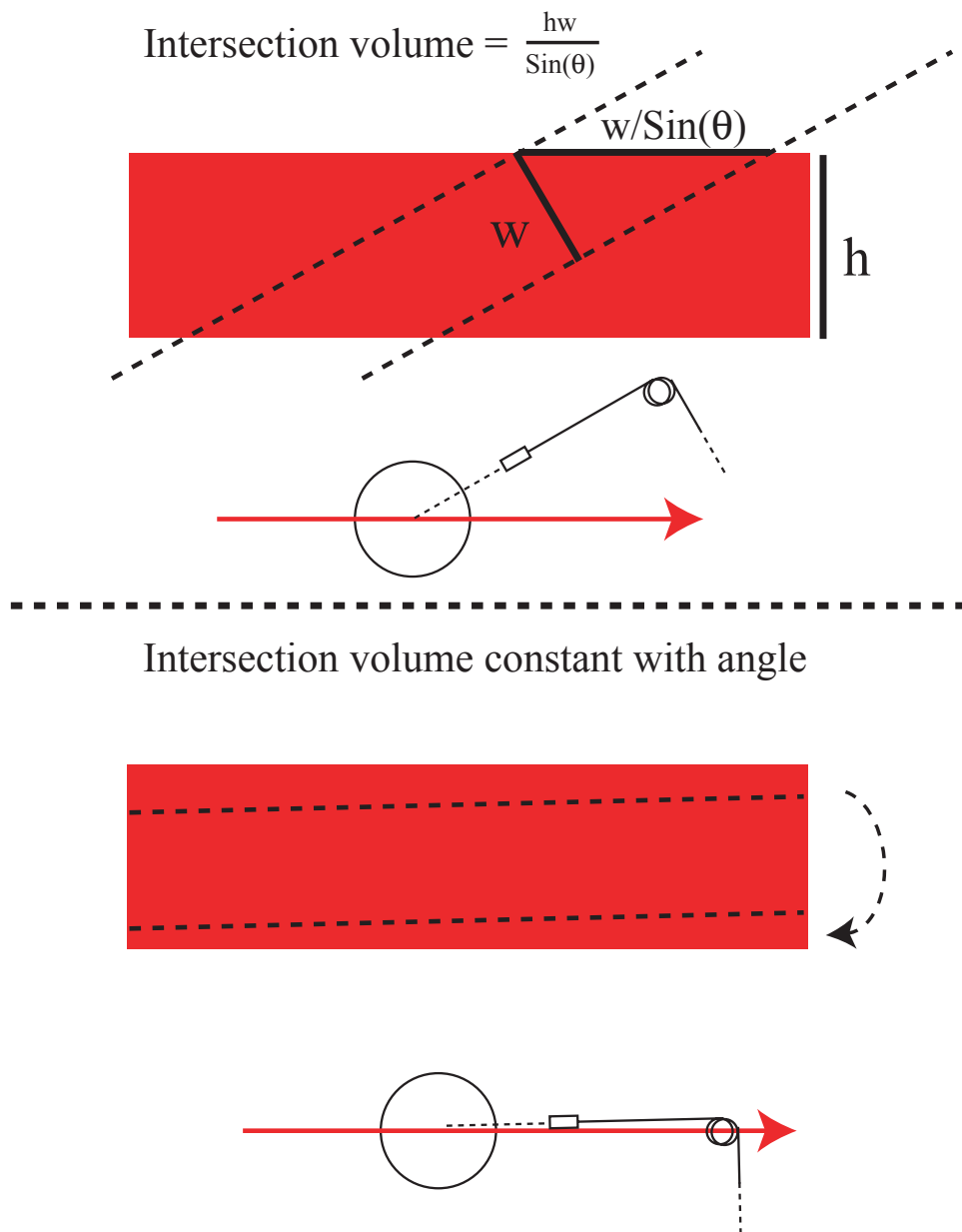


Figure A.3. Schematic explanation of the  $\sin(\theta)$  correction to the angle-resolved data and why this correction fails at extremely shallow angles. In the top drawing,  $h$  is the width of the laser beam and  $w$  is the width of the detector field of view.

directed, the backscattering signal is heavily contaminated by light that was forward-scattered from the small portion of the incident laser that was back-reflected and is traveling this backward path, as illustrated in figure A.4.

The final effect that must be expanded upon is the dependence of the quality of the scattering data versus the status of the iris diaphragm in front of the collection fiber. The trade-off is angular resolution versus signal. If the system is properly aligned, there is sufficient signal when the iris is all the way closed. If there is a need to increase signal, the iris can be opened a bit without significant loss of angular resolution at medium and high angles. As the iris affects the width of the detector field of view, the artifact that will most affect the scattering data is the failure of the  $\text{Sin}(\theta)$  correction at shallow angles. Once the system is aligned and the iris is set such that adequate signal is being collected, the quality of the acquired data must be assessed regularly via calibration with polystyrene microspheres. We have found that examining scattering data acquired with these standards is the best gauge of how well the system is aligned, and over what angular range the acquired data should be trusted.

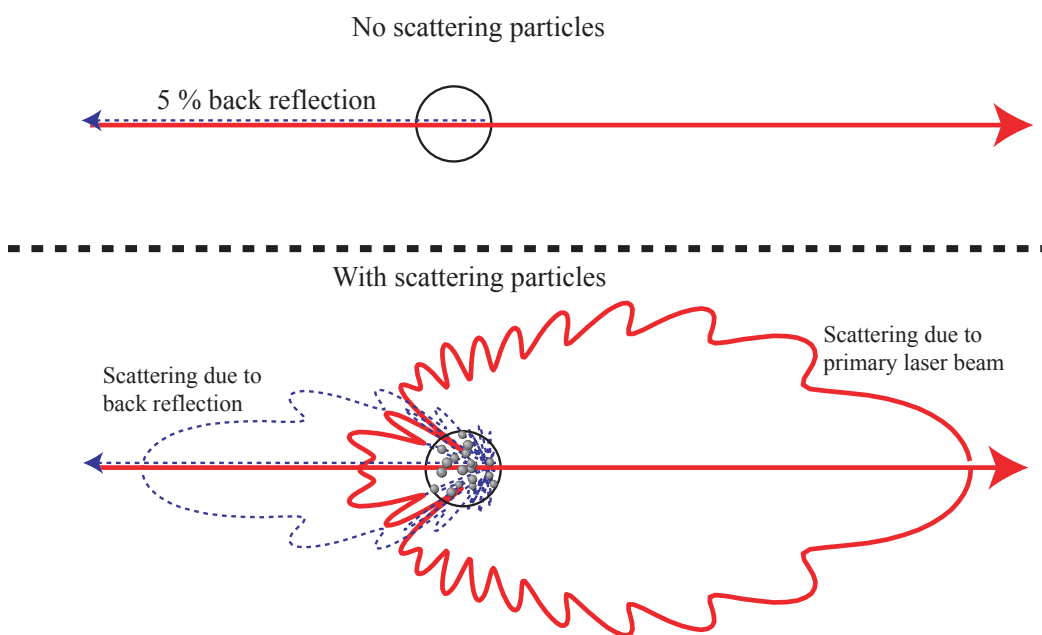


Figure A.4. Schematic to demonstrate how back reflections can affect backscattering signal from angularly-resolved measurement. There is a roughly 5 % back reflection from the final surface of the cuvette, causing light to traverse a second path through the cuvette in the opposite direction. In the lower panel, we plot polar logplots showing the scattered intensity from the forward directed laser light (solid red) and the back-reflected light (blue dashed line) from  $2\ \mu\text{m}$  polystyrene microspheres in water at 633 nm. In the backscattering direction, the blue curve dominates the red curve by several orders of magnitude.